EPFL

Influence of thermo-mechanical processing on ordering kinetics in 18 karat red gold alloy

Présentée le 9 mars 2020

à la Faculté des sciences et techniques de l'ingénieur
Neutrons et rayons X en mécanique des matériaux
Programme doctoral en science et génie des matériaux

pour l'obtention du grade de Docteur ès Sciences

par

Marina GARCIA GONZALEZ

Acceptée sur proposition du jury

Prof. C. Hébert, présidente du jury
Prof. H. Van Swygenhoven, Dr S. Van Petegem, directeurs de thèse
Prof. M. Heilmaier, rapporteur
Prof. L. Thilly, rapporteur
Prof. W. Curtin, rapporteur

■ École
polytechnique
fédérale
de Lausanne

2020

AKNOWLEDGEMENTS

ABSTRACT

Precious alloys are often subject to a series of mechanical and thermal operations during manufacturing. For 18 karat red gold alloys these operations lead to the build-up of residual stresses, which are the prime cause for fracture and shape distortion. Red gold undergoes a disorder→order solid state phase transformation. Chemical ordering results in the formation of coherent and chemically ordered nano-sized domains that induce misfit strains, causing strong distortions in both the disordered matrix and the ordered domains. This, in turn, affects the mechanical properties of the alloy. This study aims to establish the link between the microstructural evolution and chemical ordering as a function of thermo-mechanical history. To this end, *in situ* synchrotron X-ray diffraction experiments have been combined with electron microscopy studies. The main alloy under study corresponds to the red gold alloy with composition 75Au-20.5Cu-4.5Ag in %wt. Additionally, a few experiments have been carried out on a chemically modified red gold, with small additions of Sn and Pd, in order to compare the ordering kinetics under comparable thermo-mechanical history.

A combination of high energy X-ray diffraction and transmission electron microscopy studies have established a correlation between the microstructure during ordering and microstructure footprints in X-ray diffraction.

Industrially processed samples have been characterized at each operation step by standard characterization techniques, electron microscopy and *ex-situ* high energy X-ray diffraction, revealing that plastic deformation promotes natural ageing. *In situ* high-energy X-ray diffraction experiments during isothermal heating of samples with and without prior plastic deformation evidence that the presence of a dislocation network in the microstructure decreases the onset temperature for ordering and enhances precipitation growth at the early stages of the transformation. *In situ* high-energy X-ray diffraction experiments during isochronal heating show that during initial heating, the elastic lattice strain in the ordered phase increases. The ordering rate and accumulation of lattice strain depends on the cooling rate, predeformation and chemical composition. Above a given temperature, which depends on the deformation state and chemical composition, the lattice strain of the ordered phase relaxes. The lattice relaxation is ascribed to the formation of a tweed structure.

Keywords *In situ*, X-ray diffraction; transmission electron microscopy; 18 karat Gold alloys; Order-Disorder; Red Gold; Thermo-mechanical processing; Plastic Deformation; cooling rates; Isothermal Ageing; Anisothermal ageing; Heating

RESUMÉ

Les alliages précieux sont souvent soumis à une série d'opérations mécaniques et thermiques lors de la fabrication. Pour les alliages d'or rouge 18 carats, ces opérations conduisent à l'accumulation de contraintes résiduelles, qui sont la principale cause de fracture et de distorsion de forme. L'or rouge subit une transformation de phase d'ordonnancement à l'état solide. L'ordre chimique entraîne la formation de domaines nanométriques cohérents qui engendrent des contraintes pour maintenir la cohérence du réseau, provoquant de fortes distorsions à la fois dans la matrice désordonnée et dans les domaines ordonnés. Ceci, à son tour, affecte les propriétés mécaniques de l'alliage. Cette étude vise à établir le lien entre l'évolution microstructurale et l'ordre chimique en fonction de l'histoire thermomécanique. À cette fin, des expériences *in situ* de diffraction des rayons-X synchrotron ont été combinées avec des études de microscopie électronique. L'alliage principal à l'étude correspond à l'alliage d'or rouge de composition 75Au-20.5Cu-4.5Ag en% poids. Des expériences supplémentaires ont été réalisées sur un or rouge chimiquement modifié, avec des ajouts de Sn et Pd, qui montre des meilleures propriétés de corrosion tout en maintien de la couleur rouge. Une combinaison d'études de diffraction des rayons X à haute énergie et de microscopie électronique à transmission a établi une corrélation entre la microstructure lors de l'ordonnancement et les empreintes de microstructure dans la diffraction des rayons-X. Les échantillons traités industriellement ont été caractérisés à par des techniques de caractérisation standard, de la microscopie électronique et la diffraction des rayons-X à haute énergie ex situ, révélant que la déformation plastique favorise le vieillissement naturel.Des expériences de diffraction des rayons-X à haute énergie *in situ* lors du chauffage isotherme d'échantillons avec et sans déformation plastique préalable prouvent que la présence d'un réseau de dislocations dans la microstructure diminue la température de début d'ordonnancement et améliore la croissance des domaines ordonnés aux premiers stades de la transformation.Des expériences de diffraction des rayons-X à haute énergie *in situ* pendant le chauffage isochrone montrent que pendant le chauffage initial, la déformation du réseau élastique dans la phase ordonnée augmente. Le taux de commande et l'accumulation de déformation du réseau dépendent de la vitesse de refroidissement, de la préformation et de la composition chimique. Au-dessus d'une température donnée, qui dépend de l'état de déformation et de la composition chimique, la déformation du réseau de la phase ordonnée se relâche. La relaxation du réseau est attribuée à la formation d'une structure en tweed.

List of abbreviations

FCC	Face centered cubic
FCT	Face centered tetragonal
BCT	Body centered tetragonal
EBSD	Electron backscatter diffraction
FEG	Field emission gun
FIB	Focused ion beam
FWHM	Full-width at half-maximum
IPD	Inverse pole figure
OM	Optical microscopy
SEM	Scanning electron microscopy
TEM	Transmission electron microscopy
DF	Dark field
BF	Bright field
STEM	Scanning transmission electron microscopy
EDS	Energy dispersive X-ray Spectroscopy
FFT	Fast Fourier Transform
IFFT	Inverse Fast Fourier Transform
PAP	Periodic Antiphase
APB	Antiphase boundary
T_{OD}	Temperature order→disorder
R	Red gold alloy
MR	Modified red gold alloy
COD	Crystallographic open database
CIF	Crystal information file
PF	Pole figure
CCD	Charge-coupled device
HRTEM	High resolution transmission electron microscopy
CIME	Centre Interdisciplinaire de Microscopie Electronique
EPFL	Ecole Polytechnique Federale de Lausanne
GIS	Gas injector system
ESRF	European Syncrhotron Radiation Facility
XRD	X-ray diffraction

Table of Figures

List of Tables

List of Equations

Contents

Chapter 1   Introduction

1.1. Motivation

Au-Cu-Ag based alloys constitute the backbone of the precious metal industry for jewellery and watch making. These alloys combine the aesthetics and excellent corrosion properties of Au with good mechanical properties. The Au content of a precious alloy is measured in karats, which designates the weight ratio of gold out of 24 parts. Typical gold contents in precious alloys are 14k (58% Au in %wt.), 16k (66% Au in %wt.) and 18k (75% Au in %wt.).

In the last years, the development of new gold-based alloys with different optical properties has received particular attention. Novel colours are obtained by modifying the chemical ratio of the additional elements[1]. In particular, the 18-karat red gold alloy is a high copper content alloy with a chemical composition of 75.0Au-20.5Cu-4.5Ag in %wt.

The pursuit of colour via chemical modifications alters fundamental alloy properties such as structural phase transitions and the corrosion properties. Chemical ordering in the Au-Cu system and the miscibility gap in the Cu-Ag system characterize the ternary system of Au-Cu-Ag. The high copper-content of the red gold alloy results in a red metallic colour and a chemical disorder → chemical order phase transition, characteristic of the equiatomic AuCu composition.

Manufacturing of red gold exhibits unpredictable mechanical failure such as cracking, fracture and shape distortion during the fabrication process. Processing operations can induce chemically ordered $L1_0$ nanodomains that are known to lead to the build-up of residual stresses, which are the prime cause of distortion. Processing parameters such as thermal treatment temperature, cooling rates and mechanical deformation can deeply influence the ordering kinetics.

Historically, special attention has been devoted to the equiatomic AuCu alloy as a prototype alloy for solid-state order-disorder phase transitions. Above 410°C, AuCu manifests a substitutional solid solution arranged in a A1-type structure (face centered cubic). Below T=380°C, it transforms into the chemically ordered $L1_0$-type (face centered tetragonal) structure. Chemical order is characterized by stacking layers of only gold and only copper atoms along the c-axis of the lattice[2]. At the early stages of ordering, non-local and long-range coherency strains build up between the ordered domains and the disordered matrix, which notably increase the flow stress of the alloy and result in an age-hardening behaviour (known as *order hardening*[3,4]).

To date, most of the research on Au-Cu-Ag ternary alloys targeted applications in complex corrosive environments such as the oral cavity, where the age hardenability of the alloy is employed to tailor the specific hardness properties required for dental implants [5–10].

For jewellery however, there is a need to study the formation of the ordered phase during thermo-mechanical processing. The development of chemical order during the fabrication process hardens the microstructure and drastically reduces the workability of the alloy. For this reason, precious alloys are generally treated in the metastable A1 phase that is readily workable. This phase can be reached by water quenching to room temperature. However, red gold exhibits room temperature ordering after water quenching, which makes further metalworking problematic. The formation of the ordered phase is difficult to follow experimentally, due to which there is still a lack of understanding of the influence of thermo-mechanical operations in the ordering kinetics.

In the search of alternative manufacturing procedures, continuous furnaces result in a more *stable* microstructure at room temperature. These furnaces provide with milder cooling rates that significantly reduce the density of quenched-in excess vacancies, so that natural ageing after cooling is suppressed. However, when the alloy is subsequently deformed, for instance to form U-shape semi-finished products, enormous shape distortions are still observed after heat treatments.

This dissertation explores the microstructural evolution of coherent and chemically ordered nanodomains in red gold alloys ($Au_{51.1}Cu_{45.5}Ag_{5.6}$) subject to different thermo-mechanical histories. Namely, the thermal treatment temperature, the cooling rate, mechanical deformation and minor alloy modifications.

- The thermal treatment temperature (and duration) will influence the grain size of the alloy as well as the density of thermal vacancies before cooling.
- The cooling rate will allow for partial ordering (slow cooling rates) or freeze-in excess vacancies at room temperature (fast cooling rates).
- Plastic deformation will induce a dislocation network in the microstructure. The elastic strain fields of the dislocations can interact with the $L1_0$ phase formation.
- Minor alloy modifications with Sn (0.1-2%wt.) and Pd (0.1-1.1%wt.) enhance the corrosion properties of red gold while maintaining the red colour.

1.2. Objectives and thesis structure

The aim of this study is to understand the influence of thermo-mechanical history on the $L1_0$ ordering transformation and establish a link between the microstructural evolution and the ordering stages. To that end, *in situ* X-ray synchrotron studies have been performed during isothermal and anisothermal thermal treatments. Complementary electron microscopy investigations have also been performed.

The structure of the thesis is as follows:

Chapter 2 focuses on the experimental aspects of the studies. Section 2.1. describes the materials. Section 2.2. describes the processing of the samples of interest. Section 2.3. describes the metallographic and hardness characterization techniques. Section 2.4 defines the employed electron microscopy techniques. Section 2.4. gives an overview of X-ray diffraction technique and a description of the *in situ* experimental set-ups.

Chapter 3 presents the microstructural characterization of thermo-mechanically processed U-shaped samples in industry. Section 3.1. presents typical hardness values of red gold. Section 3.2. presents the hardness evolution during the manufacturing route of U-shaped samples. Section 3.3. presents shape distortion experiments on the U-shaped samples. Section 3.4. presents a comprehensive microstructural characterization of the U-shaped samples at each processing step.

Chapter 4 presents isothermal ageing experiments by means of high-energy synchrotron X-ray diffraction and transmission electron microscopy. Section 4.1 presents the preliminary microstructures. Section 4.2 presents *ex situ* studies on the microstructural evolution under isothermal ageing conditions. Section 4.3 presents *ex situ* natural ageing studies on samples processed in industry. Section 4.4. presents *in situ* investigations during isothermal ageing experiments as a function of previous cooling rate and predeformation.

Chapter 5 presents *in situ* heating experiments by means of high-energy synchrotron X-ray diffraction. Section 5.1 presents the microstructure after cooling. Section 5.2 shows *in situ* studies the microstructural evolution during heating of red gold as a function of previous cooling rate and predeformation. Section 5.3. studies the microstructural evolution during heating of the modified red gold as a function of previous cooling rate and predeformation.

Chapter 6 presents the discussion and summarizes the results.

1.3. Chemically ordered phases

Binary substitutional AB alloys with negative enthalpy of mixing, i.e. the mixing of A and B atoms is exothermic, show a tendency to chemically order at low temperatures. These alloys are solid solutions at high temperatures, but at low temperatures, and depending on the atomic interaction energies, the different atoms segregate to preferential lattice sites. Under these circumstances, the alloy is said to show perfect long-range order, which exhibits an identical structure to that of an intermetallic. The preferential arrangement of species at fixed lattice sites results in the so-called super-lattice or super-structure[11,12]. The long-range order parameter, S, quantifies the degree of chemical order[13]. Considering an AB solution with x_A and x_B the atomic fractions corresponding to the A and B species, the concentration of α- and β-sites as γ_α and γ_β, respectively; and the fraction of α- and β-sites occupied by the correct species (A or B, respectively) as r_α and r_β, the S parameter can be defined as [14]:

$$S = r_\alpha + r_\beta - 1 = \frac{r_\alpha - x_A}{\gamma_\beta} = \frac{r_\beta - x_B}{\gamma_\alpha}$$

Equation 1-1 Definition of the long-range order parameter S

The S parameter is equal to unity with perfect chemical order and decreases with increasing temperature until it becomes zero at the order → disorder temperature (T_{OD}). Long-range order can still be achieved when the composition deviates from stoichiometry. However, off-stoichiometry can easily disrupt long-range order with increasing temperature and results in a lower T_{OD}. For instance, Figure 1-1 shows part of the Au-Cu phase diagram where the CuAu and Cu_3Au superlattices are stable off the stoichiometric composition. Common ordered phases are illustrated in Figure 1-2 along with their *Structurbericht* notation as well as typical alloy systems displaying these ordered structures.
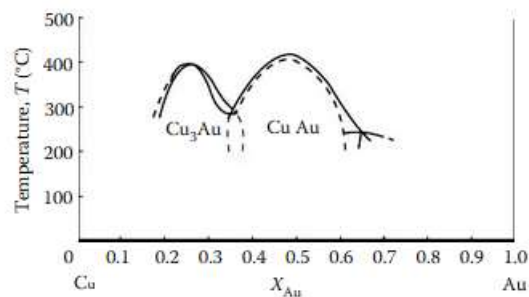
Figure 1-1 Part of the Au-Cu phase diagram showing the regions where the Cu3Au and CuAu superlattices are stable [15]
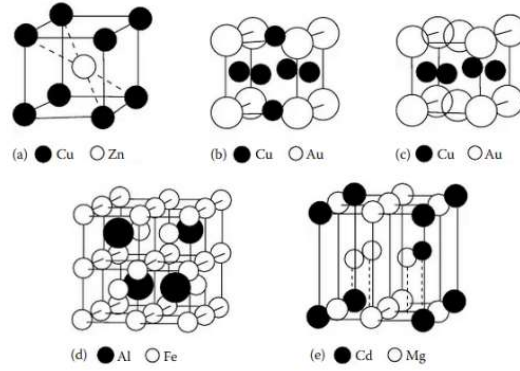
Figure 1-2 The most common ordered lattices: a) L20: CuZn, FeCo, NiAl, FeAl, b) L12: Cu_3Au, Au_3Cu, Ni_3Mn, Ni_3Fe, Pt_3Fe; c) L1$_0$: AuCu, CoPt, FePt; d) D0$_3$: Fe_3Al, Fe_3Si, Fe_3Be, Cu_3Al; e) D0$_{19}$: Mg_3Cd, Cd_3Mg, Ti_3Al, Ni_3Sn. After [16]

1.4. Chemical ordering in the Au-Cu-Ag ternary system

18-karat red gold belongs to the Au-Cu-Ag ternary system. This system is characterized by chemical ordering in the Au-Cu system, a miscibility gap in the Ag-Cu system and complete miscibility in the Au-Ag system[2].

Figure 1-3 a-c displays the binary phase diagrams for the Au-Cu, Au-Ag and Cu-Ag binary alloys, respectively.
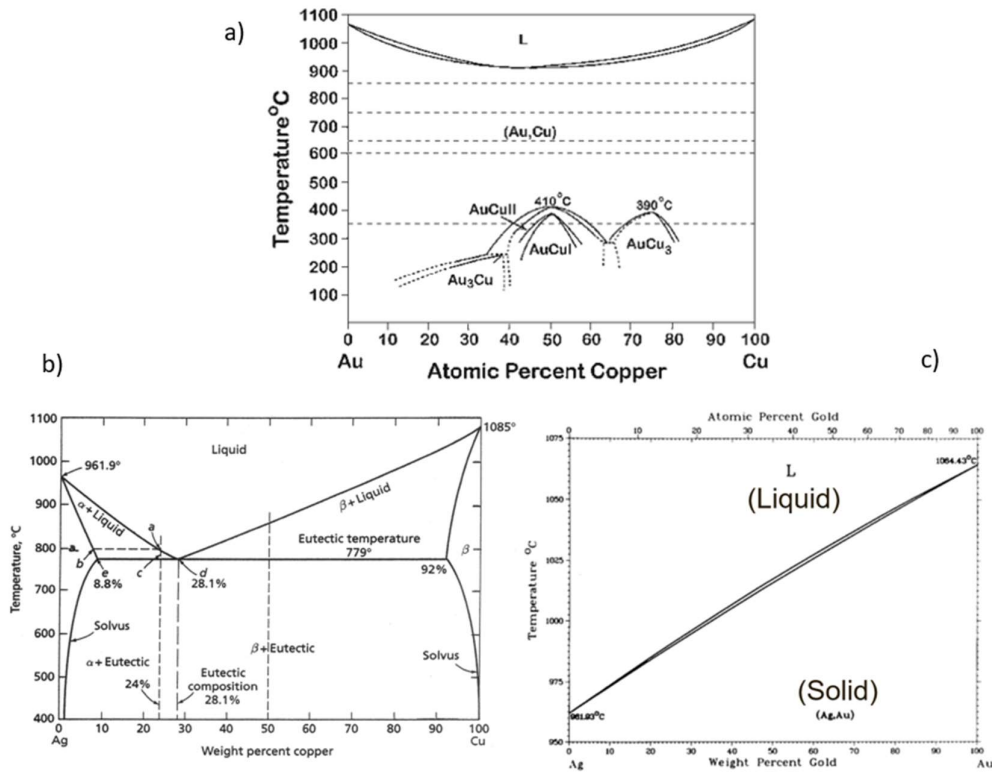
Figure 1-3 Binary phase diagrams of a) AuCu; b) AgAu and c) AgCu from [17]

The Au-Cu system is characterized by a high temperature solid solution for all compositions, i.e. disordered α-AuCu phase, where the Au and Cu atoms randomly occupy a face-centered-cubic lattice (A1-type structure). Below a certain temperature, depending on the composition, different chemically ordered phases form. Namely, the Au3Cu, AuCu I, AuCu II and AuCu3 ordered phases. Figure 1-4 displays the ordered structures present in the Au-Cu system. At the left and right sides of the phase diagram in Au-Cu phase diagram (Cu=<25% at. and Cu>=75% at.), chemical order takes place by the segregation of Au or Cu atoms to the corners of the FCC lattice, while the lattice positions located at the faces of the cubic lattice are occupied by unlike atoms. This ordered structure is known as a $L1_2$-type.

α-AuCu (A1) Au₃Cu (L1₂) AuCu I (L1₀) AuCu₃ (L1₂)
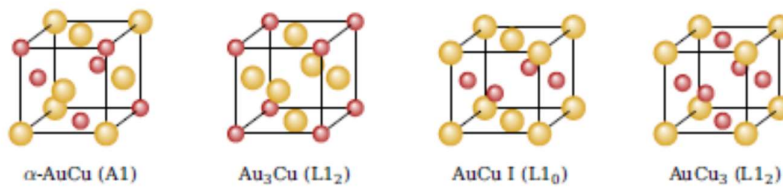
Figure 1-4 Chemically ordered phases present in the Au-Cu system. Image from [18]

At the equiatomic composition, the disordered phase first transforms into AuCu II phase (T>380°C, T<410°C) and then to AuCu I (T<380°C)[2]. It is easier to describe the AuCu I phase before understanding the structure of the AuCu II phase. Chemical ordering in AuCu I occurs by alternating {002} planes of only gold and only copper atoms along the c-axis. The significant atomic size difference between the Au and Cu atoms results in a considerable lattice contraction along the [001], which breaks the cubic symmetry (c/a=0.92) and results in a $L1_0$-type structure (space group *P4/mmm*). It is noted that this phase exhibits a body-centered-tetragonal (BCT) Bravais lattice. However, it is common practice in literature to adopt the FCT cell, which has the same orientation of the basis vectors as the FCC cell. This allows an easy comparison to the FCC parent phase. In this research, the FCT representation of the $L1_0$ structure is adopted.
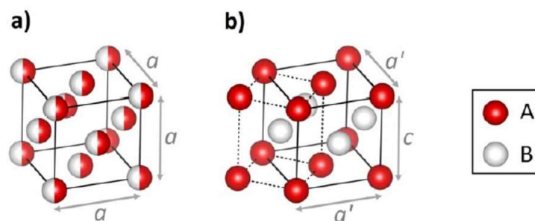
Figure 1-5 a) FCC lattice of the chemically disordered phase (A1-type structure); b)BCT and FCT representations for the chemically ordered phase ($L1_0$-type structure) [19]

The AuCu II phase is a long period structure consisting of $L1_0$ units that stack along the [100] or [010] [20,21] with periodic anti-phase boundaries, as depicted in Figure 1-6. The antiphase boundaries

delimit L1$_0$ cells with the same lattice orientation but with a Cu-layer out of step. At the anti-phase boundary, Cu shifts towards the boundary while gold shifts away[22,23].
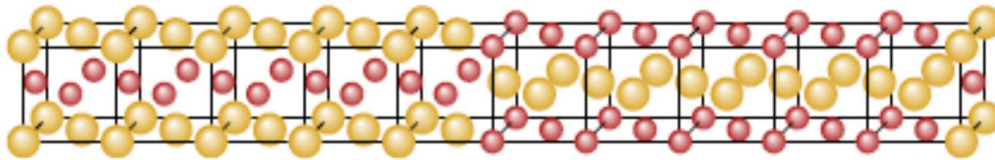
Figure 1-6 Lattice cell of the AuCu II phase

Additionally, considerable atomic disorder has been reported to exist at these boundaries [23,24].The number of cells between two antiphase boundaries is denoted by the M parameter. For the AuCu II phase depicted in Figure 1-6, the M parameter equals to 5 and the length of the lattice parameter b=10a, being a the lattice parameter of the L1$_0$ cell. Indeed, AuCu II is an incommensurate structure and the M parameter fluctuates around an average value[20,25]. This ordering transition has been reported to be sluggish and is generally not observed when the system is out of thermal equilibrium conditions even after long annealing times [26].

An immiscibility gap spans the entire composition range of the Ag-Cu system given the positive enthalpy of mixture of the alloy. This means that Ag and Cu atoms repel each other in solid solution and have a strong tendency to form a mixture of two phases. On the other hand, Au and Ag show complete miscibility over the entire compositional range.

The structural transitions of the binary alloys prevail in the ternary system. The calculated isothermal section at 300°C for the Au-Cu-Ag system [27] in Figure 1-7 predicts the presence of the AuCuAg solid solution, i.e. α, and the ordered Au-Cu phases, i.e. AuCu$_3$, AuCu I and AuCu II. The immiscibility gap is evidenced by the appearance of α' and α'' phases, which denote AuAg- and AuCu-rich solid solutions, respectively.
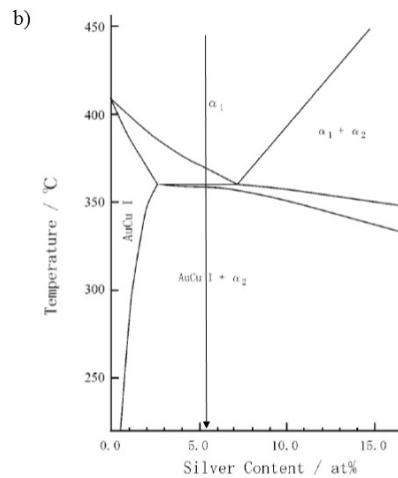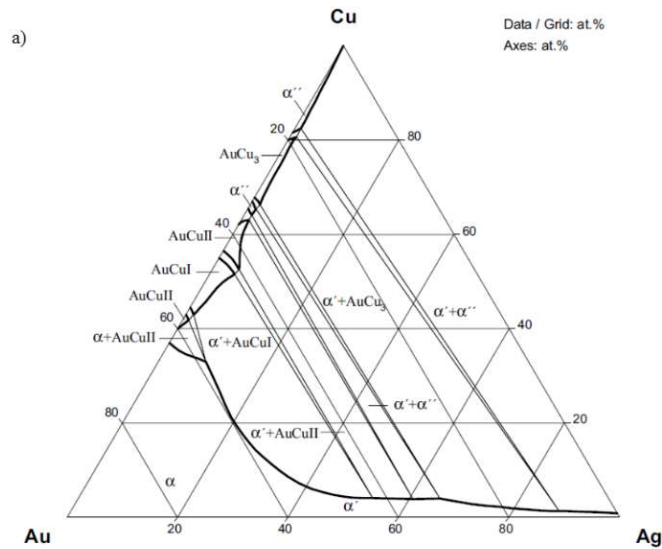
Figure 1-7 a) Predicted isothermal section at 300°C for the Au-Cu-Ag ternary system [27]; b) Predicted pseudo-binary AuCu-Ag diagram from [28]. The arrow indicates the chemical composition of red gold.

The 18 karat red gold composition (51.1Au-45.5Cu-5.6Ag in %at.) falls within the compositional range that undergoes AuCu-I chemical ordering, see Figure 1-7b. For the red gold composition, indicated with an arrow in Figure 1-7b, the presence of AuCu I and α_2 are predicted at room temperature. The latter phase corresponds to a solid solution of Au and Ag with a face centered cubic structure. Application of the Lever rule results in 97% AuCu I and 3% α_2 phase at room temperature. Several authors have confirmed the formation of the α_2 phase in AuCu alloys with small additions of Ag, with a lattice parameter of a=4Å [7,8,29–35].

1.5. Crystallographic aspects of the L1$_0$ phase

The phase transformation A1 → L1$_0$ reduces the point group symmetry and the translational symmetry of the original FCC crystal. While the FCC crystal shows three fourfold axes, after chemical ordering,

the crystal lattice only has one fourfold axis that gives raise to three orientational variants. Each orientational variant aligns the c-axis along one of the three cubic directions of the parent FCC lattice; see Figure 1-8a-c.
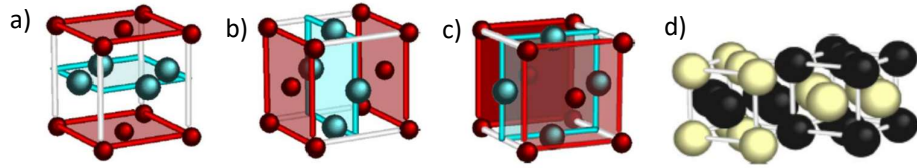
Figure 1-8 a-c) Representation of the three L10 orientational variants; d) Representation of two L10 sublattices in anti-phase relation. Images from [36]

During the A1 →L1$_0$ transition, the translational symmetry is reduced by half. This means that the same orientational variant can show two sublattices in-step or out-of-step relation to each other, i.e. in-phase or out-of-phase. Figure 1-8d shows two sublattices in out-of-step configuration. A schematic of ordered nanodomains embedded in a disordered matrix is illustrated in Figure 1-9a. The micro-domains labelled as 1, 4 and u are in-phase with one another, while the same happens for the others. However, the former group is out-of-phase with the latter group. These are the so-called anti-phase domains. The coalescence of two anti-phase domains forms the antiphase boundaries (APB) as shown in Figure 1-9b. APBs can be observed by transmission electron microscopy techniques. In summary, six distinct sublattices (3 orientational variants with 2 translational configurations) can form upon the A1→ L1$_0$ phase transformation.
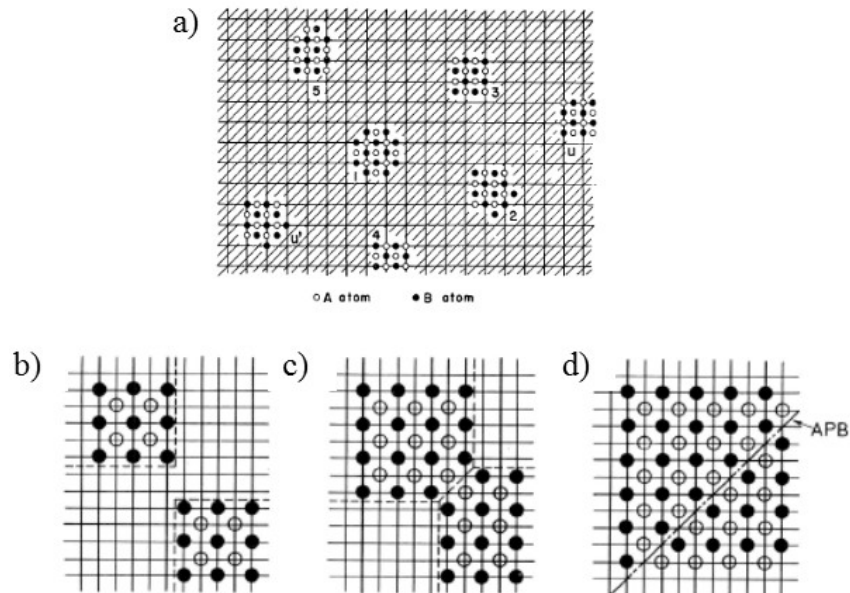
Figure 1-9 a) Ordered domains embedded in the disordered matrix, after [37] b) Schematics of the formation of an APB upon the growth of nuclei of different sublattices. b) ordered domains in antiphase relation; b) contact of the domains, c) formation of APB from [38].

1.6. Influence of silver in the $L1_0$ ordering

A1 → $L1_0$ ordering is a first order diffusional phase transition that generally follows a nucleation and growth process. Kinetics studies have been performed on equiatomic AuCu by measuring the electrical resistivity as a footprint of order as well as by means of differential scanning calorimetry experiments [39–43].

The diffusional character of this solid-state transformation makes ordering very sensitive to the presence of quenched-in excess vacancies. Increasing excess-vacancy density enhances the ordering rate [44] and reduces the onset temperature for $L1_0$ ordering [45]. A similar influence of the excess-vacancy density has been observed in $L1_2$- and B2- type ordering transitions [46]. Resistometric heating experiments[45] revealed three stages of ordering in quenched equiatomic AuCu. These were correlated to the mobility of divacancies, mobile defects and single vacancies. The activation energy for the migration of a pair of divacancies is lower than that for a vacancy in quenched gold [47]. Based on the obtained activation energies for each stage, this study concluded that no domain growth was necessary for full order.

The addition of silver slows down the ordering kinetics by lowering the ordering temperature[29,48], decreasing the activation energy and the ordering rate[49] compared to the binary AuCu alloy. Table 1-1 compares the reaction rate constant (K_0) and the activation energy (Ea) for equiatomic AuCu and an alloy with a considerable silver addition Au53Cu36Ag11 alloy.

Table 1-1 Comparison of the reaction rate constant (K0) and the activation energy for equiatomic AuCu and Au53Cu36Ag11.

Alloy	K_0 (min^{-1})	E_a(kcal/mol)	Reference
AuCu	4.46 x 10^{10}	29	Dienes[42]
Au53Cu36Ag11	7.8 x 10^7	20	Yasuda[49]

Yasuda ascribed the reduction in the ordering rate to the fact that silver atoms partially released the stress field induced by the formation of the $L1_0$ phase [49]. It has been reported that additions of silver up to 6%at. restrain significantly the AuCu I formation[50].

1.7. Microstructural evolution during $L1_0$ ordering

The most comprehensive microstructural study of AuCu ordering by means of transmission electron microscopy was performed by Hirabayashi and Weisman[51]. Three microstructural stages were identified after isothermal annealing experiments. 1) Formation of plate-like $L1_0$ nuclei coherent with the disordered matrix in the $(110)_d | (101)_o$ orientation relationship after low temperature annealing at 150°C. 2) micro-twinning on (101) planes after intermediate temperature annealing at 250°C for

2h. 3) macro-twinning on (101) planes after long time annealing at 250°C for 4h. Figure 1-10 shows the characteristic micrographs of each stage of ordering observed by transmission electron microscope.
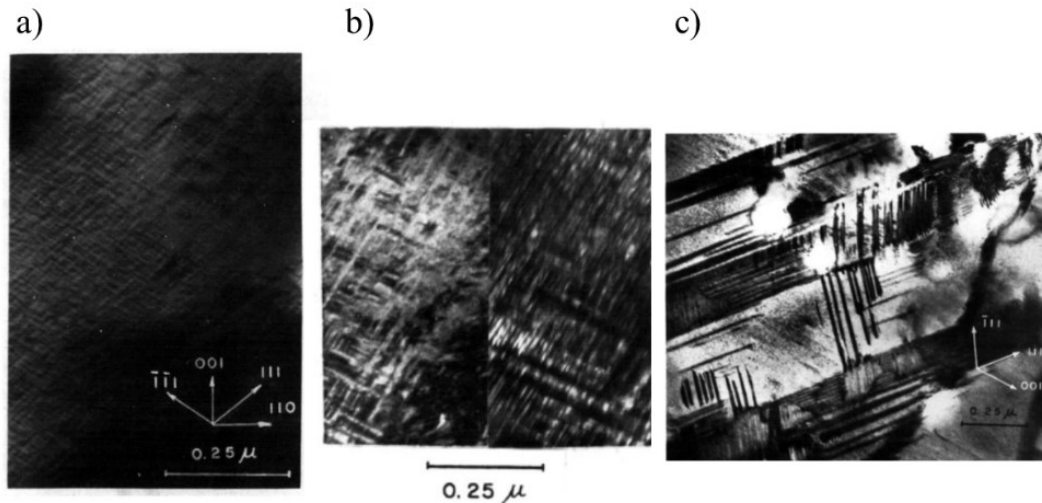
Figure 1-10 TEM micrographs at different ordering stages. a) BF image showing coherency strain contrast at the early stages of ordering, b) BF and DF image showing a microtwinned microstructure and c) BF image showing a twinned and fully relaxed microstructure. From[51]

During the early stages of $L1_0$ ordering, ordered domains form coherently within the disordered cubic matrix [51,52]. The three $L1_0$ orientational variants are randomly distributed in the disordered matrix. The coherency between the ordered domains and the disordered matrix produces large tensile strains parallel to the c-axis of the ordered domains, and little compressive strain along the directions normal to it. This is identical to the strain distribution of G.P. zones in Al-4Cu [53]. The $(101)_{fct}|\{110\}_{fcc}$ orientation relationship between the ordered and disordered is planes of the matrix is thought to minimize the coherency strain[44].

At this stage, the growth of the domains results in increasing non-local and long-range shear strains in the matrix [54–56]. Figure 1-11a shows the geometric distortion induced by a $L1_0$ coherent precipitate in the cubic matrix. Tanner [57] suggested that coherent precipitates with tetragonal distortion induce elastic shear on {110} planes along the <1-10> cubic directions when the matrix shows a high elastic anisotropy. Investigations during the early stages of $L1_0$ ordering in CoPt [58,59] suggested the occurrence of a monoclinic deformation of the matrix as a result of <1-10>{110} slip. It was suggested that the TEM observations in AuCu [51] also indicated monoclinic distortion in the cubic phase as well as in Ni-Be and Cu-Be alloys[60]. At this stage a rapid hardening is observed referred as the *order hardening effect* [3,4,39], see the initial hardness increase at annealing times below 20min in Figure 1-11b.

a)   b)
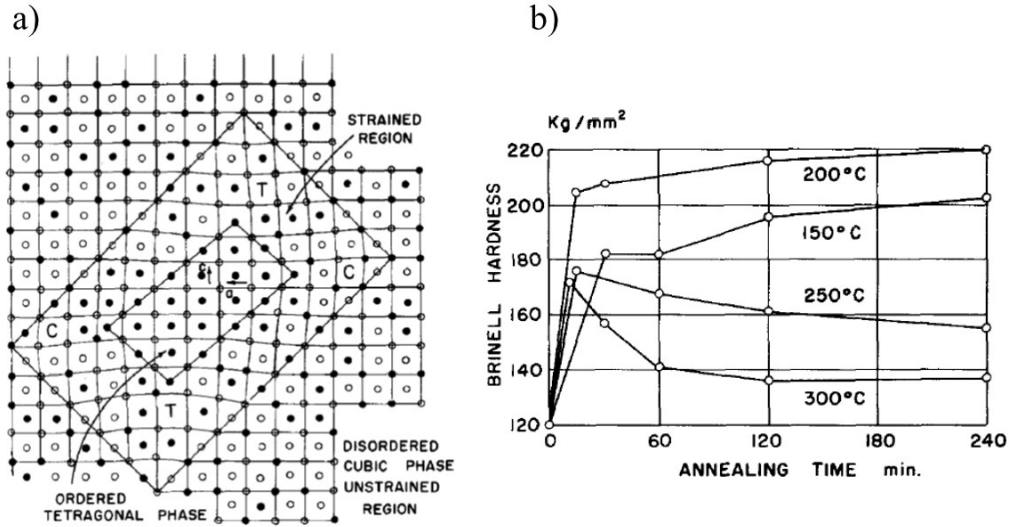
Figure 1-11 a) schematics of a coherent domain within the disordered matrix, showing the distortion due to tetragonal strains[51] b) Hardening upon isothermal ageing at different temperatures[3]

TEM microstructural observations in pseudo-binary AuCu-6Ag reported a similar microstructural evolution as in equiatomic AuCu [61–63]. Figure 1-12 compares the hardening behaviour of equiatomic AuCu (alloy No 1) and alloys with low silver content (alloy No 2, AuCu-5.6Ag) and high silver content (alloys No 4 and 6, Au36.2Cu41.4Ag22.4 and Au33.4Cu35.5Ag31.1, respectively). The age-hardening mechanism in low silver content CuAu alloys is related to the AuCu I formation, as in equiatomic AuCu [5,33,64,65]. The addition of small amounts of silver to equiatomic AuCu results in a greater hardening and a delayed softening stage, the former is attributed to the slower ordering rate and the latter to the high densities of twin boundaries and antiphase boundaries[66].
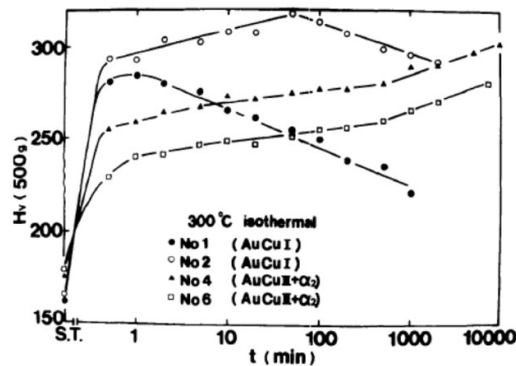
Figure 1-12 Age hardening curves at 300C as a function of annealing time for alloys: No 1: AuCu, No 2: AuCu-5.6Ag, No 4: Au36.2Cu41.4Ag22.4, No 6: Au33.4Cu35.5Ag31.1 [66]

Upon further ordering, short-range strain accommodations take place in the form of micro-twinning on (101) planes of the ordered phase[51,67], which result in a regular alternation of unique c-axis directions, see Figure 1-13a-b. The onset of micro-twinning is correlated with the softening of the

12

alloy, see Figure 1-11c. Slade and co-workers[67] showed that the first maximum of the elastic stored energy and its decline was associated with the maximum and decline of coherency strains between the AuCu I nuclei and the disordered matrix. Figure 1-13c shows the evolution of the elastic strain energy as a function of annealing time at 125°C. The first decline in the strain energy was attributed to the onset of micro twinning.
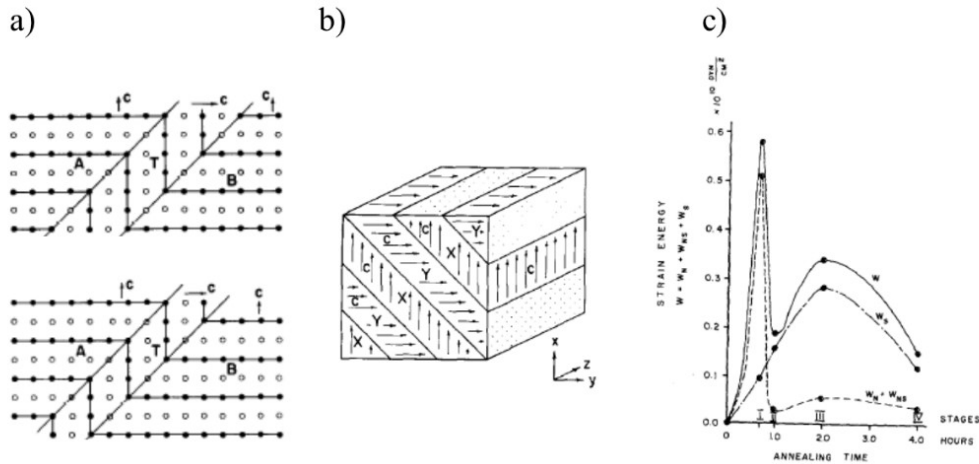
Figure 1-13 a) Schematic drawing of micro-twinning with the A and B sublattices domains in-step; b) Schematic drawing of micro-twinning with the A and B sublattices domains out-of-step;. c) Regular alternation of c-axis direction in AuCu I resulting from micro twinning. Twin interfaces are parallel to (101). Figure from reference [ref] c) Evolution of the internal strain of the system during the development of ordering[67]

Upon further development of ordering, coarse (101) lamellae accommodate long-range strain gradients arising from ordered lattice regions with different c-axis orientations[51,68]. When adjacent antiphase domains coalesce, they show anti-phase boundaries along [100]. Generally, APBs appear before twinning.

Other microstructural strain relief mechanisms

The rate of ordering controls the set-in of strain-relief mechanisms; in some cases, it is so fast that rapid strain-relief mechanisms, other than twinning, appear. Reported microstructural strain-relief mechanisms are grain boundary migration[4], fracture [4,69,70], surface relief [71,72] and shape changes[71,73]. Figure 1-14a-b illustrates intergranular fracture upon isothermal ageing at 340°C for 1h. Shape restoration studies in equiatomic AuCu and AuCu-6Ga reported that initially disordered samples underwent shape distortion after ordering treatments; see Figure 1-13 upper and middle images. When re-disordered, the initial shape was restored as shown in Figure 1-13 lower image. This implies that equiatomic AuCu has a shape memory effect [71,74]. Furthermore, it has been suggested that shape distortions depend on the grain size and the specimen geometry [71].
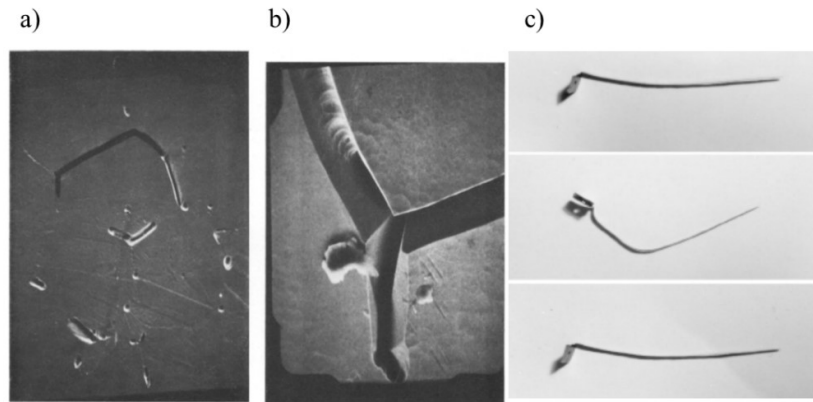
Figure 1-14 a), b) scanning electron micrographs of fracture in quenched AuCu and ordered at 340°C for 1h from [4]. c)s hape distortion of a thin sheet with 0.75mm width of AuCu-6Ga alloy as a function of the AuCu-I $L1_0$ ordering. upper) Initial condition disordered FCC; middle) condition after ordering at 100°C for 5min; lower) re-disordered condition[71]

<u>*$L1_0$ ordered domains after cooling and above the T_{OD} temperature*</u>

A microstructure consisting of stable antiphase domains within the disordered matrix at temperatures between T_{OD} and 50°C above T_{OD} was reported by electron diffraction studies of AuCu at temperatures above T_{OD} [75]. The same microstructure was reproduced by computer simulations of the atomic arrangement of AuCu above T_{OD} [76], with an average inter-domain distance of 15-20⍰. These simulations predicted that fast quenches produced the same microstructure. Later on, electron microscopy studies on water-quenched AuCu from above T_{OD} revealed the presence of a high density of ordered domains that extend 2nm in size within the cubic matrix [77].

X-ray diffraction kinetics studies on AuCu samples reveal two broad maxima around the (110) super-lattice reflection at the early stages of ordering or at temperatures close to T_{OD}, instead of the expected single peak [78–82]. This X-ray feature was also reported on the $AuCu_3$ system by Guinier and co-workers [83,84]. Later on, Hashimoto [37,85,86] published the correlative micro-domain model for ordered alloy structures, which reproduces the diffuse scattering maxima observed around the (110) super-lattice reflection. The explanation for this diffraction phenomenon are the periodic short-range spatial correlations of nano-domains with parallel c-axis but in an antiphase relation.

1.8. Influence of applied stress on $L1_0$ ordering

Hirabayashi reported [87] that the application of compressive stress during ordering of a AuCu monocrystal resulted in a preferential orientation of the $L1_0$ c-axis along the cubic axis parallel to the stress direction. This was defined as the *stress-ordering* effect. Other studies [88] reported that applied tensile stresses during ordering resulted in $L1_0$ domains aligned with their c-axis perpendicular to the stress direction, causing an enhanced strength of the alloy. A similar behaviour has been observed in other A1→$L1_0$ systems, where applied external stress or magnetic fields during ordering result in the prevalence of a favourably oriented variant [89,90]. Kulovits et al. [91] suggested that the

internal stresses generated during plastic deformation (e.g. cold work) could have a similar influence in the selection of preferred $L1_0$ orientational variants. A recent study performed by Larcher [92] showed that chemically disordered 18-karat red gold wires that were plastically deformed into a U-shape and subsequently ordered resulted in preferential $L1_0$ variant selection in the tension-compression zones.

Kinetics studies reveal that $L1_0$ ordering in FePd under elastic external stress fields show an enhanced ordering rate and transformed volume fraction. This was ascribed to an enhanced nucleation rate and the development of an internal stress field that favours $L1_0$ formation [89,91,93]. Computer simulations based on the time-dependent Ginzburg-Landau approach[94,95] show that the presence of elastic external stress fields increase the ordering rate, related to the reduction of elastic strain energy in the system. Same tendencies have been observed in other ordering systems, notably $L1_0$-type FePt [96], the $L1_0$ type FeNi [97]and $L1_1$-type CuPt [98]. Furthermore, $L1_0$ ordering in previously cold rolled FePd show enhanced ordering kinetics with greater ordering rate and higher degree of order as compared to undeformed samples[99]. Interestingly, order hardening has been reported to be greater for quenched AuCu specimens than for cold worked specimens[4].

It is well known that dislocations can act as preferential sites for nucleation of precipitates[100]. Electron microscopy studies performed by Hunt and Pashley [101] observed preferential nucleation around dislocations during AuCu II ordering. They suggested two possibilities for the preferential ordering around a dislocation: 1) the strain fields around the dislocation accommodate more readily the tetragonal distortion of the ordered phase or 2) the local chemical composition changes around the dislocation modify the critical temperature for ordering. The latter, which seems unlikely in equiatomic compositions, is however possible in ternary systems[102]. Investigations on $L1_2$ ordering suggest that dislocations enhance ordering due to the production of vacancies [103].

1.9. Influence of other addition elements on the $L1_0$ ordering transformation in AuCu

In general, small amounts of additional elements to equiatomic AuCu keeps the compositional range of single phase AuCu. Addition of Pd increases the corrosion resistance greatly while reducing the ordering rate of AuCu I [104,105]. Pd-Cu-Au shows for a wide compositional range the presence of AuCu I as ordered phase[106]. However, depending on the chemical composition, it can stabilize the $AuCu_3$ phase [8]. Hardening is attributed to the formation of AuCu I, but the age hardenability is reported to be lower. Nucleation and growth as well as spinodal ordering has been observed in these alloys [107].

Addition of Pt increases the T_{OD} [108] and enhances mechanical properties both at high and normal temperature [109]. The age-hardening is characterized by an order-twinning process initiated by spinodal ordering [32].

Addition of Zn greatly increases the hardening rate and delays the softening stage. The density increase of APBs is thought to be the main cause for the softening delay [110–112].

Chapter 2   Experimental

2.1. Materials

Two gold-based alloys have been investigated in the course of this dissertation. On the one hand, 18-karat red gold alloy constitutes the main alloy under study. On the other hand, an 18-karat red gold alloy with minor changes to the chemical composition by addition of Sn and Pd is investigated in the last chapter of this dissertation. 18-karat red gold belongs to the gold-copper-silver ternary system. Table 1 shows the chemical composition of red gold in atomic and weight percent.

Table 2-1 Chemical composition of red gold alloys

	Au	Cu	Ag	
Red gold	51.1	43.2	5.6	Atomic percent
	75	20.5	4.5	Weight percent

Figure 2-1 shows the predicted AuCu-Ag pseudo-binary phase diagram [28]. At the red gold composition, as indicated by the black arrow in the same figure, the solid-state transformation path from high temperature follows:

$$\alpha_1 \rightarrow \alpha_1 + \alpha_2 + \text{AuCu II} \rightarrow \alpha_2 + \text{AuCu II} \rightarrow \alpha_2 + \text{AuCu II} + \text{AuCu I} \rightarrow \alpha_2 + \text{AuCu I}$$
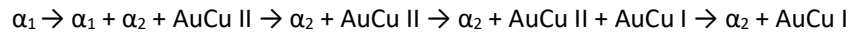
with, α_1 as AuCuAg solid solution with A1-type structure; α_2 as AuAg solid solution with A1-type structure; AuCu II as the chemically ordered PAP structure and AuCu I as the chemically ordered $L1_0$ structure. At room temperature, this alloy undergoes chemical ordering and decomposition resulting in 97% AuCu I and 3% AuAg.
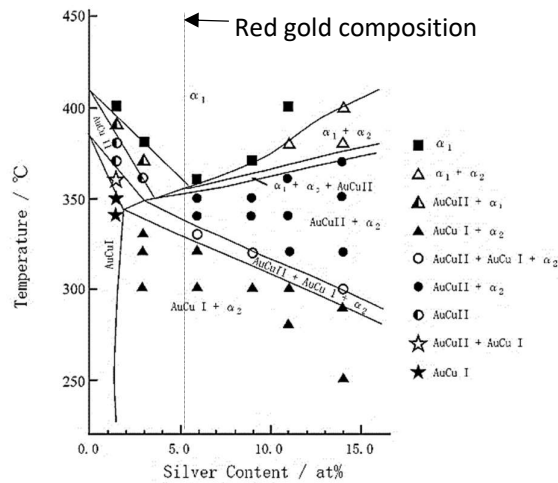
Figure 2-1 Pseudo binary AuCu-Ag phase diagram [28]

Small additions of Pd and Sn modify the chemical composition in 18-karat red gold, resulting in a slight reduction of Cu and Ag content. This modification improves the corrosion resistance of red gold alloy without modifying the colour nor the gold karatage of the alloy. From here on, this alloy will be identified as the modified red gold (MR). Alloying with Pd and Sn is such that the A1 $\rightarrow$ L1$_0$ ordering transformation remains the major phase transformation [107,113]. The Pd and Sn addition lies within the range 0.1% - 1.1% and 0.1% - 2%, respectively and in weight percent (developed and patented by Richemont International S.A.). Sn is known to improve the anti-oxidative properties of the melt while Pd substantially improves the corrosion properties of the alloy.

2.2. Processing

Industrial specimens

Traditional industrial manufacturing of precious alloys starts from a static or continuous casting furnace followed by a series of thermal and cold working operations. Typical thermal treatments are homogenization, recovery, recrystallization and ordering treatments. Cold forming operations such as rolling and drawing are usually followed by recrystallization heat treatments. Straightening operations usually follow thermal treatments and correct for shape deviations. Semi-finished parts are obtained by shape forming operations such as forging, bending, cutting and machining. In general, the mechanical operations induce heterogeneous plastic deformation in the parts. In particular, metalworking of red gold requires more frequent recrystallization heat treatments as compared to other 18-karat gold-based alloys.

At VARINOR S.A., the fabrication of U-shaped parts from rectangular wires with 2 x 4 mm^2 cross-section is a prototype manufacturing process that reveals the complexity of working with red gold. Figure 2-2 shows the processing steps included in this manufacturing route, which start with a recrystallization treatment in a continuous furnace, followed by a straightening and a bending operation. Finally, two bent wires are furnace-brazed together.

Recrystallization shape: wire	Straigthening shape: wire	bending shape: U-shape	furnace brazing shape: U-shape
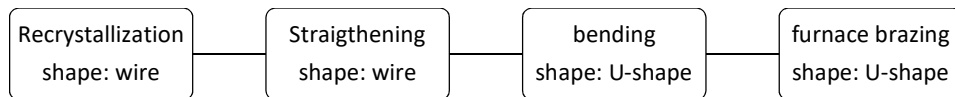
Figure 2-2 Manufacturing route for U-shaped parts

The dimensions and shape of the parts are controlled before and after the bending operation as well as before and after the furnace brazing operation. This is done with a LEICA optical instrument coupled with a customized software, capable of recognizing the shape of the part and compare it to the original drawings. Figure 2-3 shows the typical distortion of U-shaped samples after brazing. The distance

between the two ends of the sample is denoted as AE after the bending operation and AE' after the furnace brazing operation.

For the bent sample, the shape distortion is measured as the increment in the opening between the theoretical shape, AE$_{ref}$, and the shape of the sample after bending, AE. For the furnace brazed sample, the shape distortion is measured as the increment in the opening between the shape of the bent sample, AE and the shape of the sample after furnace brazing, AE'.
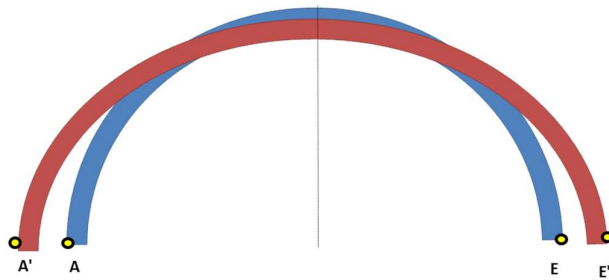
Figure 2-3 Schema of the shape distortion of U-shaped samples. Blue: before furnace brazing. Red: after furnace brazing

Figure 2-4 shows an example of the output from the software measuring the shape distortion, showing in red the regions where the shape distortion is critical. Note that, in general, the magnitude of the shape distortions are between 300µm-1000µm.
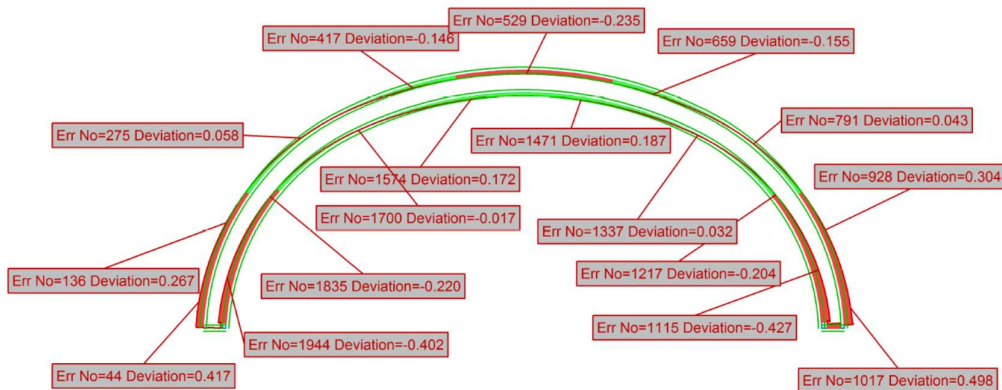
Figure 2-4 Example of the output of the dimensional control software. The shape of the sample before and after brazing is overlapped, red zones highlights distorted regions.

Within the framework of this project, VARINOR S.A. manufactured three batches of red gold samples, denoted as batch I, batch II and batch III.

Batch I investigates the influence of thermo-mechanical operations on the distortion of U-shaped samples. Five alternative manufacturing routes were undertaken, as summarized in Table 2-2. Each alternative route consisted in modifying one thermal or mechanical operation at a time. The modifications aimed at isolating the operation that had the greatest influence in the distortion of the samples. These included changing the recrystallization temperature, adding an annealing treatment or suppressing the mechanical operations. For each manufacturing route, samples were provided after each operation in the form of wires with 2 x 4 mm^2 cross section and 15cm length for the recrystallized and straightened samples; and in the form of U-shaped samples for the bent and furnace-brazed samples. All the samples underwent a metallographic inspection and dimensional control. Routes A and B underwent EBSD examinations and various samples from routes A, B and C underwent TEM observations and were investigated by synchrotron X-ray diffraction.

Table 2-2 Processing routes of the experimental batch I manufactured at VARINOR S.A.

Operation	Route A Recrystallization 660°C, 6 min		Route B Recrystallization 550°C, 6 min		Route C Recrystallization 550°C, 6 min
Recrystallization	660R-s		550R-s		550R-s
Straightening	660RS-s		550RS-s		✗
Bending	660RSB-s		550RSB-s		✗
Annealing 550°C, 6 min	✗	660RSBA-s	✗	550RSBA-s	✗
Furnace Brazing 860°C, 2.5min	660RSBF-s	660RSBAF-s	550RSBF-s	550RSBAF-s	550RF-s

Batch II deals with the influence of the cooling rate after recrystallization on the microstructural evolution during manufacturing, see

Table 2-3. A different cooling rate was obtained by performing the recrystallization treatment on a different continuous furnace (named furnace 2) as shown in Figure 2-5. Given the exponential behaviour of the natural cooling in a continuous furnace, the cooling rate is expressed as the linear fit between 350°C-200°C with values shown in Table 2-4. Samples were provided after each recrystallization heat treatment in the form of wires with 2 x 4 mm^2 cross section and 15cm length. The microstructural evolution of samples from route A (660R-s, 660RS-s), route B (550R-s,550RS,s), route A1 (660R-f, 660RS-f) and route B1 (550R-f, 550RS-f) were investigated by means of synchrotron X-ray diffraction in order to evaluate the influence of the previous cooling rate on the microstructure.

Table 2-3 Processing routes of the experimental batch 2 manufactured at VARINOR S.A.

Operation	Route A2	Route B2
	Recrystallization 660C, 6min	Recrystallization 550C, 6min
Recrystallization	660R-f	550R-f
Straightening	660RS-f	550RS-f
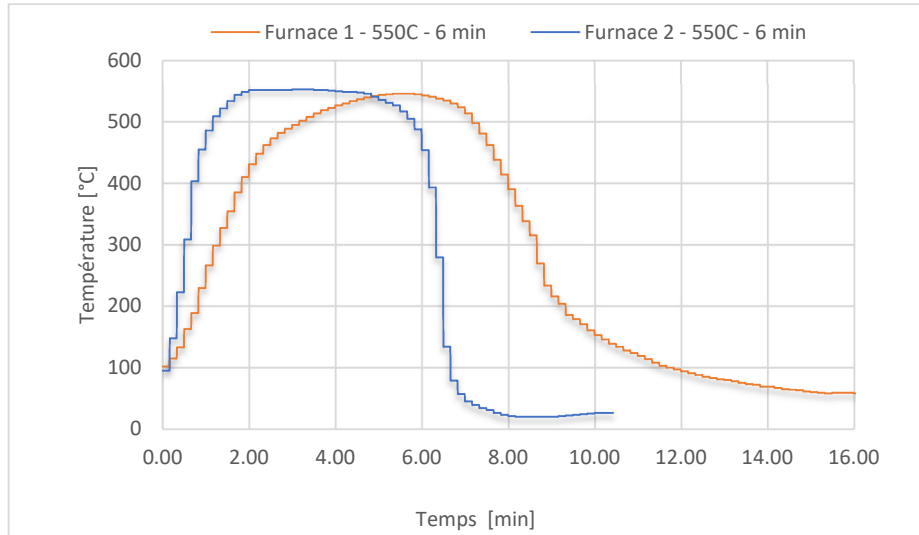
Figure 2-5 Thermal profile during a recrystallization heat treatment at 550°C on the continuous cooling furnace 1 (blue curve) and furnace 2 (red curve)

Table 2-4 Characteristic cooling rates for the furnaces 1 and 2, respectively.

Target temperature (°C)	Furnace 1 Cooling rate (°C/min)	Furnace 2 Cooling rate (°C /min)
550	-100	-700
660	-200	-700
860	-500	-

Batch III investigates the degree of ordering on isothermally aged wires at various ageing temperatures and durations, see Table 2-5. The ageing experiments were performed in tubular furnace under a mixed N_2/H_2 atmosphere. Samples were provided after each ordering treatment in the form of wires with 2 x 4 mm^2 cross-section and 15cm length. All the samples were analysed by means of synchrotron X-ray diffraction. Complementary electron microscopy studies were carried out.

Table 2-5 Isothermal treatments for experimental batch III manufactured at Varinor S.A.

Ageing temperature [^{o}C]	Duration [min]				
150	5	10	20		
200	5	10	20		
280	5	10	20		
310			20		
330				60	
330				720	

All thermal treatments except for the ones in batch III, including recrystallization treatments and furnace brazing, were performed on continuous furnaces under a reducing atmosphere with a N_2/H_2 mixture and a belt speed of 20 cm/min. The straightening machine was a cross-roll straightening machine.

It is noted that the high copper content of these alloys makes them prone to room temperature ordering. A few days are required to manufacture and deliver the samples from VARINOR S.A. until Paul Scherrer Institute (PSI). All the samples were exposed to natural ageing during about 7 days. Once at Paul Scherrer Institute, samples are stocked at -20°C in a key-locked freezer (Froster-Labex 70, ADRO AG) to avoid any further ageing until experiments.

In situ specimens

VARINOR S.A. provided the alloys dedicated to *in situ* experiments, notably red gold (R alloy) and the modified red gold (MR alloy). The as-received condition of the alloys corresponded to a recrystallized state. The recrystallization treatment was performed at 550°C during 6 minutes in the continuous furnace with a fast cooling rate (-700°C/min). The samples were delivered in the form of wires with 2 x 4 mm^2 cross-section and 15cm length.

2.3. Metallography and hardness

Conventional optical metallography was employed for grain size distribution examinations for the industrial specimens of batch I. Wire cross-sections were embedded in conductive resin and polished-down to a mirror-like surface. SiC grinding papers in decreasing particle size (*P320, P500, P800, P1000, P1200, P2500 and P4000*) were employed using water as lubricant. The relatively soft character of gold alloys requires coarse grinding from P320. Optical imaging of the grain structure is possible after chemical etching with a 50:50 (vol. %) solution of a saturated mixture of H_2O and chromium trioxide with chloridric acid at room temperature for around 120s. Metallographic analysis was performed in standard optical microscopes.

A Vickers hardness instrument was used for hardness studies with a diamond pyramidal indentor. Schematics of the indentation process are shown in Figure 2-6. The hardness number (HV) is calculated as the ratio F/A, where F is the force applied to the diamond in kilogram force and A is the surface area of the indentation in square millimetres. Given the fixed geometry of the indenter, a reasonable approximation of the hardness number can be obtained from Equation 2-1, where F is the force in kilogram force and d the diagonal of the indented area.
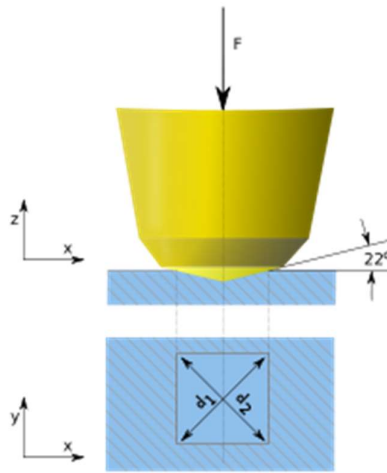
Figure 2-6 Schema of the Vickers micro-indentation geometry

Equation 2-1 Formula to calculate the Vickers number (micro-hardness)

$$HV = \frac{1.8544F}{d^2} \left[\frac{kgf}{mm^2}\right]$$

Micro-hardness profiles were performed along the transverse and normal directions of the cross-section under a load of 10N and a loading time of 20s. The minimum distance between the indentations and the distance from the indentation to the edge of the specimen followed the standard ISO 6507-1.

2.4. Electron microscopy

2.4.1. Scanning electron microscopy

Scanning electron microscopy (SEM) investigations included mostly electron back-scattered diffraction (EBSD), which is a scanning electron microscope-based technique that provides with crystallographic information within a wide length scale, ranging from tenths of nanometres to millimetres. This technique determines the local crystal structure and orientation at the surface of the specimen from electron back-scattered diffraction patterns made up of Kikuchi bands[114].

Preparation of SEM specimens

Sample preparation consists in embedding the gold alloys in carbon conductive resin and finely polish down from P4000 grit to 3µm and 1µm water-based diamond suspensions, with a final step of chemical etching based on HCl and H_2CrO_4 (50:50 %vol.).

SEM investigations

EBSD investigations were performed in a field-emission scanning electron microscope (FEG SEM) Zeiss ULTRA 55 equipped with EDAX Hikari Camera operated at 20kV with a 120µm aperture and high current mode. The pattern acquisition software was TEAM software with 4 x 4 binning and 8 bands condition for pattern recognition. For the phase ID analysis, the pure AuCu FCC CIF crystal structure was used from the Crystallographic Open Database (COD). For texture analysis, the step size was fixed to 1µm. Post-processing was performed using EDAX OIM Analysis 7.3. Texture analysis was performed via grain orientation mapping with inverse pole figures and pole figures.

2.4.2. Transmission electron microscopy

Transmission electron microscopes (TEM) are the most powerful microscopes, able to achieve 50 pm resolution in annular dark-field imaging and magnifications up to 10,000,000×. TEMs provide with local topographical, morphological, compositional and crystalline information, producing high-resolution images. The working principle of the microscope is to shine a high-energy electron beam through a very thin lamellae (<100 nm thickness and ≤3mm in diameter) and record the resulting diffracted beam in a CCD camera, which allows studying the atomic structure of the material and performing fine structure imaging of the microstructure.

In this project, transmission electron microscopy (TEM) was used to examine the microstructure of all manufactured alloys and in particular the features of ordered nano-precipitates within a grain of the matrix. The explored operation modes are the selected area electron diffraction (SAED), bright-field imaging (BF), dark-field imaging (DF), high-resolution imaging (HRTEM) and energy dispersive spectroscopy in scanning mode (STEM - EDS). Figure 2-7 illustrates the different configurations of the TEM column to produce each TEM mode.
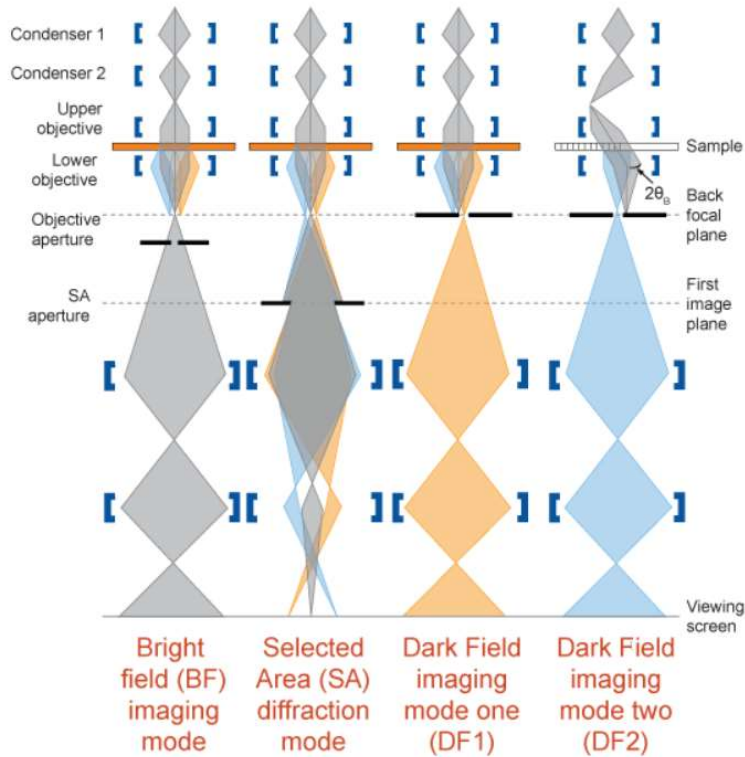
Figure 2-7 Working modes of a transmission electron microscope [115]

The SAED mode allows obtaining the electron diffraction pattern of a selected region (or grain) in the specimen. The selected area aperture is a metallic sheet that contains different hole sizes and is located below the sample holder on the TEM column. This aperture is movable and blocks all the electrons except from the ones passing through the hole, therefore the aperture can select a particular area and only this section will contribute to the diffraction pattern on the screen. This mode allows correlating atomic structures with regions of the sample.

The direct or transmitted electron beam generates BF images. The objective aperture located below the specimen selects the unscattered electron beam, enhancing the contrast of the image. Areas that strongly scatter or absorb electrons appear dark, whereas areas that transmit electrons appear brighter. For instance, this mode allows imaging coherency strain contrast.

DF images are produced by blocking the direct or transmitted beam and only allowing scattered electrons to form the image. The regions where no scattering occurs appear dark. This method is very useful for imaging e.g. ordered nano-domains using a diffracted beam of the superstructure (superstructure diffraction spots reflecting the presence of chemical ordering in a structure characterized by fundamental diffraction spots) to form the image.

High-resolution TEM imaging is a phase contrast technique that allows direct imaging of the atomic structure of the specimen. The contrast of a HRTEM image results from the interference in the image plane of the electron wave itself.

The scanning transmission electron microscopy (STEM) mode allows performing chemical mappings on the specimens. Information on the elemental composition is obtained by energy dispersive X-ray spectroscopy. The detection of elements in very low concentration is an inherent limitation of this technique.

An excellent and comprehensive guide for the interpretation of electron micrographs was found in Edington's *Practical guide for electron microscopy in materials science* [116].

Preparation of TEM specimens

A detailed description of the various sample preparation strategies that were undertaken in the course of this investigation follows. Most of the preparation was performed at the Interdisciplinary Centre for Electronic Microscopy (CIME) of the EPFL.

Note that the soft character of gold and copper results in a high sensitivity to thin film damage during the lamellae preparation process. Additionally, the high absorbing power of gold-rich alloys requires extra thin samples. This results in a challenging sample preparation and practical limitations such as e.g. simultaneous imaging of dislocations and ordered precipitates.

a) Cryo-ultramicrotomy

Cryo-ultramicrotomy is a fast and effective technique to produce very fine TEM lamellas. This technique forms thin sections with homogeneous thickness in very soft materials. The specimen is fixed on a cantilever arm and cooled down in liquid nitrogen. The cantilever arm moves up and down, such that a cold diamond knife slices up thin sections as shown in Figure 2-8 a). Wet- sectioning consists in collecting the thin sections in a small water reservoir placed on top of the diamond knife; see Figure 2-8 b). The available instrument from the Interdisciplinary Centre for Electronic Microscopy (CIME) at EPFL was used. Unfortunately, BF imaging of the prepared samples revealed a strong layering effect due to the compressive stresses induced during the slicing operation as shown in Figure 2-9.
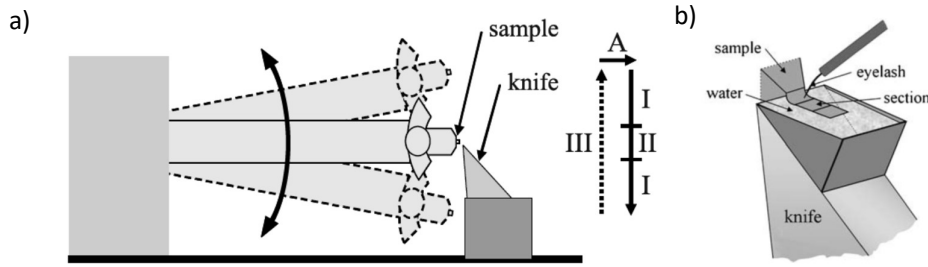
Figure 2-8 a) The ultramicrotomy working principle and b) wet-sectioning method, from [117]

Figure 2-9 TEM BF image of red gold prepared by cryo-ultramicrotomy.

b) Focused ion beam

Focused Ion Beam (FIB) is a popular micro-machining technique dedicated to TEM lamella preparation. The nano-meter scale resolution of the FIB allows selecting the region of interest in the specimen, e.g. grain boundary or a specific location in the cross-section. The preparation procedure starts by depositing a carbon mask on top of the region of interest that will protect the lamella from beam damage. Then, the front and back sides of the lamella are milled down to a thickness of 2µm, as shown in Figure 2-10a. The next step prepares the lamella for the lift-out. After milling out one of the two remaining sides, a nano-manipulator is attached to it by depositing carbon on the contact surface, see Figure 2-10b. The lift-out step is completed after milling-out the remaining side of the lamella. The next step consists in transferring the lamella to a TEM grid as shown in Figure 2-10c; the free side of the lamella is attached to the grid by depositing a carbon layer on the contact area and the contact with the nano-manipulator is cut. Finally, the lamella is thinned down to electron transparency by using decreasing beam voltages and current densities, see Figure 2-10d.

A dual beam (SEM/FIB) Zeiss NVision 40 instrument was dedicated to the TEM lamella preparation, with a 0.1-30kV Schottky field emission gun (FEG) and 1-30kV Ga liquid metal ion source. The SEM

resolution was 1.1nm at 20kV and 4nm at 30kV for the FIB. The gas injection system (GIS) consisted in a four channel single injector (carbon, platinum, insulator, water, XeF_2).
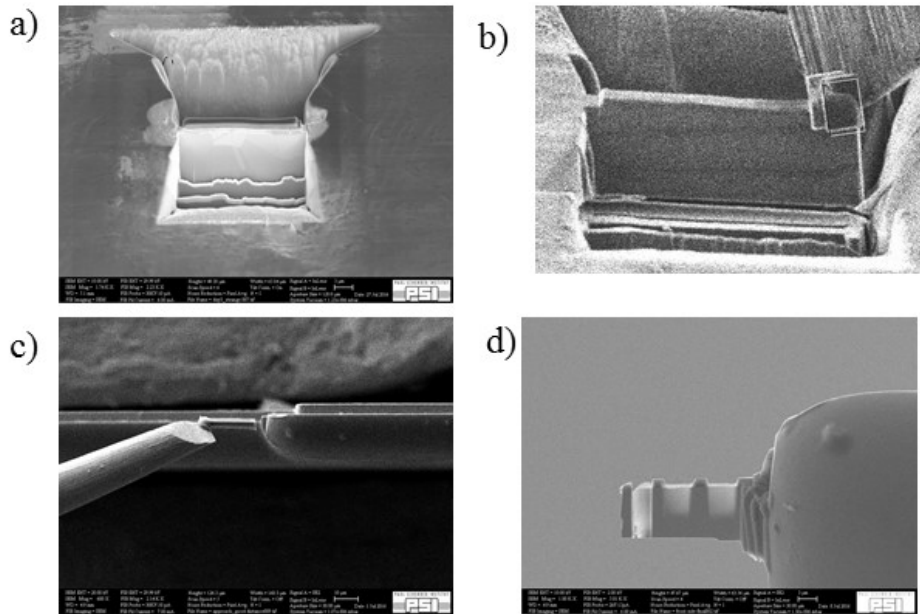
Figure 2-10 FIB preparation procedure. a) Milling down a lamella in the region of interest, b) lift-out with a nano-manipulator, c) transfer of the lamellae to a TEM grid and d) electron-transparent lamella

The first TEM lamella prepared by FIB was still too thick to be observed on the TEM. Further thinning-down was achieved by a fine Ar milling in a PIPS II instrument from GATAN. Typical FIB damage includes small irradiation clusters, observed as black and white dots in bright and dark field TEM images, respectively; small dislocation loops and eventually argon bubbles. These irradiation defects are not removed by the PIPS II, which can also produce similar defects. TEM BF imaging of polycrystalline copper samples exposed to a perpendicular ion beam at 30kV and 50pA was found to exhibit wavy patterns within the grains, which vanish under certain diffraction conditions, as shown in Figure 2-11. Such a wavy microstructure appears as a typical strain contrast due to beam damage produced during sample preparation.
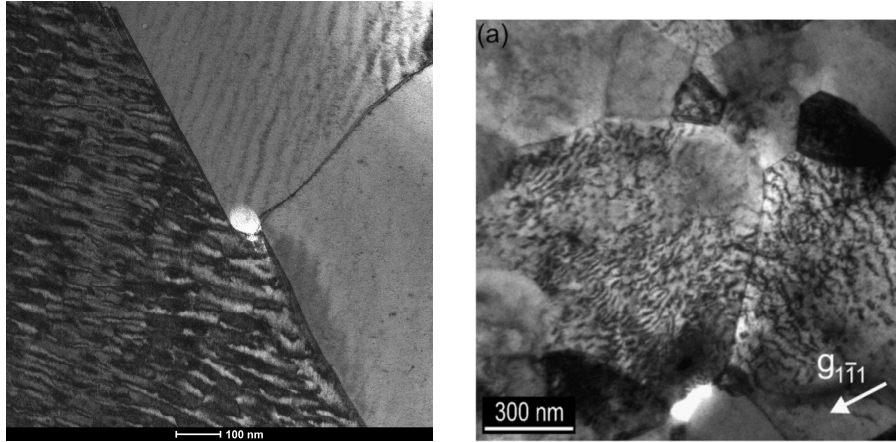
Figure 2-11 a) TEM BF image of FIB sample, b) TEM BF image of Cu exposed to a perpendicular ion beam at 30kV and 50pA[118]

Inspired on FIB milling of delicate materials [119], a very low intensity procedure that minimized radiation damage was developed, as shown in Table 2-6. Unfortunately, samples prepared by this procedure revealed the same wavy microstructure in TEM BF conditions, see Figure 2-12. In addition, internal strains within the grains resulted in distortion of the lamellas, which hindered any TEM observation. Furthermore, the number of observable grains in FIB lamellas remained limited (max. 3) and finding relevant zone axes was many times impossible in the available double tilt TEM. The aforementioned facts together with the uncertainty of the extent of beam damage made FIB an unsuitable sample preparation method. Contrarily to FIB, electrolytic polishing is a well-established method to prepare metallic TEM specimens and does not produce such defects.

Table 2-6 Low intensity FIB procedure for red gold

Down to [nm]	Voltage [kV]	Current	Angle side1/side2 [°]	Comment
4000	30	700pA	55/56	Milling
2000	30	300pA	55/56	Milling
1000	10	300pA	55/56	Thinning
800	10	100pA	55/56	Thinning
500	10	50pA	55/56	Thinning
100	5	55pA	55/56	Thinning
60	2	15pA	± 7	Shower, 2 min
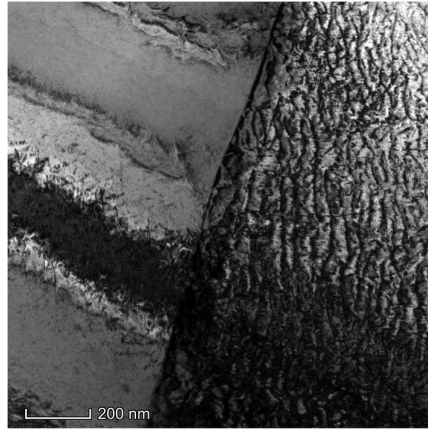
Figure 2-12 TEM BF image of sample prepared by low intensity FIB procedure

c) Electrolytic polishing

The working principle of electrolytic polishing consists in the electrochemical removal of material from both sides of the specimen until electron transparency is reached, see Figure 2-9. Electropolishing is accomplished through the formation of an anodic film of electrolyte on the specimen's surface. An electro-chemical reaction occurring in this film removes material from the specimen's surface. A proper anodic film layer is developed by adjusting the electrolyte flow. Insufficient flow results in contamination due to redeposition of material onto the specimen's surface. Excessive flow prevents the formation of the anodic film and results in etching rather than polishing. The voltage is adjusted to establish the proper polishing conditions. Figure 2-14 depicts the relation between voltage and current density and its applicability to electropolishing. Insufficient voltage results in etching, producing an uneven surface due to different etching rates of different grains or preferential etching. Excessive voltage causes electrolysis of the solution producing bubbles on the specimen's surface. These bubbles mask locally and result in pitting. In general, working at low temperatures slows down the electropolishing process. Each alloy require very specific electropolishing parameters, such as voltage, current density, temperature, time, electrolyte and electrolyte flow rate. A long and careful parametric study is required to find the optimum parameter values.
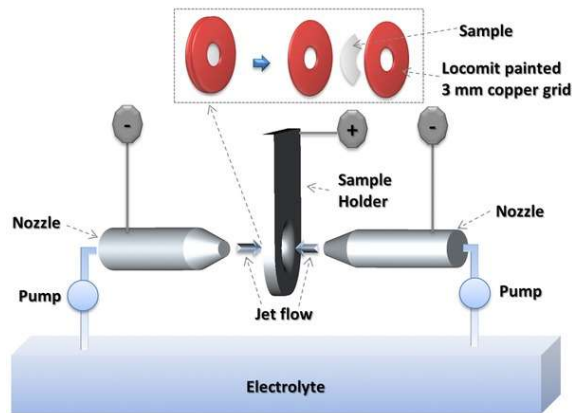
Figure 2-13 Layout of the double-jet electro-polishing set-up
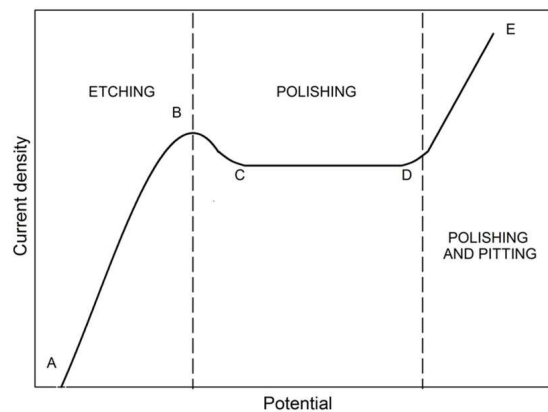
Figure 2-14 Typical electro-polishing curve, current density vs. potential. Showing the etching, polishing and pitting stages [120]

Rectangular samples with 4x2mm^2 cross section and 1mm thickness were cut out from the various wires, polished down to 100 μm thickness and punched-out into 3mm discs. Afterwards they are placed on a specific sample holder of a TENUPOL 5 instrument from STRUERS, which is equipped with a double jet electro-polishing chamber, see Figure 2-13.

The first tested electrolyte was based on chromium trioxide (35g), acetic acid (100mL) and distilled water (10mL), frequently used in literature to study equiatomic AuCu and alloys [69,77,105,121,122]. The TENUPOL 5 instrument is able to perform a preliminary voltage scan on the sample recording the current density and plots a curve similar to that in Figure 2-14. This allows to roughly estimate the starting voltage value on the parameter optimization process. For this specific electrolyte, the starting voltage value was 20.5V at 17°C. Voltage values ranging from 5 to 20V were tested at 17°C with a strong flow rate, these conditions lead to strong pitting of the specimen surface and a black oxide layer on the surface, see Figure 2-15. A trick to increase the polishing potential is to decrease the bath temperature. At a new temperature of 13°C, voltages ranging from 5V to 20 V were tested again and an etched surface was obtained at 5V and 13°C, although the oxide layer remained. The only way to

remove the oxide layer was to increase the flow of the electrolyte (increasing the temperature) but at the same time, lower temperatures were necessary to fine-tune the polishing potential. In summary, this electrolyte was discarded.
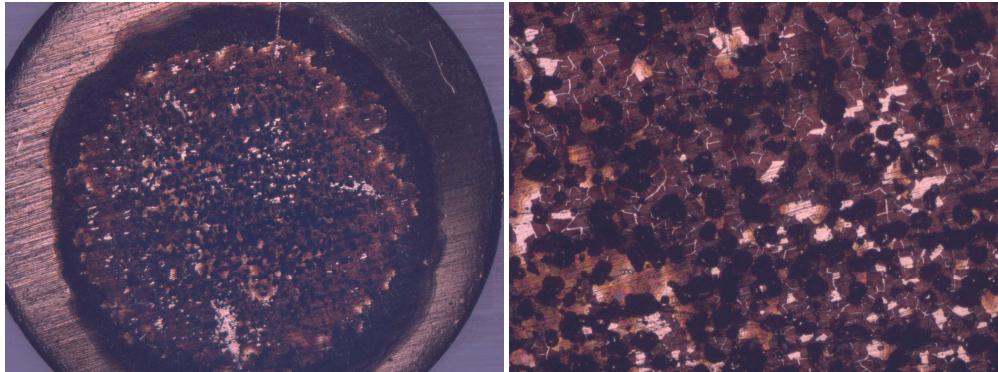
Figure 2-15 Optical micrograph of a 3mm disk electro-polished with the chromic acid electrolyte. Right: high magnification image showing pitting and the black oxide layer.

Table 2-7 Electro-polishing conditions for the chromic acid electrolyte

Temperature [^{o}C]	Voltage [V]	Observation
17	20	Pitting
17	10	Pitting
17	5	Pitting
13	20	Pitting
13	10	Less pitting
13	5	Etching

The next candidate for the electrolytic solution was composed of 5% perchloric acid and methanol like in [51]. The first trial at -20°C resulted in a very fast etching, as shown in Figure 2-16, and most of the sample was consumed by the end of the electro-polishing. However, further reduction of the temperature to slow down the reaction was not feasible technically.

500μm
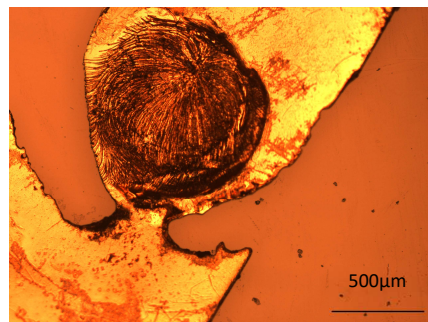
Figure 2-16 Optical micrograph of the excessive etching after electrolytic polishing with perchloric acid

32

Finally, a solution with HCl, glycerol and ethanol (2:1:1 %vol.) [17, 18] successfully polished the samples with the optimized parameters 0°C, medium flow, 24V and 140s, see Figure 2-17. Although, as a rule, a final thinning step of the TEM lamellas was performed in a PIPS II instrument with the parameters shown in Table 2-8.
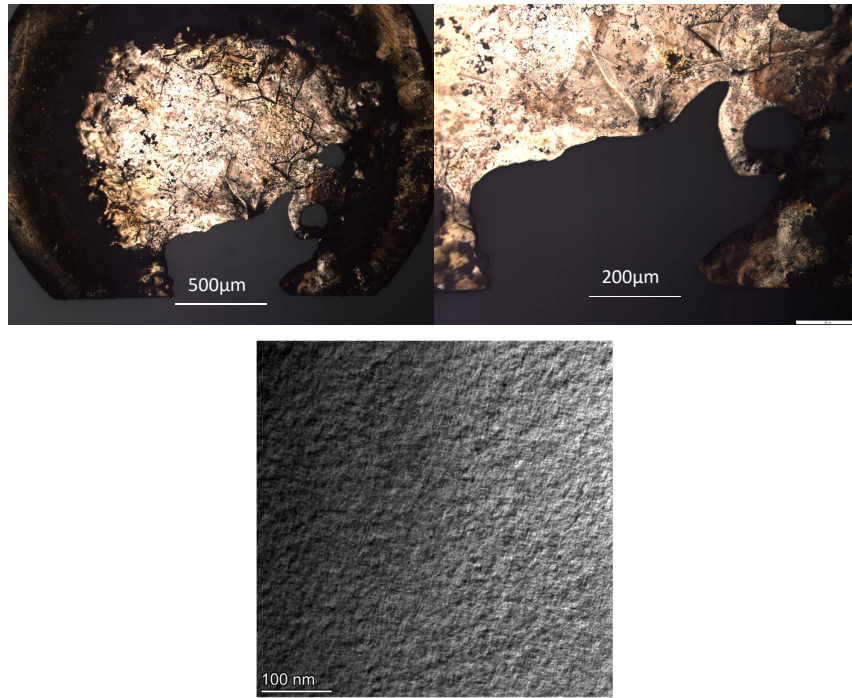
Figure 2-17 a) Optical micrograph of a 3mm diameter disk electropolished with the HCl solution. b) Higher magnification. C) TEM BF image of the same sample with very good surface contrast.

Table 2-8 PIPS II working parameters for red gold

Operation	Temperature (°C)	Modulation	Top angle (°)	Low angle (°)	Voltage (kV)	rpm	Sector (°)	Time (min)
Thinning	-100	no	8	6	2	1	60	20
Thinning	-100	no	8	6	0.8	1	60	25
Cleaning	-100	no	8	6	0.3	1	60	20

Overall, TEM sample preparation by electro-chemical polishing remains a challenge because the samples behave differently depending on their thermo-mechanical history and chemical composition.

d) Ion milling

In order to avoid complexity of specimen preparation by electrolytic polishing, a PIPS II ion milling device (model 695) from the Gatan company was used to thin down the samples to electron transparency. It was found that such a method provides specimens that are good enough for overall observation of the microstructure. However, diffraction patterns appear quite affected by irradiation damage, in the sense that they often contain additional diffraction spots due to surface damage and

are therefore more difficult to interpret than those of electrolytically polished specimens. In order to avoid the formation of wavy image contrast, as obtained in the case of FIB thinning, PIPS II ion milling with two argon ion beams was performed at -150°C, in order to reduce effects from ion beam heating and evolution of the microstructure. By using ion beam angles of +7° and -6° and applying a voltage of 5 kV for a few hours, a small perforation was created in the centre of the specimens. Final thinning and surface cleaning of the specimens was performed by applying first a voltage of 0.5 kV for 10 minutes and second a voltage of 0.2 kV for 15 minutes. A TEM image of a specimen prepared using the PIPS II ion milling device is shown in Figure 2-18.

On the other hand, the electrolytically polished TEM specimens were submitted shortly to final thinning and cleaning in the PIPS II device, in order to further reduce their thickness (to facilitate TEM observations) and to remove the surface oxide layer resulting from electrolytical polishing. Final thinning was performed at -100°C using beam angles of +6° and -6° and applying a voltage of 0.8 kV for 30 minutes. Final cleaning was also performed at -100°C using beam angles of +6° and -6°, applying a voltage of 0.3 kV for 15 minutes.
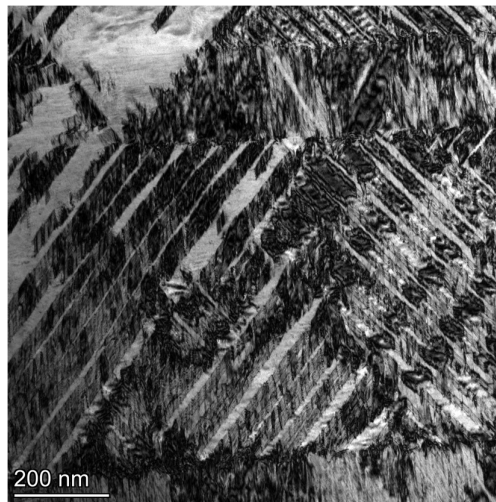
Figure 2-18 TEM BF image of a sample prepared by ion milling

TEM investigations

All TEM investigations were performed at the Interdisciplinary Center for Electron Microscopy (CIME) of the EPFL.

Main TEM investigations were performed in Thermo Fisher TALOS F200S TEM microscope operating at 200 kV and using a double tilt 'low background' specimen holder. These included TEM observations of the overall microstructure of all material types by means of BF, DF and diffraction techniques, as well as scanning transmission electron microscopy (STEM) observations complemented with energy

dispersive X-ray spectrometry (EDS) to analyse the chemical composition and observe the distribution and morphology of eventual secondary phases.

High-resolution TEM observations (HRTEM) were performed either in Thermo Fischer TECNAI OSIRIS microscope operating at 200 kV, using a standard double tilt holder, or in Thermo Fischer TITAN THEMIS microscope operating at 300 kV, also using a standard double tilt holder. All observations were performed defocus values close to the Scherzer defocus value[125], which depends on microscope properties like the spherical aberration Cs and the accelerating voltage (through the wavelength) [126], in order to optimize high resolution TEM imaging.

Analysis of TEM results

Diffraction patterns of the main zone axes have been simulated using the JEMS electron microscopy simulation software developed by P. Stadelmann [127]. High resolution TEM images have been analysed using the Gatan Digital Micrograph software; in that case Inverse Fast Fourier Transition (IFFT) images were re-constructed from original images in selecting a limited number of diffraction spots in the corresponding diffraction patterns by applying a chosen 'mask ' onto the diffraction patterns.

2.5. Powder X-ray diffraction

2.5.1. Principle

Powder X-ray diffraction is a non-destructive characterization technique used for the investigation of the atomic structure of polycrystalline materials. It is an elastic X-ray scattering method. Figure 2-19 displays the diffraction geometry where the incident beam with a momentum $k_i = \frac{2\pi}{\lambda}$ is scattered by a crystal, and results in a scattered beam with momentum $k_f = \frac{2\pi}{\lambda}$ and a diffracting angle of 2θ. The momentum change $\boldsymbol{q} = \boldsymbol{k}_i - \boldsymbol{k}_f$ is known as the scattering vector and follows Equation 2-2.
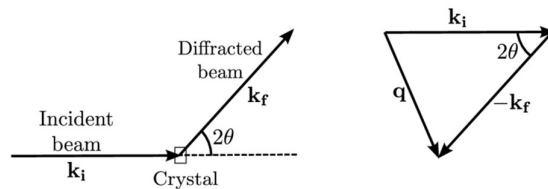
Figure 2-19 Elastic scattering geometry

Bragg's Law dictates that a beam diffracted by a set of atomic planes with interplanar spacing *d* results in constructive interference when the path difference between two waves $(2dsin(\theta))$ is equal to an integer multiple of the beam wavelength (n λ). This establishes the relationship between the atomic

inter-planar spacing (d) and the diffraction angle (θ) for a given wavelength (λ), as shown in Equation 2-3.
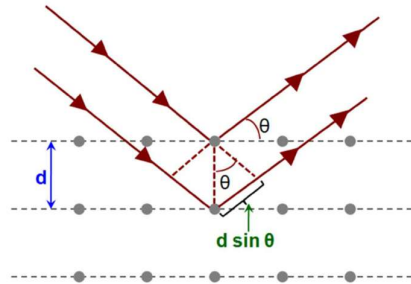
Figure 2-20 Geometry of Bragg diffraction

Equation 2-2 Definition of the scattering vector

$$q = \Delta K = \frac{4\pi \cdot sin(\theta)}{\lambda}$$

Equation 2-3 Braggs Law

$$n \cdot \lambda = 2 \cdot d \cdot \sin(\theta)$$

Synchrotrons provide high flux and high-energy X-ray beams that enable studying the bulk of the material in transmission, whereas conventional laboratory x-ray diffractometers access the first surface layers of the material. The penetrating ability of X-ray radiation in a metal depends on the photon energy, the X-ray mass attenuation coefficient, the density and the thickness. Figure 2-21 a) shows the normalized transmitted intensity vs. sample thickness for various photon energies for Au, following the Beer-Lambert equation in Equation 2-4. This reveals that energies as high as 80keV only get around 20% transmission on a sample with a thickness of 500µm.

Figure 2-21 b) shows the penetration depth as a function of the photon energy. It turns out that 80keV, just before the K-absorption edge, provides the maximum penetration depth within the available synchrotron energy range (10-150keV). The selected experimental sample thickness was 300 µm for high-energy experiments, which is a trade-off between maximum transmission and sufficient grain statistics.

Equation 2-4 Beer-Lambert equation

$$\frac{I_{out}}{I_{in}} = e^{-\mu \cdot \rho \cdot x}$$
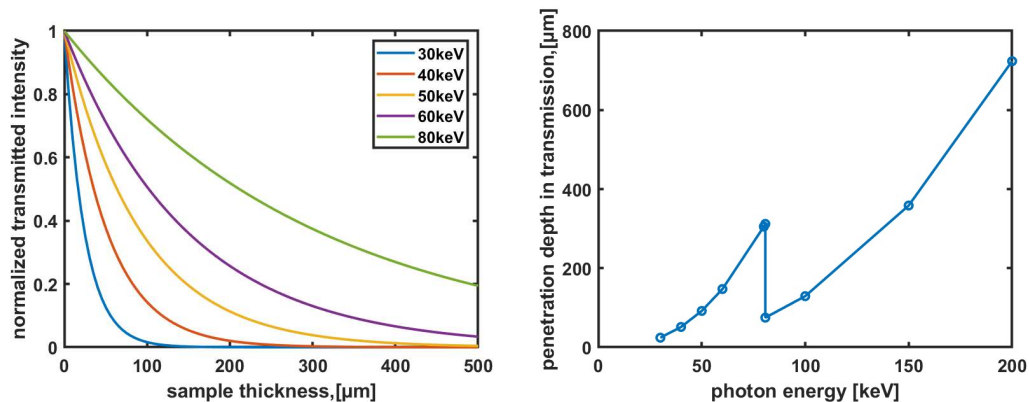
Figure 2-21 a) X-ray transmitted intensity in red gold vs. sample thickness as a function of beam energy; b) penetration depth in transmission as a function of photon energy

When working in reflection mode, for instance in a laboratory powder X-ray diffractometer, a similar analysis can be applied to estimate the penetration depth. In this case, the X-ray penetration depth will depend on the diffraction angle as shown in Figure 2-22. Laboratory diffractometers often use Cu $k\alpha_1$ radiation with characteristics energy of 8keV. Here penetration depths are limited to a few micrometres only. Mo sources exhibit somewhat higher energies (17.9keV) but do not provide larger penetration depths. This is because of the presence of the L1, L2 and L3 absorption edges of gold (between 11.92keV and 14.35keV). Even at energies as high as 80keV penetration depths remain very low in transmission. This is because at high X-ray energies the diffraction angles become very small.

In summary, working in reflection mode does not probe sufficient volume to be representative of the bulk and might not be sensitive to low volume densities of ordered domains.
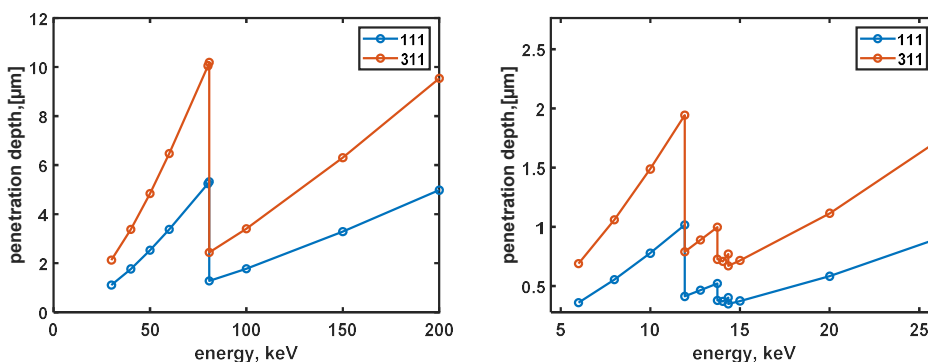
Figure 2-22 Penetration depth in reflection mode for the atomic planes a) (111) and b) (311).

2.5.2. Instrumentation

Conventional laboratory x-ray examinations with Cu-$k_{\alpha1}$ radiation were performed on a Bruker AXS D8 powder X-ray diffractometer with a Bragg-Brentano geometry, an angular range 8° - 90°, a slit size of 0.1mm and an angular resolution of 0.005. The output files of this technique are intensity profiles vs. the diffracting angle 2θ.
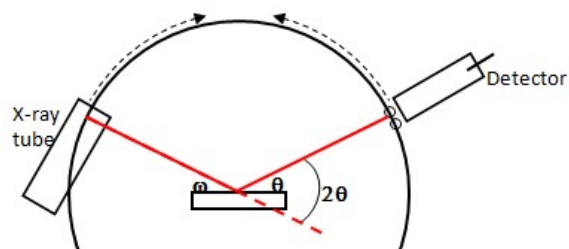
Figure 2-23 Bragg-Brentano geometry of a laboratory diffractometer

Samples examined at high-energy beam lines are probed in transmission mode. The incoming X-ray beam goes through the sample and the diffracted beam is typically recorded with a 2D detector, as shown schematically in Figure 2-24. These detectors record full diffraction rings, which provides excellent grain statistics as well as texture information.
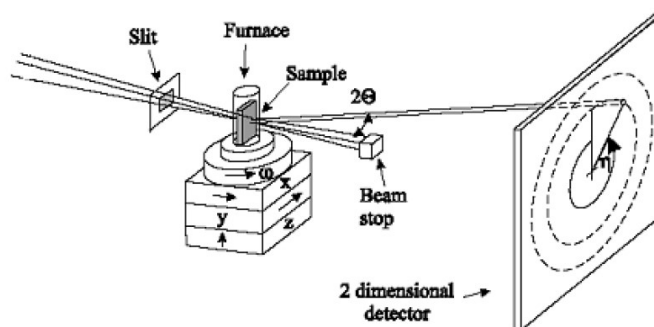
Figure 2-24 Set-up in a high-energy powder X-ray diffraction experiment from [128]

The standard procedure to access high-energy X-ray beamlines is on a proposal round basis. Twice per year, research teams may submit an experimental proposal that will be reviewed by an international expert committee. Within the framework of this research, proposals were submitted to materials science high-energy powder diffraction beamlines within Europe. Beam times were granted at the beamlines of PETRA III and ESRF while beam time at the Diamond light source was kindly granted as part of other experiments, see Table 2-9.

Table 2-9 List of synchrotron beam lines

Country	Synchrotron / beam line	Energy	Detector
United Kingdom, Oxford	Diamond / I12	60keV	Pilatus3 X CdTe 2M
Germany, Hamburg	PETRA III / P07	79keV	Perkin Elmer XRD 1621
France, Grenoble	ESRF / ID31	79keV	Pilatus3 X CdTe 2M

In each beamline, different detectors were employed according to availability. The Pilatus detectors are single-photon counting detectors with very low noise, high sensitivity and fast detection rates.

They exhibit a pixel size of size of 172 μm x 172 μm. In contrast, the Perkin Elmer XRD 1621 Flat Panel detector works with a CsI scintillator, 200 μm x 200 μm pixel size and covers an area of 2048 x 2048 pixels. The sample-to-detector distance was chosen such that at least diffraction peaks between (001) and (400) were recorded.

2.5.3. Ex situ measurements

The *ex situ* samples were prepared from the batches I to IIIs prepared by VARINOR S.A with a thickness of 350μm resulting in a transmission of 20 to 50%, depending on the X-ray beam energy. Each sample was cut out the wire with a diamond wire saw (*SMS labs* model 3500*)* equipped with 60μm diameter diamond particles. Afterwards, they were mechanically polished down to 350 μm with a *Fischione* precise planar specimen grinder model 160 making sure that every damaged layer was removed from previous grinding steps. Finally, each sample was finely polished down to 3μm with a water-based diamond solution. Spatial-dependent X-ray diffraction measurements, i.e. line scans, were performed in transmission geometry, as shown schematically in Figure 2-25. Diffraction patterns are recorded across the 2mm length of the sample with an 0.2mm X-ray beam and step size of 0.1mm.

The *ex situ* measurements were performed during beam times at Diamond (UK), PETRA III (Germany) and ESRF (France).
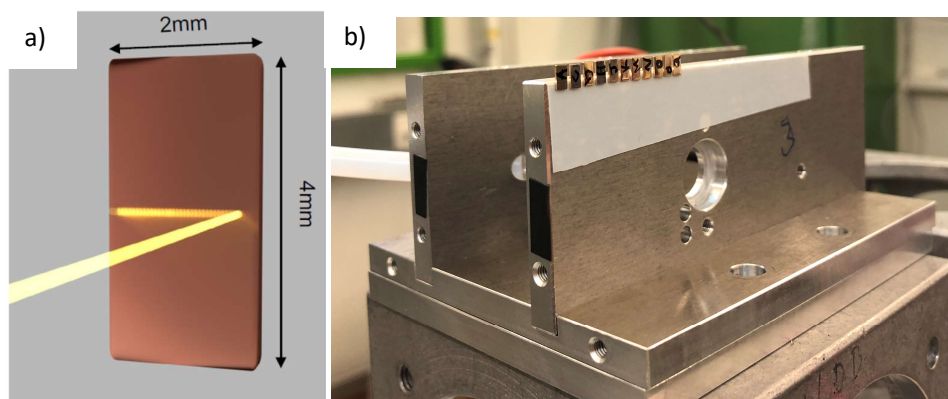
Figure 2-25 a) Schematics of the line scans along the 2mm thickness of the samples; b) picture of the experimental set-up for line scans on several samples

2.5.4. In situ measurements

The *in situ* samples were prepared with a final thickness of 350 μm resulting in a transmission of 50%. The sample preparation consisted in cutting each sample with a diamond wire saw (*SMS labs* model 3500*)* with 60μm diameter diamond particles. Then, mechanically polishing down to 350 μm with a *Fischione* precise planar specimen grinder model 160, making sure that every damaged layer was removed from previous grinding steps. Lastly, a final 3μm-polishing step with a water-based diamond solution.

For the *in situ* experiments, samples are subject to two different thermal cycles with or without an intermediate deformation step. In the first thermal cycle a recrystallization procedure is simulated, where the treatment temperature is well above T_{OD}. Here, the samples are heated for 2 min at 550°C or 660°C. This ensured a full dissolution of precipitates that have formed during the final cooling step of the wires. Subsequently, the samples are cooled down either fast (-800°C/min) or slow (-100°C/min). Some of the samples are cold-rolled to a thickness reduction of 25% using a cold rolling device for jewellery applications (supplied by *Cooks on gold* with the product reference: rolling mill 999 AXWA). The second thermal cycle simulated an ordering treatment either by isothermal artificial ageing at 250°C or by a slow heating ramp of 10°C/min. Figure 2-26 illustrates the two experimental temperature profiles, one of an *in situ* isothermal ageing experiment and another one of an *in situ* heating experiment. The first thermal cycle for both temperature profiles heated up to 660°C, however the cooling rate was slow (-100°C/min) for the isothermal ageing experiment while fast (-800°C/min) for the heating experiment.
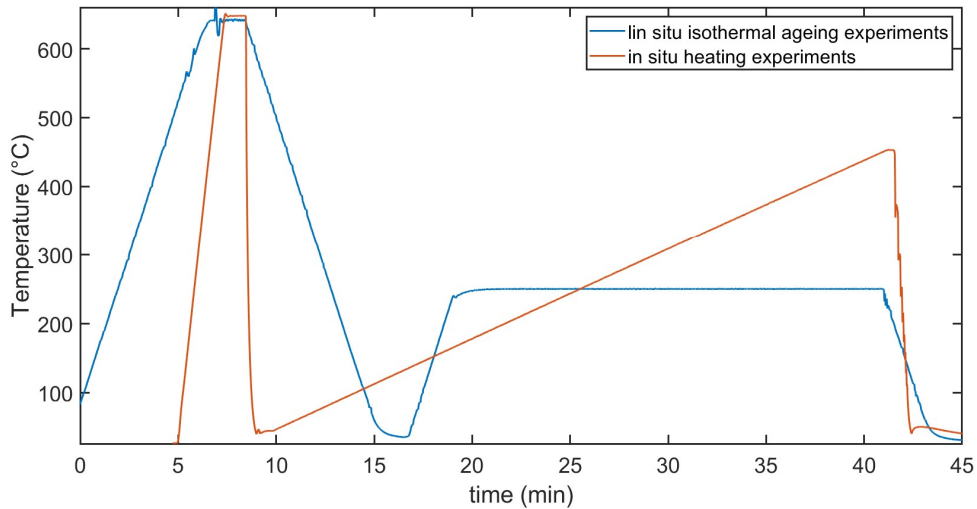
Figure 2-26 Temperature profiles of the in situ X-ray powder diffraction experiments

Dedicated furnaces available at synchrotron beamlines for *in situ* temperature experiments are mostly designed for isothermal experiments under controlled atmospheres or quench experiments with no control on the cooling rates. Typical cooling rates of these furnaces are very fast or very slow compared to the target cooling rates of this study, see Table 2-10. The target cooling rates of this study mimic industrial cooling rates that of continuous furnaces, which range from -100C/min to -1000C/min.

Table 2-10 Typical cooling rates of different types of furnaces

Furnace	Typical cooling rates [°C/min]
Closed chamber under Ar atmosphere	-1
Open chamber under air	-40
Open chamber and fast quench	-20 000

Therefore, a miniaturized portable furnace was developed with the thermal characteristics shown in Figure 2-28b. This heating system includes a sample holder, two ceramic heaters, a current generator, a thermocouple, an electromechanical valve, two gas jets, an external aluminium box and a computer.

Finite element modelling with ABAQUS [129] was employed to design the sample holder's geometry ensuring 1) a minimal weight to reduce the required heating power and 2) maximum surface to increase the cooling ability. Copper was the selected material of the samples holder due to its low heat capacity, high thermal conductivity and high melting point. The design allowed reaching a homogeneous temperature distribution on the sample in stationary and transient conditions, a maximum target temperature of 800°C and cooling rates as fast as -800C/min by forced cooling while maintaining mechanical stability. Figure 2-27 shows the drawings of the copper sample holder.
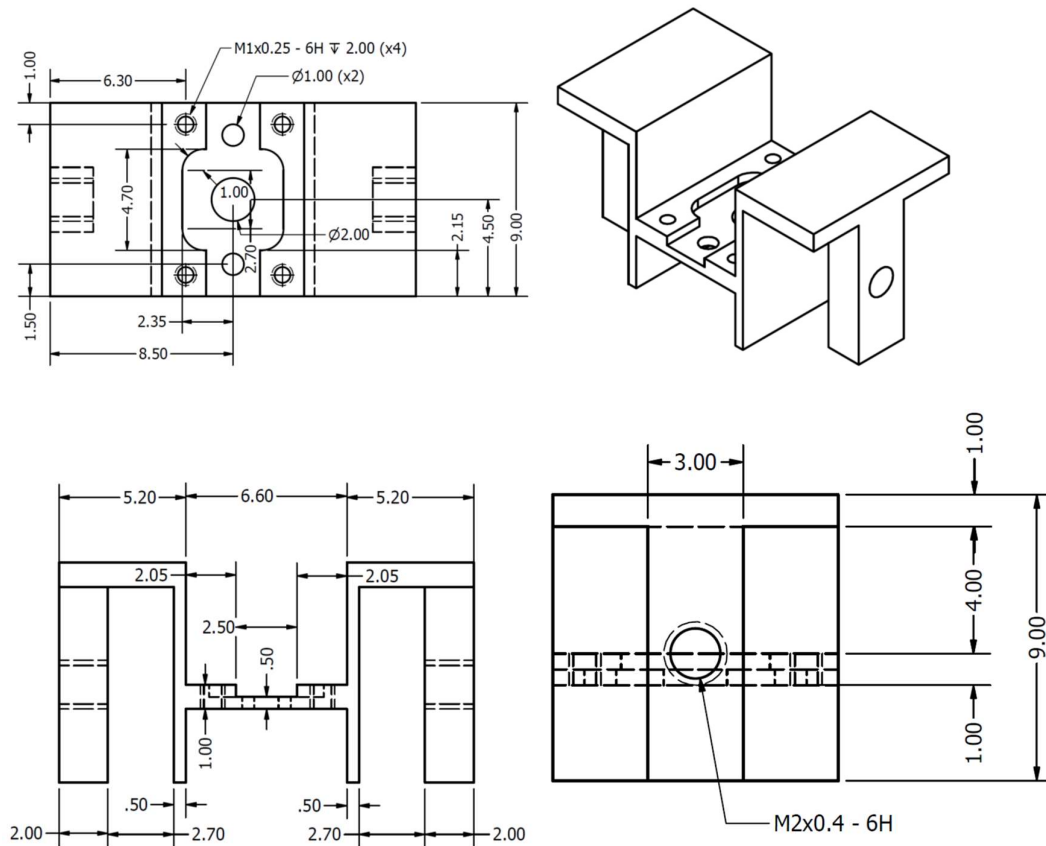
Figure 2-27 Technical drawings of the copper sample holder

The sample and a fine gauge K-type thermocouple (OMEGA GmbH) were clamped in the holder, which included an aperture to allow the passage of the incoming X-ray beam through it. The aperture diameter was big enough to prevent copper diffusion into the probed volume during the *in situ* experiments.
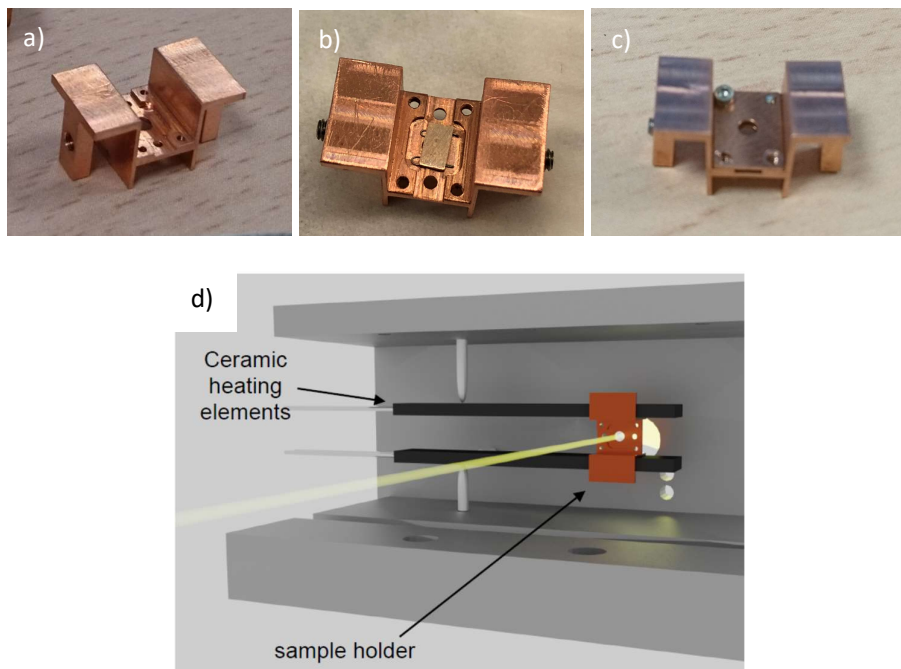
Figure 2-28 a) Copper sample holder without sample; b) copper sample holder with sample; c) copper sample holder with sample and cover; d) set-up for in situ synchrotron experiments.

The fine gauge thermocouples consisted of a 125 µm diameter head and 500mm length. A data acquisition device NI 9211 was employed for the temperature read out.

The heating elements were two silicon nitride resistor ceramics (Glow igniters, Bach resistors AG) with high power density, fast precise heating and outstanding durability. The dimensions of the heaters are 60.0 x 8.0 x 2.5 mm with a heated area of 10.0 x 8.0 x 2.5 mm and a maximum working temperature of 1000°C. They were in permanent mechanical contact with the sample holders, as shown in Figure 2-28. The temperature of the heaters was raised by a 10-Ampere generator, which worked in a current-control mode with a limit working voltage of 24V. The Electronics department at PSI kindly lent the current generator.

Heat sinks were avoided by stabilizing the ceramic heaters with sharp-tipped screws in such a way that the copper sample holder was kept at the height of the entrance and exit apertures for the x-ray beam of the outer aluminium chamber. Two argon jets (not shown in figure) on each side of the copper parts forced fast cooling. The pressure of the argon jet varied between 5-10 bars depending on the beamline.

An in-house written LabView program remotely controlled the furnace. The input parameters for each temperature cycle were the heating rate, the target temperature, the hold time at the target temperature and the cooling rate. The temperature readout from the thermocouple served as the input for a PID loop that steered the thermal cycle. During the cooling stage, an electro-mechanical valve (RS-VDW20GA) would open/close the argon jets following the specified cooling rate. The LABVIEW program was synchronized via TCP/IP to the beamlines, in order to save the temperature value in the corresponding XRD file during the *in situ* experiment.

Set-up for in situ artificial ageing experiments performed at the P07 beam line at Petra III

In situ isothermal ageing X-ray diffraction experiments are performed at the High Energy Materials Science Beamline (P07) at Petra III [130]. A schematic view of the setup is shown in Figure 2-29. The X-ray beam had an energy of 77.7keV and a size of 0.2×0.2mm2. Diffracted X-rays are recorded with a Perkin Elmer XRD 1621 Flat Panel detector, which is positioned at a distance of 1.4m. Exposure times were 0.1s and 1s for the in situ and ex situ measurements, respectively. Calibration of the setup was performed using a standard CeO_2 powder yielding precise information on the position of the beam centre, the sample-to-detector distance and the detector tilt.
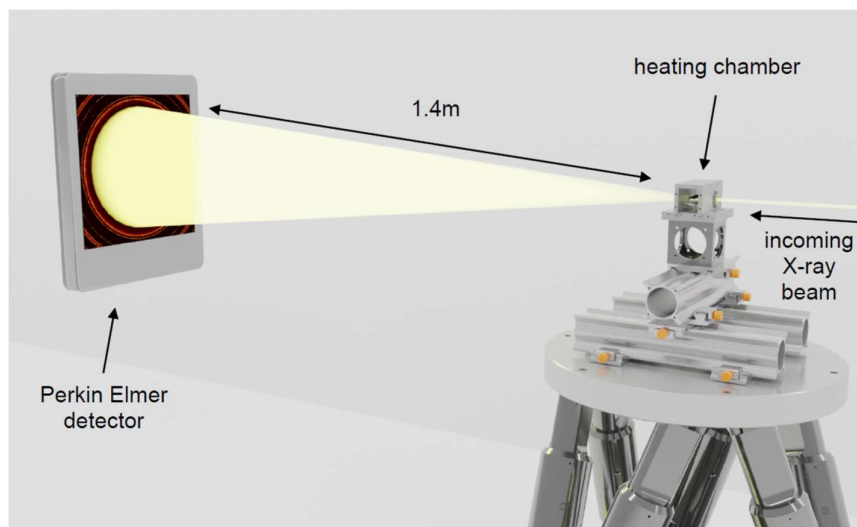
Figure 2-29 Experimental set-up for in situ experiments at P07 in Petra III

Set-up of the in situ heating experiments performed at the ID31 beam line at ESRF

In situ heating X-ray powder diffraction experiments were performed at the High Energy Materials Science Beamline (ID31) at ESRF. The X-ray beam had an energy of 79keV, which is just below the K-absorption edge for gold. This results in a transmission of 30% for the samples considered in this study. The focused X-ray beam is slit down to a size of 0.2 x 0.2 mm². The diffracted X-ray beam is recorded with a Dectris Pilatus3 X CdTe 2M detector, with 1475 x 1679 pixels and a pixel size of 0.172 mm. The detector was positioned at a distance of 910 mm from the samples. The set-up was calibrated using a

standard CeO$_2$ powder yielding precise information on the beam centre, sample to detector distance and detector tilt. The samples are mounted in a custom-built heating chamber.

2.5.5. Analysis of X-ray diffraction results

Data reduction

Figure 2-30 shows a typical 2D diffraction pattern, which is obtained after applying the corresponding detector flat-field correction and masking of the detector channels. Powder diffraction patterns show radially symmetrical 2D patterns and can be reduced to 1D patterns by radial integration, resulting in an intensity profile vs. the diffracting angle (2θ) or the scattering vector (q).

In order to process a 2D pattern it is necessary to input the beam wavelength, the beam centre and the detector orientation. For that, the standard NIST SRM64b CeO$_2$ is used as a calibrant before every experiment. Different software packages were used for data reduction The patterns obtained at I12 (Diamond) and P07 (PETRA III) beamlines were processed with the Data Analysis WorkbeNch software (DAWN)[131]. At ID31 (ESRF), in-house built MATLAB scripts from the beam line were used. In what follows the 1D intensity profiles will be presented as a function of the scattering vector (q), defined as in Equation 2-5, because the latter is only dependent on the inter-planar spacing (d) and not the X-ray wavelength (λ); this facilitates comparison of X-ray patterns of different beam lines.

Equation 2-5 Equation of the scattering vector q

$$q_{hkl} = \frac{4\pi \sin \theta}{\lambda}$$
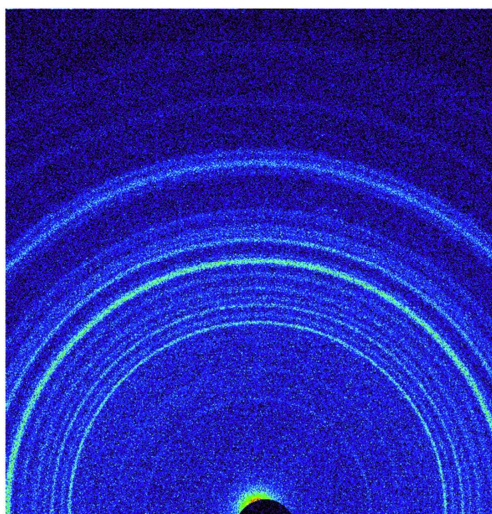
Figure 2-30 2D Diffraction pattern

In some cases, secondary diffraction has been observed. This results in spikes on top of the regular diffraction patterns see blue line in Figure 2-31. These spikes were filtered out from the 2D images via an algorithm that identifies abrupt intensity changes between a pixel and its first-neighbours. The red

line in Figure 2-31 shows that this procedure was very successful in removing the spike, without disrupting the original spectrum.
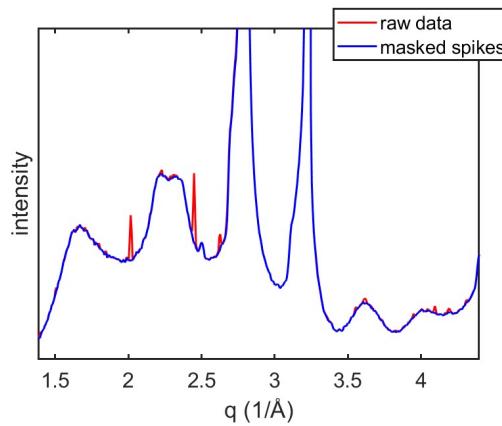
Figure 2-31 Powder diffraction peaks before and after masking of the secondary diffraction spikes.

Data Fitting Method

The lattice parameters of the disordered FCC matrix and the ordered AuCu-I phase are very similar, resulting in a strong overlap of fundamental peaks, in particular during the early stages of ordering. These cannot be separated easily. Therefore we concentrate for the fitting on the freestanding (001), (201) and (112) superlattice reflections. The evolution of some of the fundamental peaks will be reported by showing the raw data.

The diffraction peaks were fitted using in-house developed single peak-fitting MATLAB routines, yielding precise information on the integrated intensity, peak position and full-width at half-maximum (FWHM). It is not possible to apply full-pattern fitting routines to follow the ordering transformation, as it will be discussed in Chapter 6. An adaptive fitting routine was developed in order to account for thermal expansion during the experiments.

The fitting model is based on an asymmetric Pearson VII function Equation 2-6 because it fits well peak shapes of X-ray powder diffraction patterns. This function is becomes Lorentzian as $m \rightarrow 1$ and Gaussian as $m \rightarrow \infty$. Therefore, the m parameter can handle various tail-shapes. The w parameter represents the FWHM. The asymmetric Pearson VII handles asymmetric tails (m_l and m_r) and the peak skewness (α). Fitting is performed via the linear least squares method.

Equation 2-6 Asymmetric Pearson VII function

$$I(q) = I_{max} \frac{w^{2m_l}}{\left[w^2 + (1 + 10^\alpha)^2 \left(2^{\frac{1}{m_l}} - 1\right)(q - q_0)^2\right]^m_{q<q_0}} + I_{max} \frac{w^{2m_r}}{\left[w^2 + (1 + 10^\alpha)^2 \left(2^{\frac{1}{m_r}} - 1\right)(q - q_0)^2\right]^m_{q>q_0}}$$

The integrated intensity, the peak position and the FWHM can be easily calculated from the fitted curve of a diffraction peak. The integrated intensity of the diffracted peaks is linked to the volume fraction of a particular phase. From the peak position, the elastic lattice strain of a given grain family can be calculated as in Equation 2-7.

Equation 2-7 Lattice strain formula

$$\varepsilon_{hk} = \frac{q_{hkl} - q_{hk}^0}{q_{hkl}^0}$$

With q_{hkl} the hkl-dependent scattering vector, θ the diffraction angle and λ the X-ray wavelength. The stress-free scattering vectors q^0_{hkl} for the ordered phase are obtained from a sample heat-treated at 330°C for 12h.

The (110) super-lattice peak exhibited the characteristic early stages peak splitting with two diffuse maxima during most of the experiments, therefore single peak fitting routines were not applied and the integrated intensity was calculated as the integral below the peak curve.

Different sources of diffuse scattering such as short-range order and/or thermal diffuse scattering[132] result in a strong non-linear background. Therefore, a spline function is fitted on every pattern to account for the background, as shown in Figure 2-32.

However, the position of the diffraction peaks slightly varies for different shapes of the spline, in particular at the early stages of ordering, where the superlattice reflections have low intensity. Lattice strain variations up to 0.2% for the undeformed and 0.8% for the deformed samples have been found when using different splines. Regardless the background subtraction strategy, the observed tendencies in peak position, integrated intensity and FWHM are however the same.
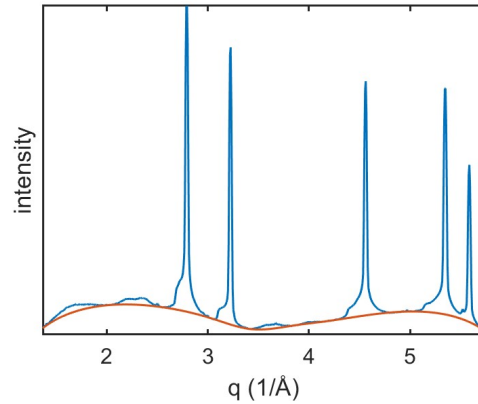
Figure 2-32 Powder x-ray diffraction pattern with an overlay of the fitted non-linear background

The FWHM is defined as the width of the diffraction peak, in inverse Å, at a height halfway between the background baseline and the peak maximum. Contributions such as crystallite size, micro-strain, dislocations, faults and antiphase boundaries contribute to the peak broadening. However, only the peak broadening induced by crystallite size and micro-strain will be considered in this study. It is considered that the samples subject to FWHM evaluations do not show contributions from dislocations, antiphase boundaries nor faults.

The peak width due to crystallite size varies inversely with crystallite size, i.e. as the crystallite gets smaller, the peak gets broader. The Scherrer equation is a formula that relates the crystallite size with the X-ray peak broadening, named after Paul Scherrer[133]. Equation 2-8 defines the peak broadening,β_c as a function of the crystallite size τ. The coefficient 5.56 results from assuming spherical crystallites in a cubic matrix. Peak broadening due to crystallite size is independent of the scattering vector.

Equation 2-8 Peak broadening β_c due to crystallite size

$$\beta_c = \Delta q = \frac{5.56}{\tau}$$

The contribution of the displacements of the unit cells about their normal positions is known as microstrain. Figure 2-33a shows a set of unit cells under a strain gradient, in this case bending. The distribution of d-spacings of such unit cells results in the broadening of the observed diffraction peak, as shown in Figure 2-33b. The peak broadening due to microstrain,β_{ms} increases with increasing scattering vector, as shown in Equation 2-9.
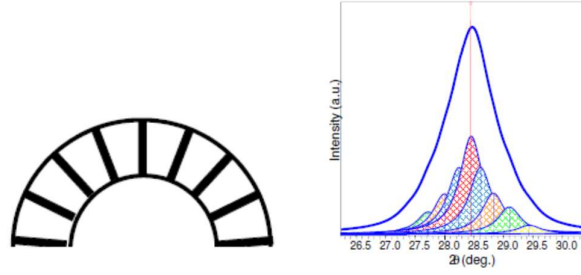
Figure 2-33 a) Unit cells under a strain gradient; b) contribution of the distribution of d-spacings of each unit cell to the observed diffracted peak from [134].

Equation 2-9 Peak broadening β_{ms} due to microstrain

$$\beta_{ms} = \Delta q = q \cdot \varepsilon$$

The Williamson hall plots the FWHM vs. the scattering vector as in Equation 2-10. The contributions of micro-strain and crystallite size results in a straight line with a positive slope equal to the microstrain where the intercept at y = 0 is inversely proportional to the crystallite size τ.

Equation 2-10 Formula of FWHM with microstrain and crystallite size contributions

$$\beta = \Delta q = q \cdot \varepsilon + \frac{5.56}{\tau}$$

Calculation of the long-range order parameter S

The long range order parameter, S, can be calculated based on the integrated intensity of the diffracted peaks from the ordered phase and is defined following [135]:

Equation 2-11 Definition long-range order parameter, S, from the intensity in the diffraction peaks

$$S^2 = \frac{A_s \, [mLP]_f \left| f_{Au}e^{-M(Au)} + f_{Cu}e^{-M(Cu)} \right|_f^2}{A_f \, [mLP]_s \left| f_{Au}e^{-M(Au)} - f_{Cu}e^{-M(Cu)} \right|_s^2}$$

With A_s and A_f to the integrated intensity of a fundamental and a superlattice peak, m the multiplicity factors, LP the Lorentz Polarization factor and f_{Au} and f_{Cu} the atomic scattering factors. The exponential functions represent the temperature factor with the M parameter as the Debye-Weller factor, which contribution can be neglected for the temperature and q-range considered in this work.

Chapter 3   Microstructural   characterization   of thermo-mechanically processed wires

This chapter characterizes the microstructural evolution of red gold during the manufacturing route of U-shaped samples. The thermo-mechanical operations in the manufacturing route are 1) recrystallization heat treatment in a continuous furnace, 2) re-straightening operation, 3) bending operation and 4) furnace brazing treatment in a continuous cooling furnace.

Two recrystallization temperatures (550^oC and 660^oC) were selected to study the evolution of the microstructure during processing as well as the shape distortion after the furnace brazing operation. In order to elucidate whether the shape distortion happened during the heating or cooling stage of the brazing operation, two additional samples were annealed between the bending operation and the furnace brazing operation, i.e. 660RSBA and 550RSBA. Table 4-1 summarizes the investigated samples in this chapter, which is organized as follows:

Section 1 presents typical hardness values in red gold at different microstructural stages. Section 2 presents the hardness evolution during the manufacturing of U-shaped samples performed at two different recrystallization temperatures. Section 3 presents the shape distortion of the U-shaped samples as a function of thermo-mechanical history. Section 4 presents the characterization of the microstructure at each processing stage. Section 5 summarizes the results

Table 3-1 Summary of the investigated samples in this chapter

Manufacturing route	Sample	Hardness	OM	EBSD	TEM
A	660R-s	•	•		•
	660RS-s	•	•		
	660RSB-s	•	•		•
	660RSBF-s	•	•		
	660RSBA-s				
B	550R-s	•	•	•	
	550RS-s	•	•		
	550RSB-s	•	•	•	
	550RSBF-s	•	•	•	
	550RSBA-s				
C	550RF-s	•	•	•	

3.1. Typical hardness values of red gold

Typical macro-hardness values at different microstructural states, i.e. water-quenched, continuously cooled or heavily deformed, are presented in Table 4-2. Note that the hardness after continuous furnaces is generally greater compared to the water-quenched alloys.

Table 3-2 Hardness values of red gold at different manufacturing conditions

State	HV30
Water quenched from 750°C	170
Water quenched from 660°C	160
Continuous furnace cooling from 660°C	180
75% reduction cold rolled	260

Figure 3-1 displays the macro-hardness evolution at 25°C as a function of time (weeks) for red gold samples treated at 660°C and 750°C in a water-quench furnace and at 660°C in a continuous furnace, respectively. The credits of this dataset belong to VARINOR S.A., who kindly allows the reproduction of the data. The macro-hardness measurements (HV30) were performed with an industrial durometer KB 250 BVRZ. The plotted values correspond to the average of 6-10 measurements with a standard deviation between 2-5%. The water-quenched samples exhibit a marked hardness increase with time, whereas the continuously cooled sample shows smaller hardness variations. The sample quenched from a greater temperature (750°C) is expected to have the largest density of quenched-in excess vacancies. This explains the pronounced hardening up to week 9 compared to the water-quenched sample from a lower temperature (660°C).
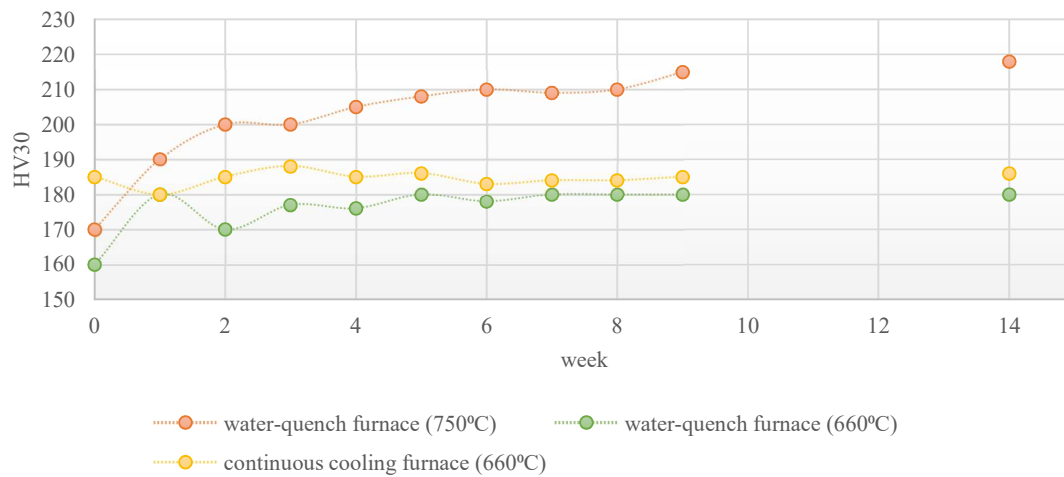
Figure 3-1 Evolution of the micro-hardness as a function of time (weeks) as a function of previous cooling rate.

3.2. Hardness evolution during the manufacturing of U-shaped samples

Figure 3-2 shows the micro-hardness profiles across the thickness of thin wires (2mm thick) after various processing operations: recrystallization, straightening and bending. Each value is the average of 5 measurements and the error lies within the dotted markers of the graph. The recrystallized samples 550R-s and 660R-s show similar and homogeneous hardness along the thickness. The straightening operation induces V-shaped profiles because of increased hardening of the near-to-surface regions. The 660RS-s and 550RS-s samples show a similar behavior. The bending operation increases further the hardness in the near-to-surface regions. No major hardness differences are observed as a function of the previous recrystallization treatment.
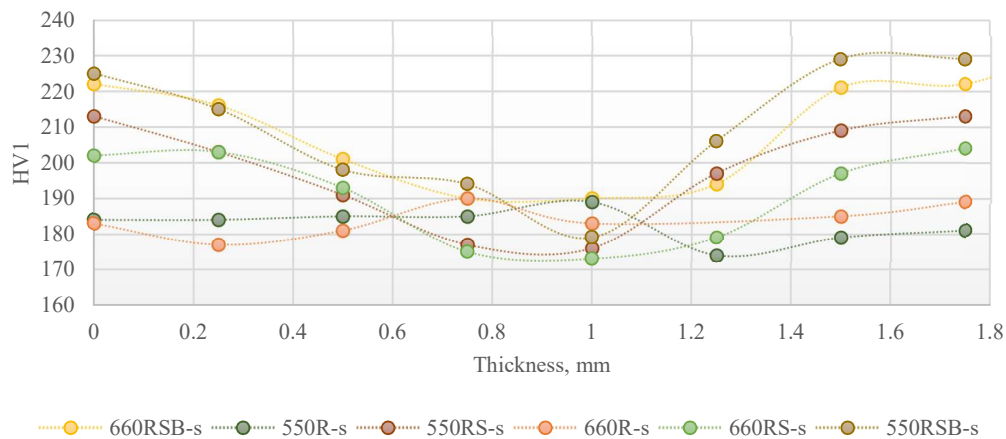
Figure 3-2 Hardness profile along the thickness of the wires from samples 550R-s, 550RS-s, 550RSB-s, 660R-s, 660RS-s, 660RSB-s

Figure 3-3 shows the micro-hardness profiles along the thickness of bent wires that were subject to a furnace brazing treatment (550RF, 550RSBF, 660RSBF) or an annealing treatment (550RSBA, 660RSBA). The hardness values show a large scatter within one sample; which is explained by the excessively big grain size of this samples (>100μm), and therefore each hardness measurement was performed on a different grain. Greater hardness values are related to chemical ordering that occurred during the cooling from 860°C. Later on, it will be shown that the microstructure at this point shows a quite advanced degree of chemical order.
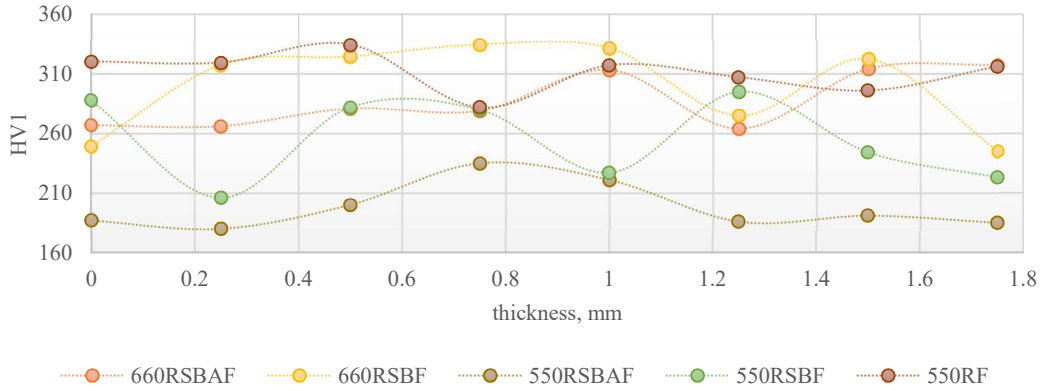
Figure 3-3 Hardness profile along the thickness of the samples for the states: 550RSBF, 550RF, 550RSBAF, 660RSBF, 660RSBAF

3.3. Shape distortion of U-shaped samples

Right after the bending operation, the U-shaped samples show spring-back. Figure 3-4 shows the spring-back effect of U-shaped samples as a function of the recrystallization heat treatment parameters, i.e. recrystallization temperature and cooling rate. Fast cooling rates induce the well-known spring back behaviour, meaning that the U-shape opens up after bending. On the other hand, slow cooling rates induce a *spring-forward* effect, meaning that the U-shape closes up after bending.
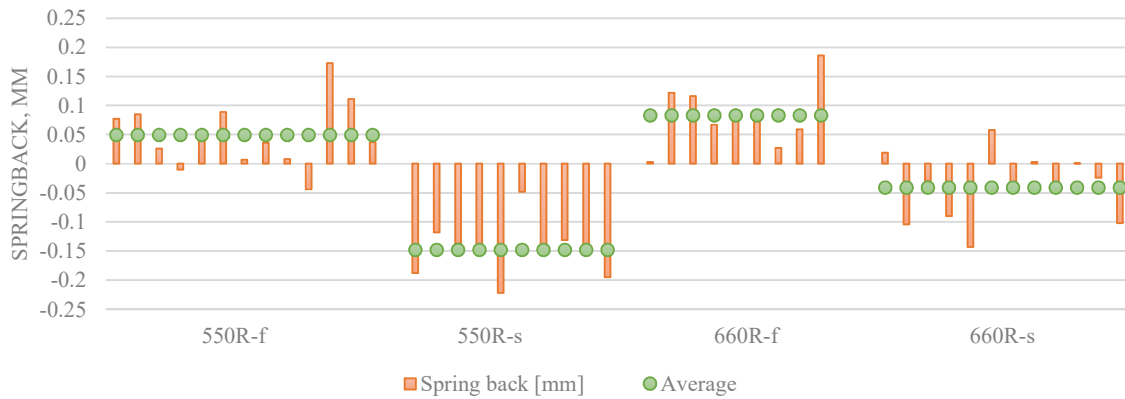
Figure 3-4 Springback on U-shaped samples after the bending operation

After the furnace brazing operation, the U-shaped samples generally open-up. Figure 3-5 shows an overlay of the spring-back effect, the shape distortion after brazing and the total shape distortion (spring-back +distortion after brazing) obtained for all the processing routes. The number of samples used for this study was limited to 10, which is far from a statistical study but already shows some tendencies in the data.

- For a fixed recrystallization temperature, faster cooling rates result in a greater distortion (comparing 550RSBF-s and 550RSBF-f)

- Higher temperatures suggest greater distortion (compare 550RSBF-s vs 660RSBF-s).
- The shape distortion after the furnace brazing operation is equivalent to the one obtained after an annealing treatment applied right after the bending operation (e.g. compare 660RSBF-s and 660RSBA-s). This suggests that the shape distortion is not related to the temperature of the thermal treatment (860°C and 550°C/660°C, respectively). This suggests that the shape distortion happens during the heating ramp of the thermal treatment applied after the bending operation.
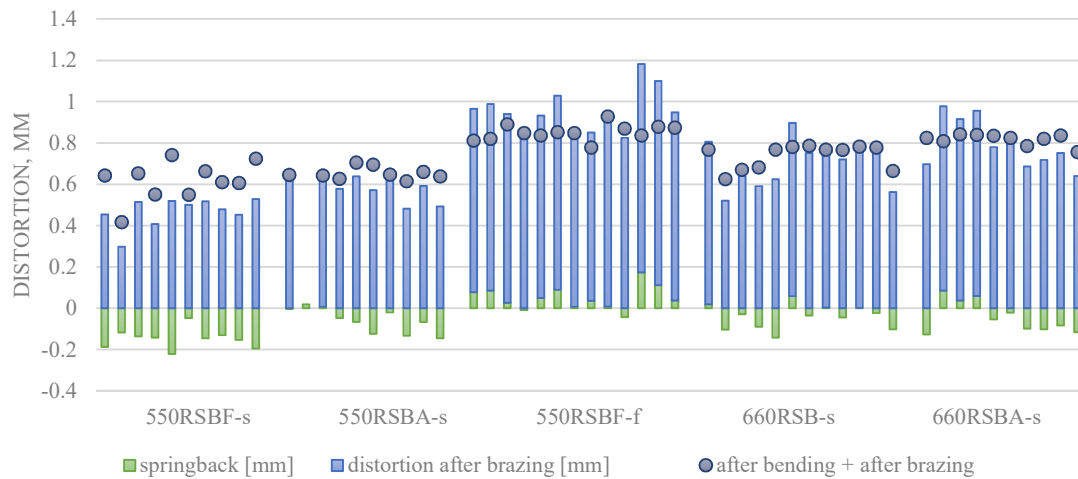
Figure 3-5 Distortion of various U-shaped samples differently processed. Green bars: spring-back after bending. Blue bars: distortion after brazing. Blue dots: total distortion calculated as the sum of the spring-back effect and the distortion after brazing.

3.4. Microstructural characterization at each processing step

3.4.1. Recrystallized state

Optical examination of the transverse and longitudinal cross-sections of the wires reveal a fully recrystallized microstructure composed of equiaxed grains and a homogeneous grain size distribution. Under a thermal treatment at a fixed temperature, a duration of 6 minutes and a slow cooling rate, the sample 660R-s shows an average grain size of 30μm, while the sample 550R-s shows an average grain size of 8μm (Figure 3-6).

Micro-hardness measurements on the cross-section of the wires reveal a homogeneous hardness distribution, with an average value of 183±4 HV1 for both samples. EBSD examinations performed on the cross-section of sample 550R-s reveal a very mild texture, as shown in inverse pole figure map in Figure 3-7 left. Phase identification using EBSD shows a FCC solid solution phase.
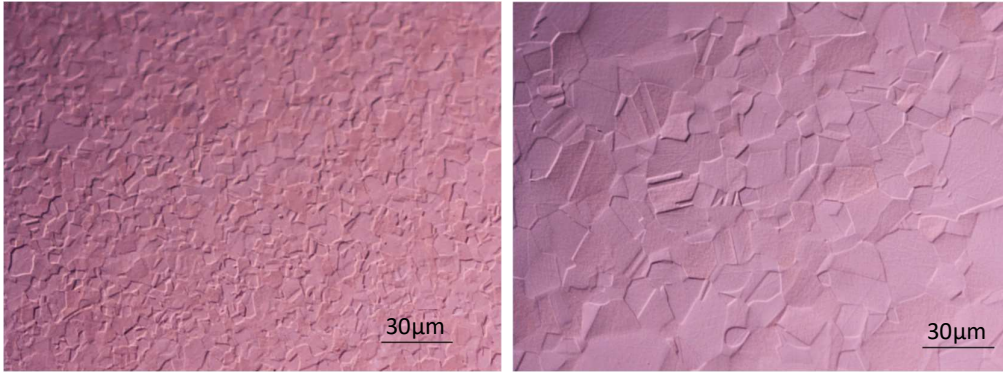
Figure 3-6 Optical micrographs of the wire's transversal cross-section a) Sample 550R-s, b) Sample 660R-s.
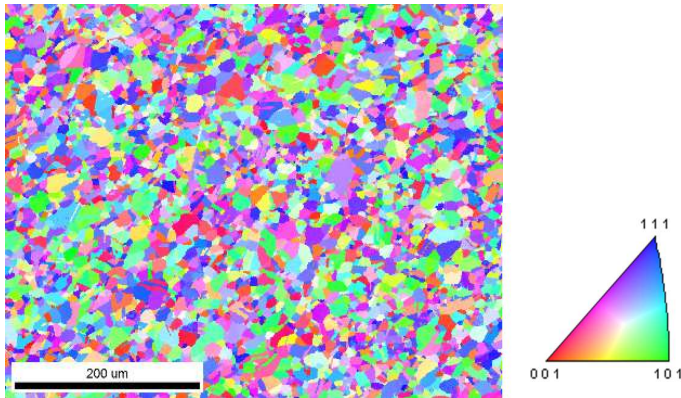
Figure 3-7 EBSD inverse pole figure map at the center of sample 550R-s

To understand the structural details of the specimen, TEM and HRTEM analysis were carried out. Ordering after a recrystallization heat treatment is characterized by a marked mottled surface in bright field images, as indicated by the white arrows Figure 3-8a-b. The selected area electron diffraction (SAED) in Figure 3-9 belongs to the region A in Figure 3-8a and reveals weak and diffuse super-lattice spots together with a characteristic streaking of the disordered fundamental (111) and (002) reflections; as indicated by white open circles and arrows, respectively. The combination of the latter features indicates the presence of coherency strains between chemically nano-sized ordered regions and the disordered matrix [51].
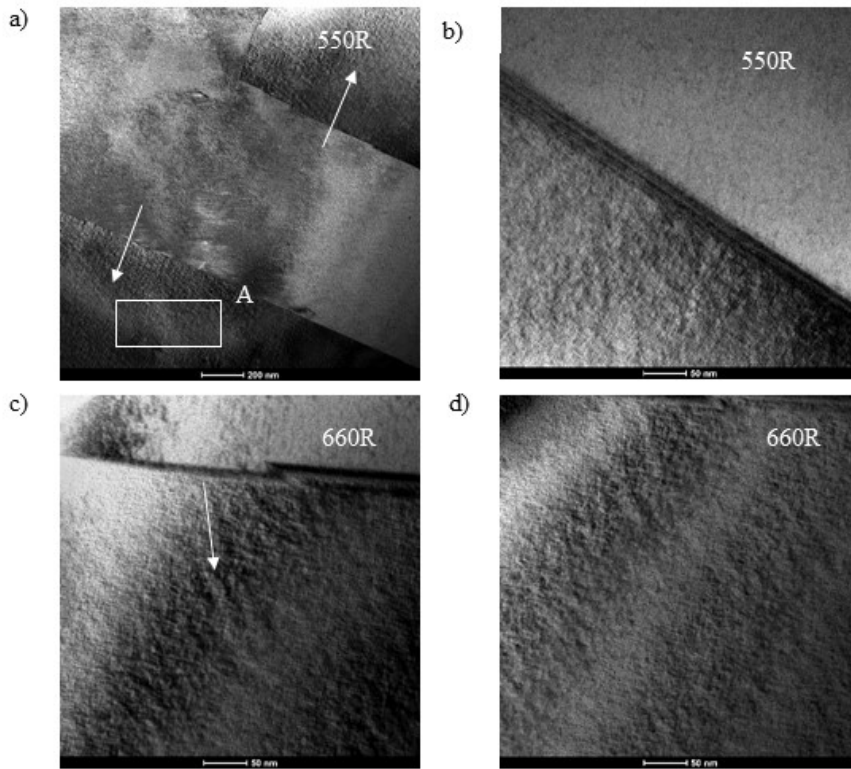
Figure 3-8 TEM BF images revealing the characteristic mottled contrast due to coherency strains
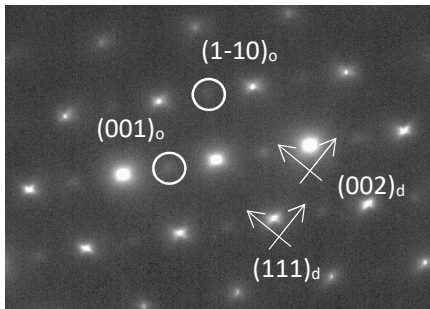
Figure 3-9 TEM SAED pattern from region A in Figure 3-8a, corresponding to the [110] zone axis. Open circles indicate diffuse superlattice reflections due to chemical ordering, while the white arrows highlight the streaking of the fundamental spots.

Dark field images in Figure 3-10a-b belong to sample 550R-s and reveal the presence of chemically ordered domains that appear as white dots. The zone axis under observation corresponds to the [110], which is sensitive to $L1_0$ orientational variants with their c-axis in plane with the specimen's surface. The ordered domains are finely dispersed within the disordered grains in a very homogeneous manner. It is noted that opposite to the diffraction pattern in Figure 3-9, the SAED in Figure 3-10c does not clearly show <110> streaking of the fundamental (200) and (220). This is due to the overexposure during acquisition of the SAED image.

a)

b)

c)

(001)o

(110)o
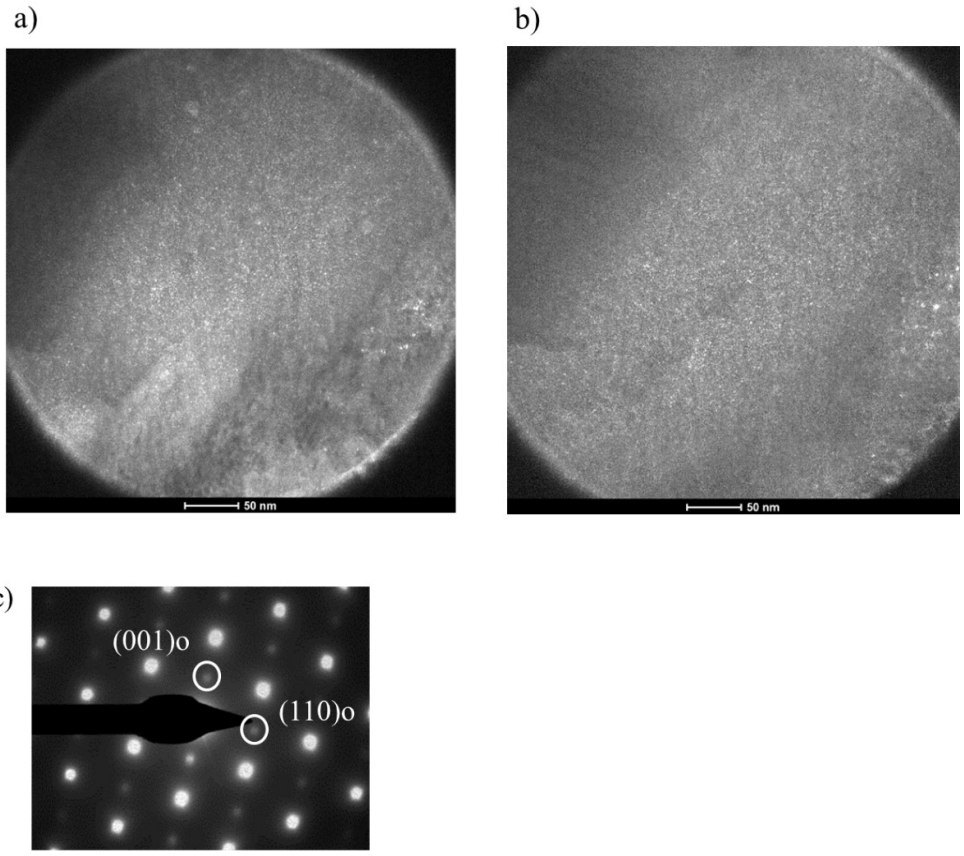
Figure 3-10 TEM DF images using a) the (001) and b) the (1-10) superlattice reflections along the [110] zone axis on sample 550R-s.

The observable grains in the 660R-s sample were badly oriented with respect to the [110] zone axis. The only accessible zone axis was the low symmetry [201] zone axis, however, succesful DF imaging could be performed using the (1-10) superlattice spot, see Figure 3-11b. The DF image in Figure 3-11a reveals a homogeneous and fine distribution of chemically ordered domains. Please note that images taken along different zone axes are not comparable in terms of distribution nor size of the precipitates.
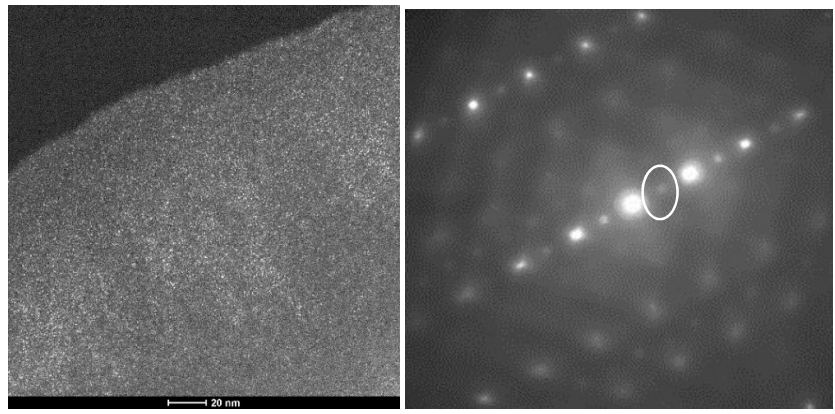
Figure 3-11 TEM DF image along the (1-10) super-lattice reflection, indicated by a white arrow in the SAED, along the [210] zone axis.

A second tentative to observe the 660R-s sample under the same conditions as for the 550R sample, for comparison purposes, only provided a SAED along the [001] zone axis. The general cubic symmetry of the microstructure confirmed the presence of the three orientational $L1_0$ variants along the [001] zone axis, as shown in Figure 3-12. Unfortunately, the specimen thickness was too thick to allow good contrast DF images on the superlattice reflections.
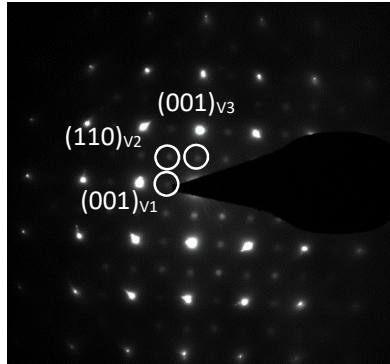
Figure 3-12 SAED pattern along the [001] zone axis revealing diffuse scattering on the (100), (010) and (110) super-lattice spots, confirming the presence of the three L10 orientational variants.

These observations confirm that slow cooling rates in continuous cooling furnaces result in a very similar microstructure regardless the treatment temperature. This microstructure is characterized by weak and broad super-lattice spots and sometimes streaking of fundamental reflections. DF images show a very fine and homogeneous distribution of chemically ordered domains within the disordered grains which induce tweed contrast. This is ascribed to coherency strains between the ordered domains and the cubic matrix. The SAED patterns show a general cubic symmetry, and confirm the coherency of the ordered domains with the cubic disordered matrix. As three orientational variants have been observed in sample 660R-s, it is therefore reasonable to think that they are also present in sample 550R-s.

Chemical analysis of sample 550R-s was performed in scanning transmission electron microscopy mode. Figure 3-13 shows elemental chemical maps where different colors correspond to the distribution of each element (Au, Cu and Ag) in the region of interest. The sample surface was heavily contaminated as indicated by the white arrow, however, the region delimited by the white rectangle does not show appreciable compositional changes on the specimen.
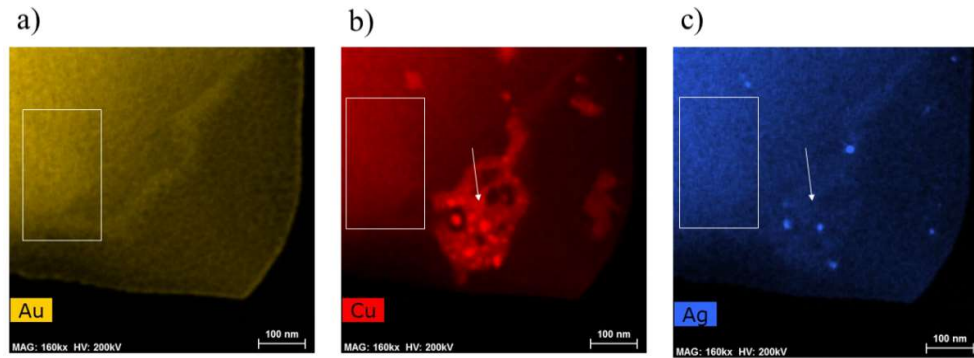
Figure 3-13 Elemental chemical maps obtained from X-ray chemical mapping in STEM mode.

In the purse of estimating the domain size of the ordered domains, high resolution transmission electron microscopy (HRTEM) was performed on sample 550R-s. Figure 3-14a shows a HREM image taken along the <110> zone axis with its corresponding Fast Fourier Transform (FFT) image as an inset. Figure 3-14b displays the Inverse Fast Fourier Transform (IFFT) of the super-lattice within a selected squared region of the HRTEM image, calculated by using the superlattice diffraction spots highlighted with white open circles in the FFT insert. Strong contrast variations (alternation of black and white atomic planes) are thought to correspond to chemically ordered domains, while weak contrast variations (grey-ish atomic planes) would correspond to chemically disordered regions.

The IFFT reveals a dense distribution of ordered domains which are no more than 2nm in size (equivalent to 5 $L1_0$ unit cells). The coherency between the ordered domains and the matrix results in a very diffuse boundary, making difficult to estimate the inter-domain distance. The lattice distortion that the ordered domains induce in the disordered matrix is evident and quite strong, as can be seen in the white rectangles in Figure 3-14b. Furthermore, two orientational variants relief the distortion by aligning their c-axis perpendicular to each other , as indicated by the white oval shape in Figure 3-14b; the white arrows indicate the direction of the c-axis of the respective domains.

Figure 3-14 a) HREM image along the [110] zone axis with the corresponding FFT image as an inset. b) IFFT image using the super-lattice spots in the FFT from the highlighted region on the HREM image White arrows indicate ordered domain, which show enhanced contrast due to the chemical ordering

3.4.2. Straightened state

Several attempts were done to observe the microstructure of a straightened wire at the center of a cross-section and in a near-the-surface region. The aim was to investigate possible microstructure variations due to the presence of plastic deformation.

Alike the rest of the samples in this chapter, which were prepared by electrolytic polishing, the focused ion beam (FIB) method was employed to prepare specimens from specific locations in the sample. Moreover, the samples that underwent plastic deformation showed strong stress-relief upon preparation, resulting in deformed TEM lamellas. This prevented proper sample alignment in the TEM along the zone axes.

- Center of the specimen

The DF images using the (001) and (1-10) superlattice spots in Figure 3-15a-b reveal a fine dispersion of ordered domains within the disordered matrix. The electron diffraction pattern shows the diffuse character of the super-lattice reflections.
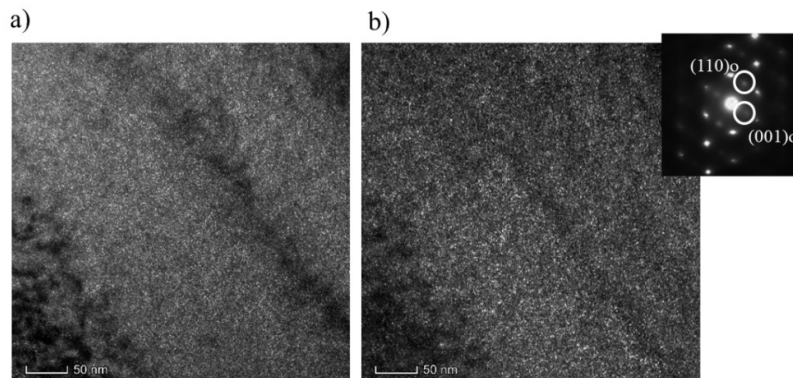
Figure 3-15 TEM DF image using a) the (001) superlattice spot and b) (1-10) superlattice spot along the [110] zone axis.

The electron diffraction pattern in Figure 3-16 corresponds to the [201] zone axis of the cubic matrix. The three orientational $L1_0$ variants are present in the microstructure, revealed by the weak spots highlighted by open white circles. DF imaging using the three super-lattice spots reveal a homogeneous and fine dispersion of precipitates within the disordered grains.
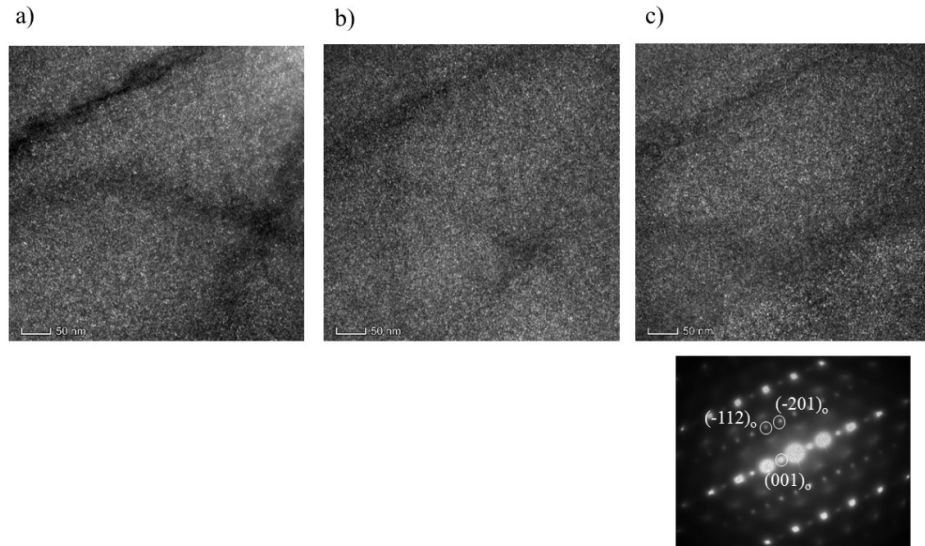
Figure 3-16 TEM DF images along the [201] zone axis using the a) (-201), b) (-112) and c) (-201) superlattice spots.

- Near-to-surface region

The DF images in Figure 3-17 and Figure 3-18 confirm the presence of a homogeneous and fine dispersion of ordered domains within the cubic matrix in the near-to-surface region. The observed zone axes only reveal the presence of two $L1_0$ variants. However, given the stage of ordering it is reasonable to assume that in the near-to-surface region, three $L1_0$ orientational variants are also present.
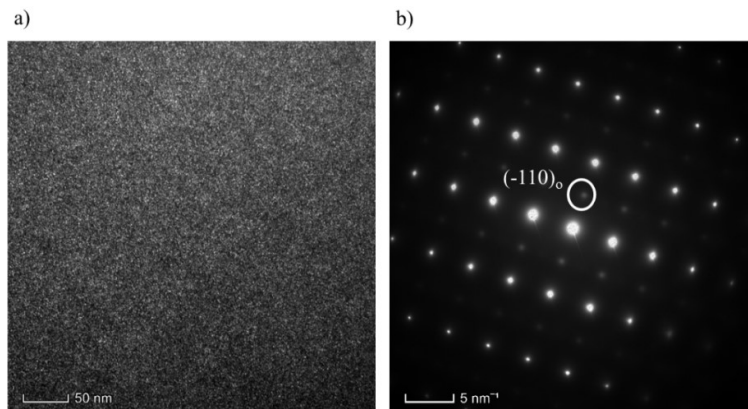
Figure 3-17 TEM DF image using the (-110) superlattice spot along the [112] zone axis
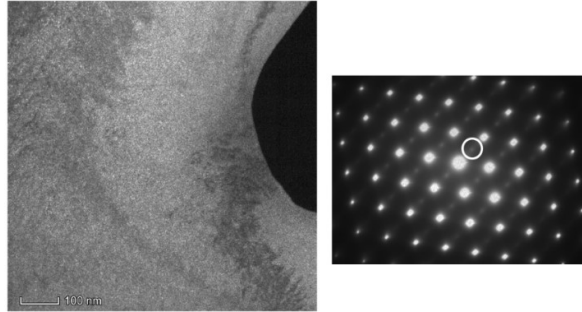
Figure 3-18 TEM DF image using the (001) superlattice spot along the [110] zone axis

 - Comparing the center and near-to-surface region

Electron diffraction patterns along the same zone axes were obtained for both specimens. Given that DF images did not reveal major microstructural differences, maybe some differences could be observed in the electron diffraction patterns. A comparison of electron diffraction patterns obtained along the same zone axis and in the same imaging conditions was performed. Table 3-3 displays the electron diffraction patterns along the [110] and [112] zone axes for the center and near-to surface regions in the sample 660RS. The intensity of the diffraction spots cannot be used as a comparison feature because it not only relates to the volume density of precipitates but also to the thickness of the specimen, which could not be successfully measured.

Table 3-3 Electron diffraction patterns along the [110] and [112] zone axes at the center and near-to-surface regions of sample 660RS.

Zone axis	Center	Near-to-surface
[110]		
[112]		

In general, after straightening, weak and broad super-lattice spots characterize the ordered microstructure. The distribution of the domains is homogeneous and very fine. Differences in domain size compared to R550-s and R660-s could not be assessed by standard TEM observations.

3.4.3. Bent state

The mechanical operations of straightening followed by bending do not change the grain structure nor produce grain refinement close to the surface. Figure 3-19 compares the microstructure of samples 550R-s and 550RSB-s. This observation is confirmed by EBSD examinations which show the same average grain size of 8μm in the bent sample.
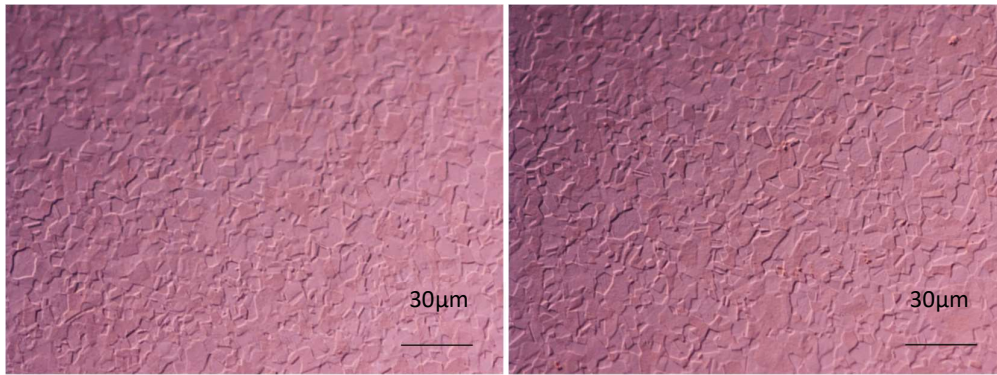
Figure 3-19 Optical micrograph. a) Sample 550R-s at the center, b) 550RSB-s at the center.

EBSD grain orientation maps reveal a mild texture change on the bent samples as compared to the recrystallized sample. From the pole figure in Figure 3-20, it is observed that the bent samples show an average [111] out-of-plane grain rotation, as opposed to the average [100] out-of-plane texture in the recrystallized condition. This texture changes are however so mild that IPD maps do not reveal clear texture tendencies.
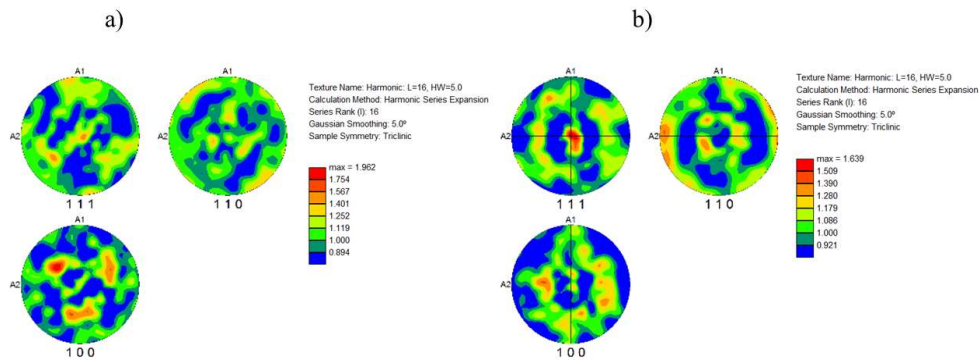
Figure 3-20 EBSD Pole figures a) sample 550R-s at the center and b) 550RSB-s at the center

BF images of sample 660RSB-s reveal an enhanced mottled contrast, whereas the surface condition of sample 550RSB-s is not good enough to withdraw any conclusions, see Figure 3-21a-b, respectively.
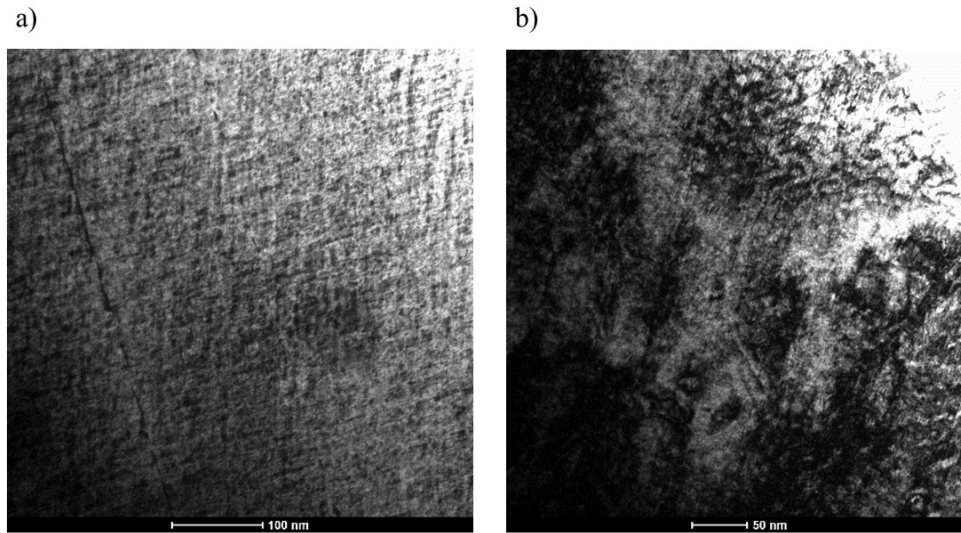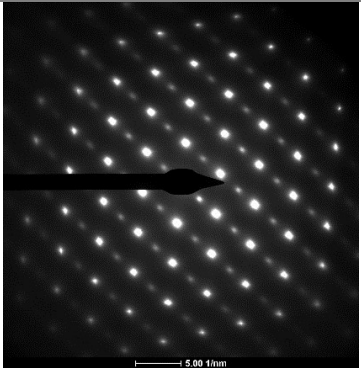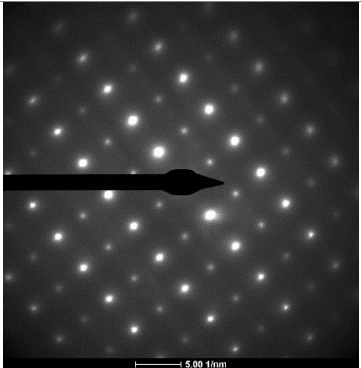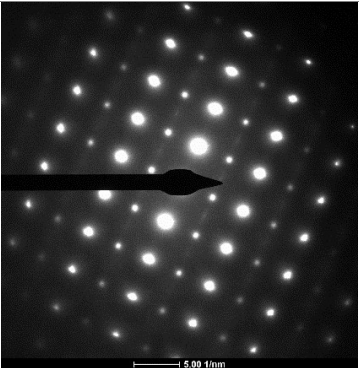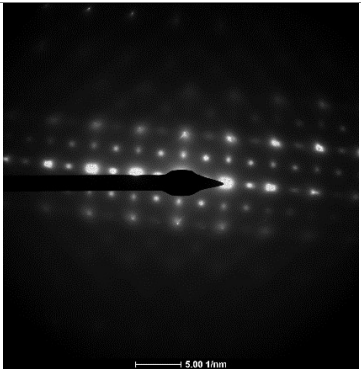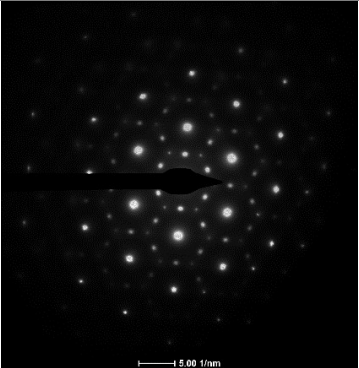
Figure 3-21 TEM BF image a) sample 660RSB-s and b) sample 550RSB-s

It is noted that the plastic deformation induced during the bending operation of the U-shaped sample is not homogeneous through the cross-section of the sample. Therefore, the prepared specimen for TEM observation (by electrolytical polishing) was not necessarily representative of the center of the cross-section nor near-to-surface region. Comparisons between 550RSB-s and 660RSB-s was impossible.

However, a common feature between the 550RSB-s and 660RSB-s samples is that the super-lattice spots become more intense, as shown in Table 3-4 DF imaging in Figure 3-22a and Figure 3-23a-b reveal a homogeneous distribution of ordered domains for the [112] and [110] zone axes, respectively. Furthermore, comparison of DF images using the (1-10) super-lattice reflection between the bent (550RBS-s, 660RSB-s), straightened(660RS-s) and recrystallized (550R-s) states suggest that the ordered domain size in the bent samples (Figure 3-22a-b) is slightly greater as compared to that in the straightened (b) and recrystallized (Figure 3-22c) samples.

Table 3-4 Electron diffraction patterns along different zone axes for samples 660RSB and 550RSB

Zone axis	660RSB	550RSB
[110]		
[112]		
[001]		
[111]		
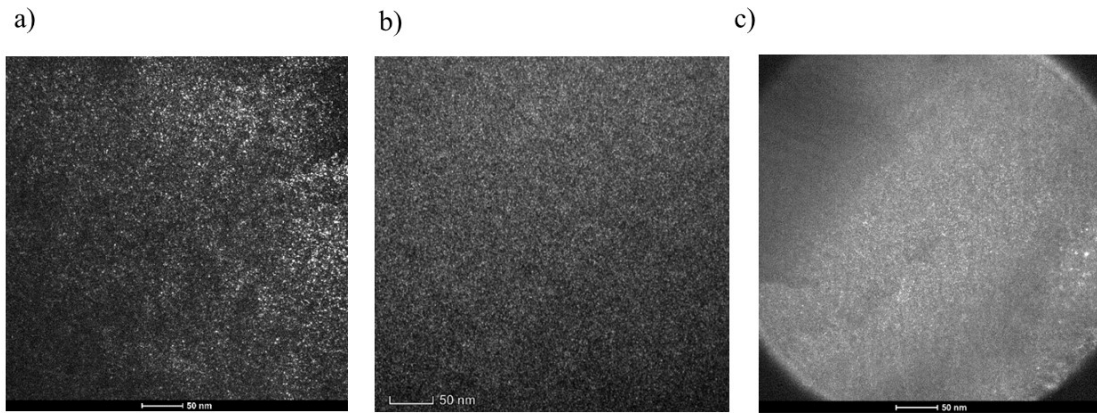
Figure 3-22 TEM DF image using the (-110) reflection along the [112] zone axis for a) 550RSB-s and b) 660RS-s near the surface; c) DF using the (-110) super-lattice spot along the [110] zone axis in R550-s.
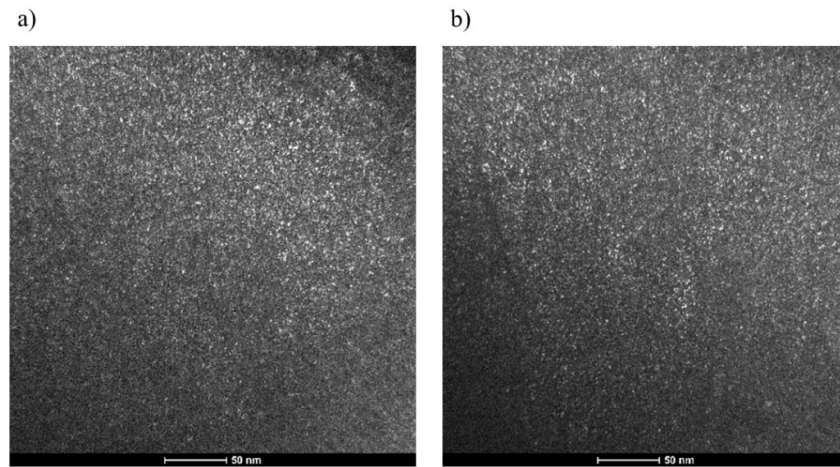
Figure 3-23 TEM DF images obtained using the a) (-110) and (001) reflections along the [110] zone axis on sample 660RSB-s.

The three $L1_0$ orientational variants are still present in the bent samples, as shown by the electron diffraction pattern obtained along the [111] zone axis displayed in table 3. DF images on the {110} super-lattice spots along such a zone axis display a homogeneous distribution of the three orientational variants, see Figure 3-24.
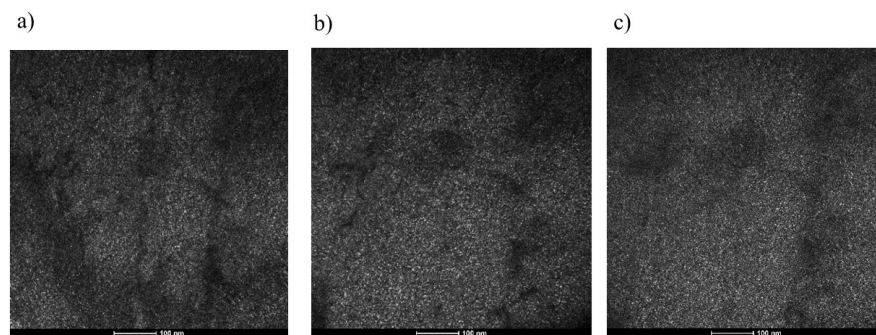
Figure 3-24 TEM DF images using the a) (1-10), b (-110) and c) (-101) diffraction spots along the [111] zone axis in sample 550RSB

65

In summary, bent samples reveal a slight increase in super-lattice spot intensity. The three orientational $L1_0$ variants are present in the microstructure and homogeneously distributed among the ordered grains. DF imaging suggest that the ordered domains are slightly greater in size as compared to straightened and recrystallized samples. The former observations would imply that order is more advanced in the bent condition. However, differences remain small and TEM investigations are not the most suited characterization technique to address this matter.

Finally, dislocation networks were observed in thick samples supposedly induced during the bending operation, as seen in Figure 3-25. Unfortunately, the specimen thickness required to observe dislocations is too big to perform DF imaging of ordered domains in the same region.
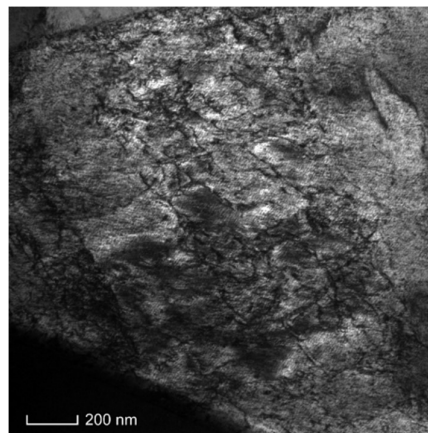
Figure 3-25 TEM BF image of dislocation networks in 660RSB-s

3.4.4. Furnace brazed state

The combination of high temperatures (i.e. 860°C) and fast cooling rates (-700°C/min) during the furnace brazing treatment results considerable ordering during cooling and or natural ageing, this is ascribed to enhanced ordering due to the high density of quenched-in excess vacancies [45]. Extensive grain growth happens at 860°C suggesting that dislocations from the previous mechanical operations are annealed-out. Optical examinations illustrate that grain growth is dependent on the thermo-mechanical history of the sample. For instance, the sample 550RSBF-s shows an average grain size of 110μm, while sample 660RSBF-s exhibits a greater average grain size around 250 μm. Moreover, the absence of mechanical operations (sample 550RF-s) displays the greatest grain sizes around 500μm. See Figure 3-26.
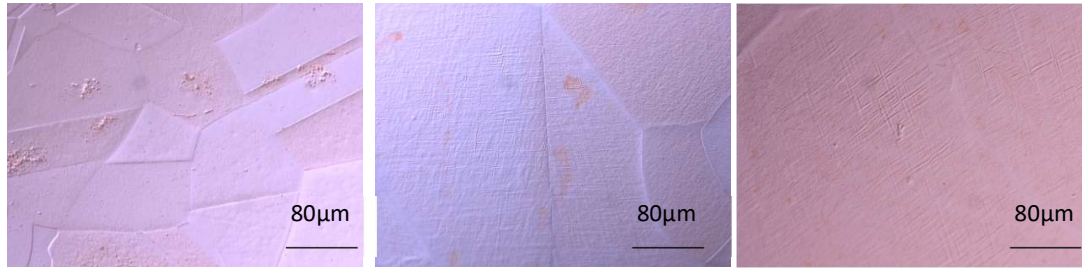
Figure 3-26 Optical micrograph a) 550RSB, b) 550RSB, c) 660RSB.

Sample 550RF-s displays the greatest degree of order and it is sufficiently advanced to reveal surface relief effects in optical micrographs. Figure 3-27 a-c reveals surface relief effects and cross-like features within the grains, which are typical indicators of order. High-resolution EBSD examinations on grains exhibiting these features were performed. Firstly, inverse pole figure maps show the presence small misorientations organized as a lamellar structure within the grain, see Figure 3-28a. High magnification maps on areas containing cross-like features fail to obtain proper electron back scattered diffraction patterns from the feature itself. This suggests that these areas are highly distorted and/or too small to be indexed. Figure 3-28b shows an EBSD IPF map on an area with a cross-like feature, the black pixels correspond to areas that were not indexed during the EBSD processing.
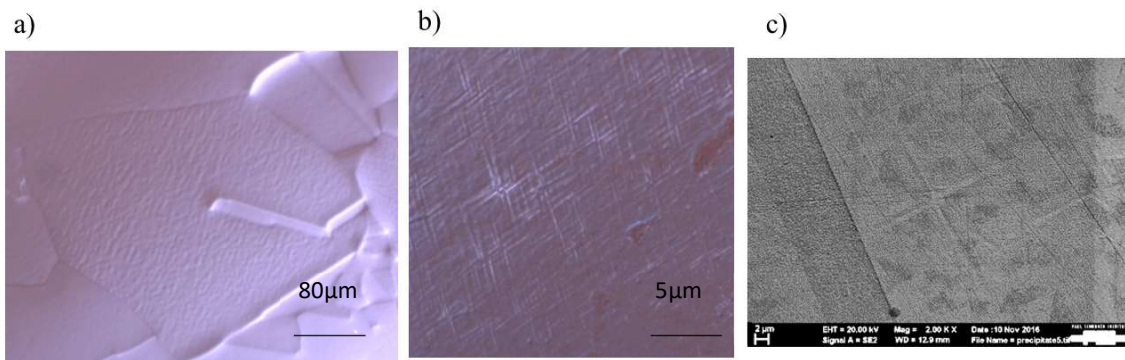
Figure 3-27 DIC optical micrographs in sample 550RF-s. a) grain with surface relief contrast, b) grain with cross-like features; c) cross-like features observed in SEM
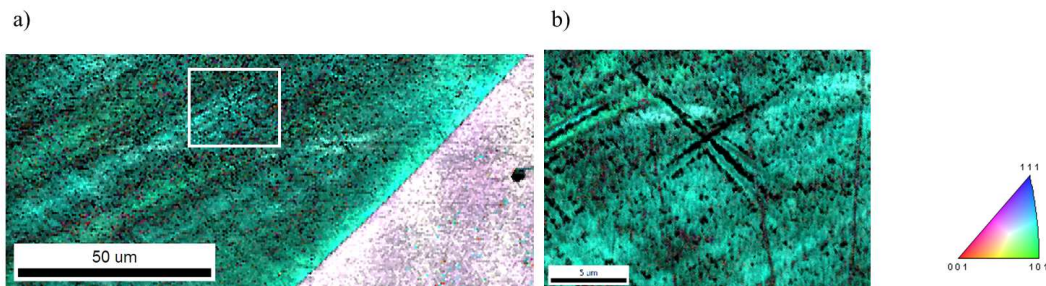
Figure 3-28 a) EBSD IPF map revealing a lamellar configuration of small misorientations within the grains. b) High magnification EBSD IPF map on a cross-like feature

Furnace brazed state after mechanical deformation: 550RSBF and 660RSBF

BF images show a marked microstructural difference for the furnace brazed samples depending on the initial recrystallization heat treatment. On the one hand, sample 550RSBF-s shows a contrast similar to that of tweed. On the other hand, sample 660RSBF-s shows clear sets of twins, as indicated by the white lines in Figure 3-29b. Note that the grain size in the sample 550RSBF is in average 100μm, whereas on sample 660RSBF contains grains about 250μm diameter.
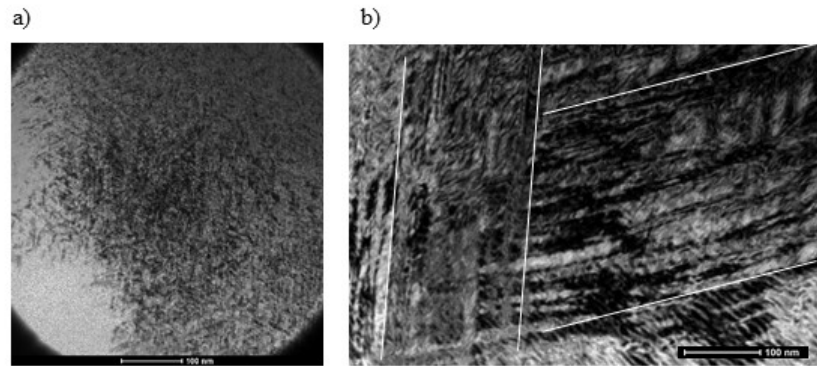
Figure 3-29 TEM BF image for a) 550RSBF-s and b) 660RSBF-s

The microstructural details of samples 550RSBF-s and 660RSBF-s are emphasized in what follows. Sample 550RSBF-s reveals a tweed microstructure, as displayed by the DF images shown in Figure 3-30 and Figure 3-31. The observed ordered domains arrange in bands that align along specific directions, as indicated by the white arrows. Each band is composed of nano-sized ordered domains, as shown in Figure 3-32. It is possible that the black worm-like boundaries between the ordered domains correspond to antiphase boundaries, due to the coalescence of two out-of-step ordered domains.
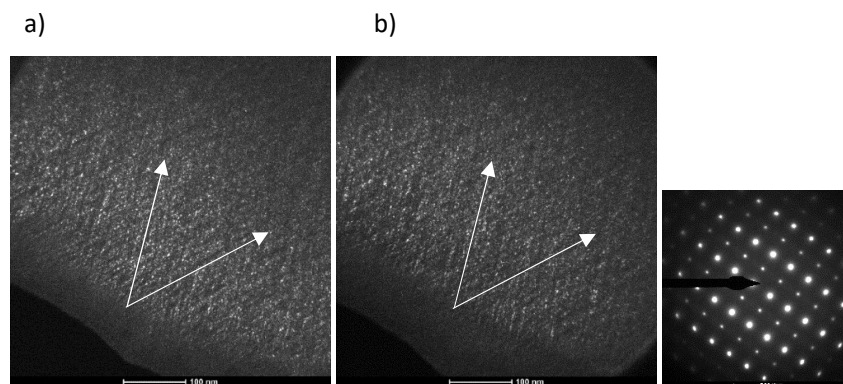
Figure 3-30 TEM DF image along the [112] zone axis using the a) (-110) and b) (-201) super-lattice spots on sample 550RSBF-s

a)   b)
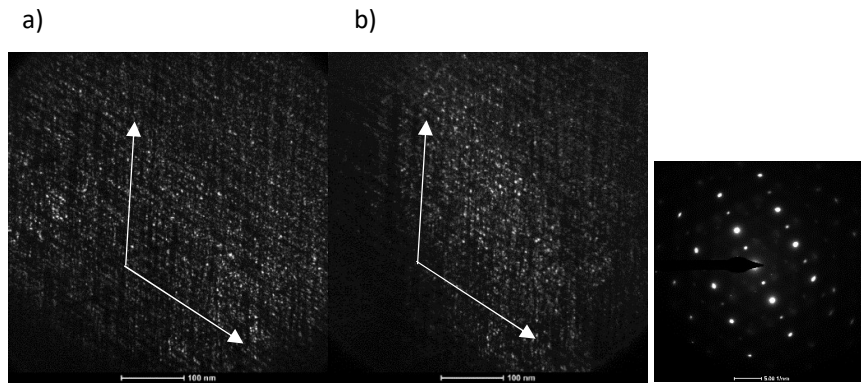
Figure 3-31 TEM DF image along the [210] zone axis using the a) (001) and b) (-241) super-lattice spots on sample 550RSBF-s

a)   b)

50nm   50nm
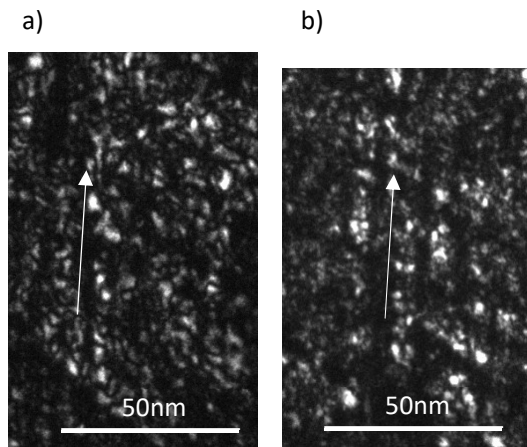
Figure 3-32 Detail of the DF images shown in figure 3-31 a) and b) respectively.

 The electron diffraction pattern along the [110] zone axis, which is subject to <110> streaking due to coherency strains, is shown in Figure 3-33. Unfortunately the acquired image was slightly out of focus.
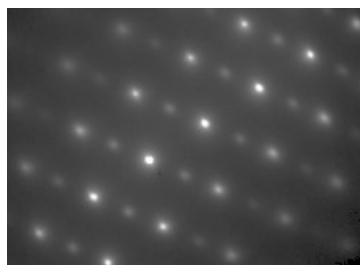
Figure 3-33 SAED pattern along the [110] zone axis showing a slight <110> streaking of the fundamental spots.

EDS chemical mapping in STEM mode does not reveal any elemental segregations in the site of interest, as shown in Figure 3-34. Figure 3-35 displays elemental chemical maps, notably those of gold, silver and copper. The results of the chemical composition analysis are shown in Table 3-5, showing the expected nominal chemical composition for red gold.
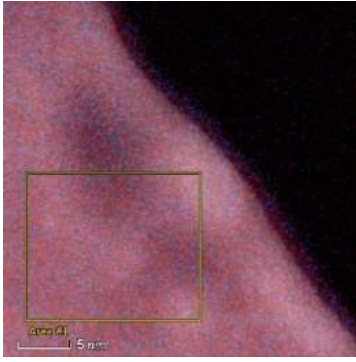
Figure 3-34 Region of interest for STEM EDS chemical mapping. The obtained chemical composition refers to the squared zone, denoted Area 1

a)   b)   c)
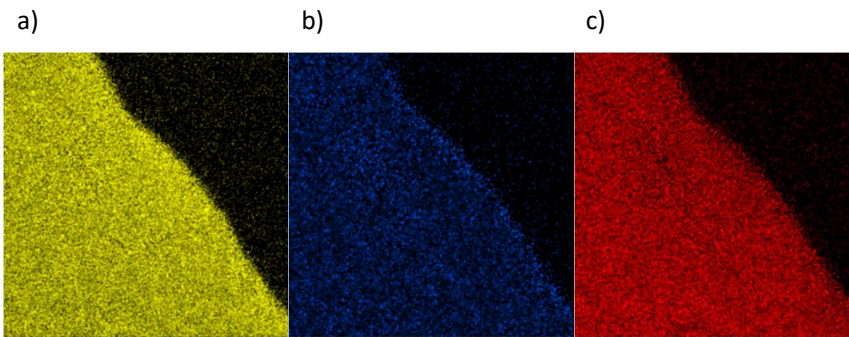
Figure 3-35 STEM EDS elemental chemical maps for a) gold, b) silver and c) copper

Table 3-5 Chemical composition from Area 1 shown in Figure 3-34

Z	Element	Family	Atomic Fraction (%)	Atomic Error (%)	Mass Fraction (%)	Mass Error (%)	Fit Error (%)
29	Cu	K	44.85	5.41	21.65	2.24	0.08
47	Ag	K	5.05	0.80	4.19	0.61	0.98
79	Au	L	50.10	7.50	74.16	10.11	0.08

Results of HRTEM investigations on 550RSBF-s along the low symmetry [112] zone axis are shown in Figure 3-36a. Ordered domains are characterized by the alternance of intense and less intense horizintal atomic ranges in HRTEM images, while disordered regions are characterized by the alternance of horizontal atomic rows with similar intensities. The boundaries between disordered and ordered regions are only visible by calculating the IFFT of HRTEM images using the superlattice reflections shown in the FFT insert in Figure 3-36a. Figure 3-36b displays the resulting IFFT. In this case, the ordered domains seem to cover a greater area as compared to the disordered matrix. White lines in Figure 3-36 indicate the regions, maybe boundaries, between the ordered domains. The characteristic size of the domains varies between 1nm and 2nm. These observations are consistent with the DF images taken along the [112] zone axis and shown in Figure 3-18. Figure 3-37 shows a zoomed area of the DF image reported in figure 18a, showing domain sizes around 1-2nm and disordered boundaries between the domains as highlighted by the white lines.
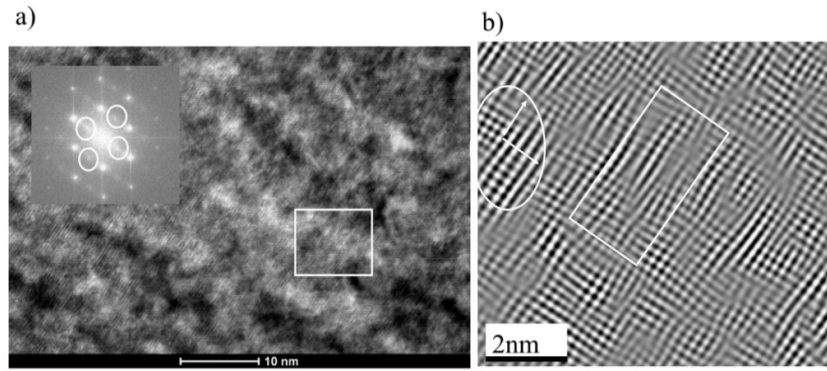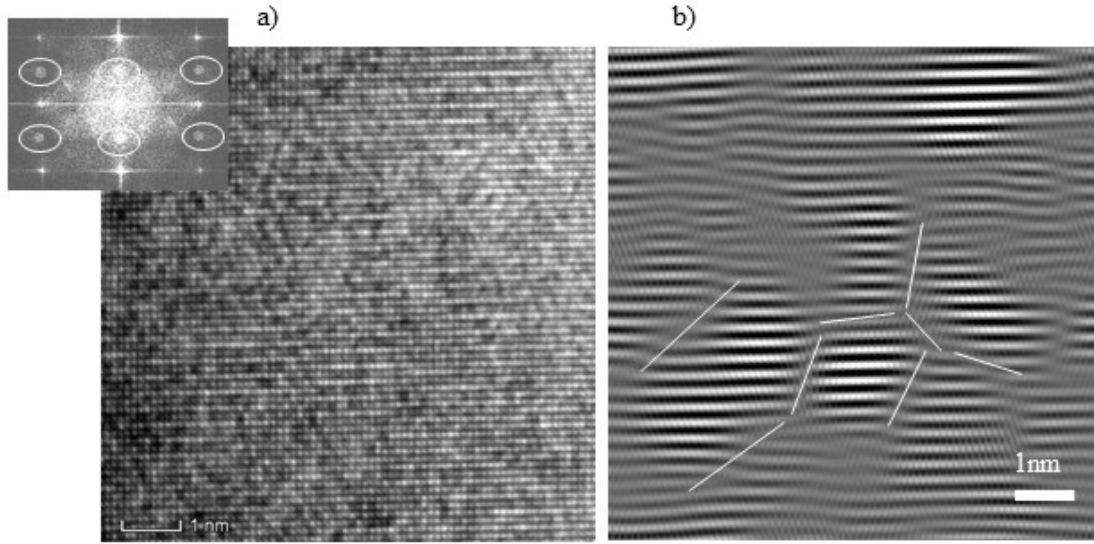
Figure 3-36 a) HRTEM image along the [112] zone axis with its corresponding FFT in insert. b) IFFT image using four superlattice reflections highlighted in the FFT insert. White lines indicate the presence of disordered regions between ordered domains.
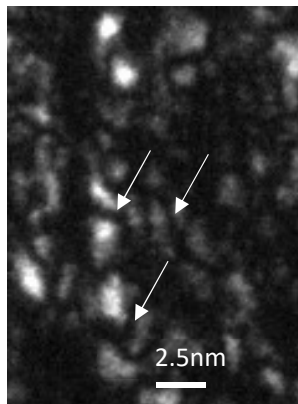
Figure 3-37 TEM DF image along the [112] zone axis using the (001) super-lattice spot. Zoomed region from figure 18a.

Sample 660RSBF-s shows a coarser tweed structure, as shown by the DF images along the [110] zone axis and reported in Figure 3-38a-b. The bands that form the tweed structure are also composed of nano-ordered domains, probably separated by APBs as suggested by Figure 3-38c. The dark areas observed in the DF images obtained using the $(001)_o$ reflection in Figure 3-38 a-b can belong to either the disordered matrix or the $L1_0$ variant with the c-axis out-of-plane. DF images on the fundamental (002) and (2-20) spots show enhanced contrast on such areas see the bands indicated by white arrows in Figure 3-40. The disordered matrix also exhibits the tweed structure.
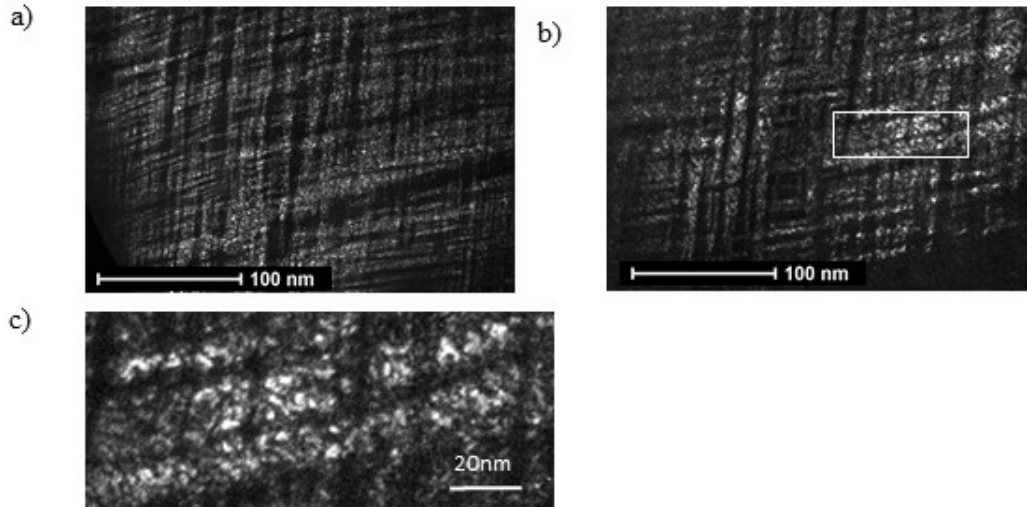
Figure 3-38 TEM DF image along the [110] zone axis obtained using the a) (001) and b) (1-10) super-lattice spots; c) detail of the highlighted region in b).
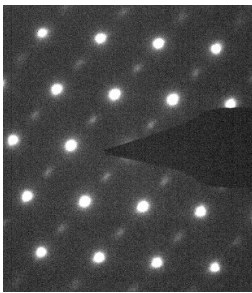
Figure 3-39 SAED pattern of the [110] zone axis.
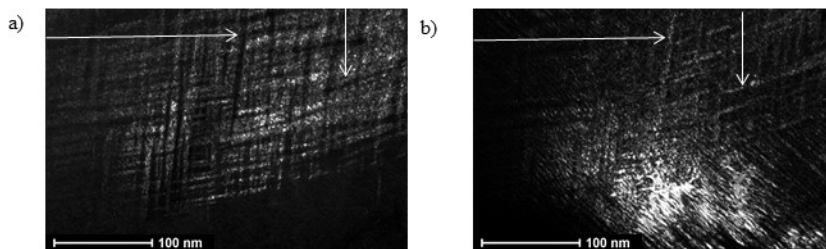
Figure 3-40 TEM DF micrographs along the [110] zone axis using a) the (001) superlattice spot and b) the fundamental (002) spot.

To summarize, continuous cooling from the brazing temperature of 860°C results in a cooling rate sufficiently fast that results in an advanced ordered microstructure, as compared to previous thermo-mechanical operations. It seems that the grain size plays a major role on the development of the microstructure, as suggested in [46,71]. Another factor that can control the ordering kinetics upon cooling from 860°C is the cooling rate; however, both samples were treated in the same furnace using the same geometry. Sample 550RSBF (smaller grain size) shows a tweed microstructure, where each tweed band is composed of nano-sized ordered domains probably separated by APBs. Slight <110>

72

streaking is observed for the [110] zone axis. Sample 660RSBF (greater grain size) shows a coarser tweed structure. Each tweed band is composed of nano-sized domains. No <110> streaking is observed for the [110] zone axis. There seems to be ordered and disordered bands. The general symmetry of the system remains cubic.

Furnace brazed state without mechanical deformation: 550RF

The sample 550RF-s does not undergo mechanical operations and is directly furnace brazed after the recrystallization heat treatment. The ordered microstructure in 550RF-s is the most advanced of all samples. BF images in Figure 3-41 show clear bands aligned along the g= [001] direction. The electron diffraction pattern of the [001] zone axis in Figure 3-41 show the presence of the three orientational variants. The white arrows in the same figure suggest splitting of the fundamental spots. However, the observation of the three $L1_0$ orientational variants under the same zone axis indicates that the lattice is cubic in symmetry, thus the observed splitting around the fundamentals cannot belong to the $L1_0$ phase. DF using the (001) superlattice spots in Figure 3-42 a-b reveals that the ordered twin bands are arranged such that the c-axis are rotated 90°. The white arrows indicate the direction of the c-axis within a selected twin set bounded by white lines. Figure 3-42c shows the DF image of the (002) fundamental spot. Moreover, DF image obtained with the (110) superlattice spot along the [001] zone axis shows the presence of antiphase boundaries, characterized by a worm-like dark structure, see Figure 3-43.
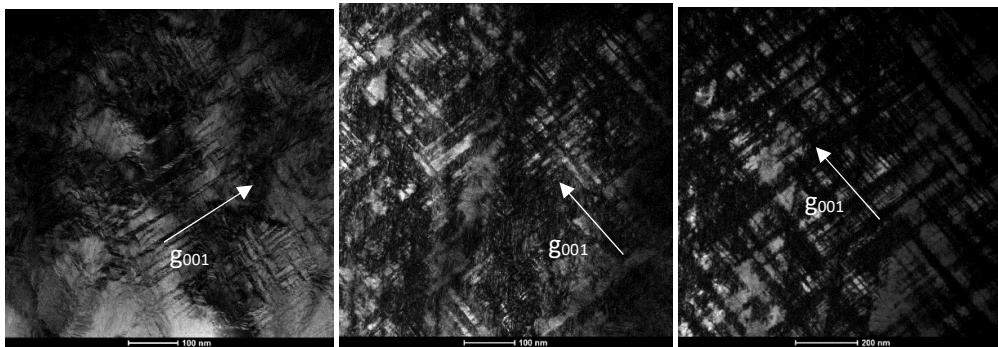
Figure 3-41 TEM BF image showing twins aligned on the [110].
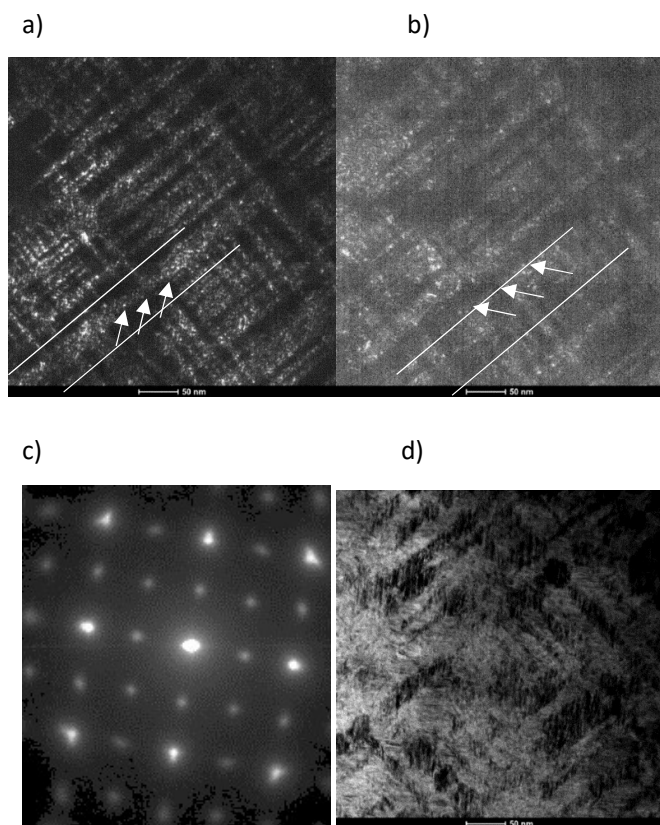
Figure 3-42 TEM DF image along [100] zone axis using a) the (001) from orientational variant 1 superlattice spot, b) the (001) spot of orientational variant 2 and c) (002) fundamental spot.
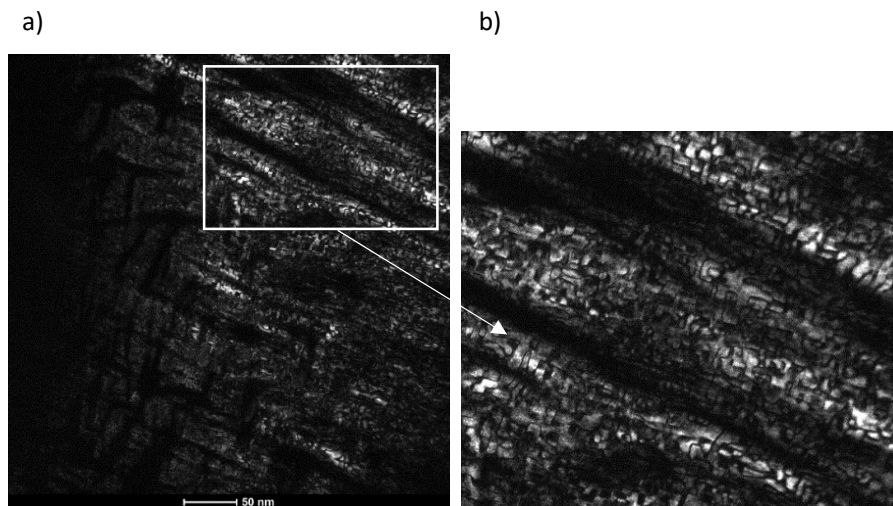
Figure 3-43 TEM DF image along the [001] zone axis on the (110) superlattice spot showing antiphase boundaries.

STEM EDS chemical mapping was performed in the same region (Figure 3-44a), which showed the presence of a twin delimited by white lines. Corresponding elemental chemical maps in Figure 3-44 b-d show no clear segregation of Ag and a homogeneous distribution of the three atomic species.

Table 3-6 shows the chemical composition expected for red gold, accounting for the uncertainty in measurements.
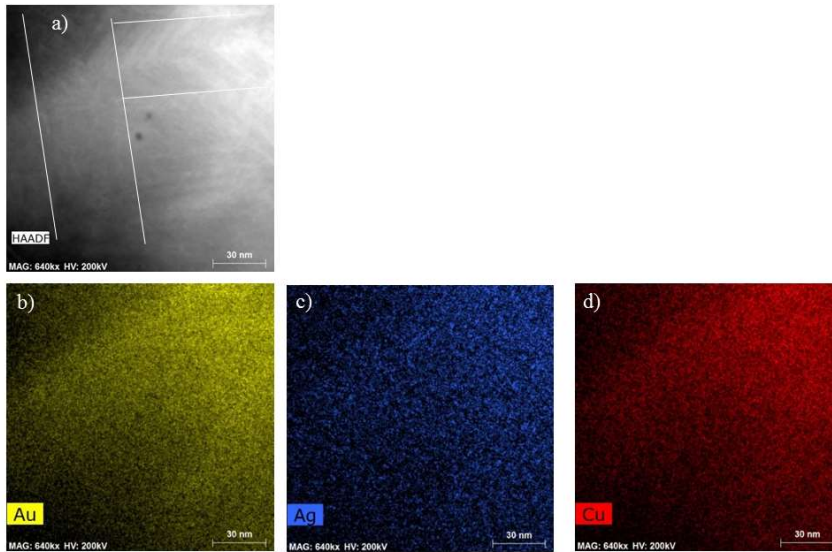
Figure 3-44 a) region of interest for the chemical mappings, b-c-d) Elemental chemical maps of Au, Ag and Cu respectively

Table 3-6 Chemical composition of sample 550RF

Element	series	Net	wt.%	norm. wt.%	norm. at.%	Rel. error % (2σ)
Copper	K-series	108312	19.346	19.346	41.600	6.293
Silver	L-series	20007	4.232	4.232	5.363	21.259
Gold	L-series	234861	76.429	76.421	53.027	20.073

Finally, Figure 3-45 shows a HRTEM image performed on the 550RF-s sample. Particularly, 90° twinned ordered domains can be seen in the HRTEM image, as indicated by the white lines. It is to be noted that ordered zones appear as series of alternate white atomic rows and darker atomic rows (see e.g. the center or upper right part of the picture), while disordered zones exhibit a homogenous image contrast (see e-g. the lower left part of the picture).
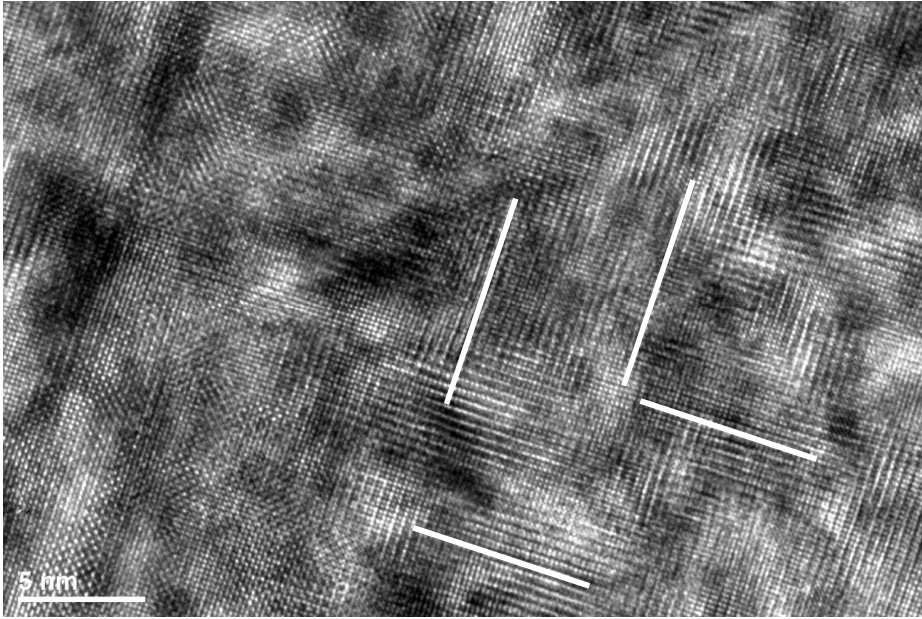
Figure 3-45 HRTEM along the [100] zone axis, showing twinned ordered domains.

3.5. Summary

Table 3-7 summarizes the major microstructural features observed at each thermo-mechanical processing step together with the processing parameters.

Table 3-7 Microstructural features observed at each thermo-mechanical processing step associated to the processing parameters

Sample	Stage of ordering	Major microstructural features	Processing parameters
550R-s 660 R-s	Early stages	Homogeneous dispersion of ordered domains High density of nano-sized domains within the disordered grains 3 $L1_0$ variants Chemical segregation not observed	Recrystallization T Cooling rate
660RS-s	Early stages	Homogeneous dispersion of ordered domains High density of nano-sized domains within the disordered grains 3 $L1_0$ variants	Recrystallization T Cooling rate Plastic deformation near-to-surface
550RSB-s 660RSB-s	Early stages	Homogeneous dispersion of ordered domains High density of **bigger** nano-sized domains within the disordered grains 3 $L1_0$ variants	Recrystallization T Cooling rate Plastic deformation heterogeneous
550RSBF-s	Fine Tweed	Tweed structure in the arrangement of ordered domains Tweed bands composed of nano-sized APB present Chemical segregation not observed Grain size ⸱ 100μm	Recrystallization T Cooling rate Plastic deformation heterogeneous Grain growth at 860°C Fast cooling from 860°C
660RSBF-s	Coarse Tweed	Coarse tweed structure in the arrangement of ordered domains Tweed bands composed of nano-sized APB present	Recrystallization T Cooling rate Plastic deformation heterogeneous

		Chemical segregation not observed	Grain growth at 860$^{\text{o}}$C
		Grain size � 250μm	Fast cooling from 860$^{\text{o}}$C
550RF-s	Nano twins	Twinned structure	Recrystallization T
			Cooling rate
		Twin bands composed of nano-sized	Plastic deformation
		APB present	heterogeneous
		Chemical segregation not observed	Grain growth at 860$^{\text{o}}$C
		Grain size ⊂ 350μm	Fast cooling from 860$^{\text{o}}$C

Chapter 4   Isothermal treatments

This chapter studies the microstructural evolution of red gold under isothermal ageing conditions, at temperatures below the critical temperature T_{OD}.

The first section describes the microstructural evolution after isothermal ageing at 100⁰C, 200⁰C, 280⁰C, 310⁰C and 330⁰C on samples from Batch III.

The second section addresses the influence of the initial condition on the natural ageing behavior of samples that were thermo-mechanically processed in industry, with particular focus on 1) the influence of the cooling rate and 2) the combination of cooling rate and plastic deformation. The investigated samples belong batches I and II.

The third section explores the influence of the initial condition on ordering. Firstly, *ex situ* X-ray profiles are performed on industrially deformed samples (straigthened) and subsequently isothermally aged at 100⁰C, 250⁰C and 330⁰C. Secondly, in situ X-ray isothermal ageing experiments are performed at 250⁰C on samples thermo-mechanically treated under controlled laboratory conditions

The main objective of this chapter is to reveal the microstructural evolution upon ordering and to evaluate how it changes when the initial conditions are changed.

4.1. Initial microstructures

4.1.1. Microstructure of a nearly fully ordered L1$_0$

Figure 4-1a displays the powder diffraction pattern of a sample isothermally treated at 330°C for 12h. It can be indexed as a mixture of an L1$_0$ and an α_2 phase. The calculated lattice parameters for the L1$_0$ phase are a=3.97Å and c=3.67Å, which results in c/a=0.92, in agreement with literature values for AuCu-I [51]. The tetragonal L1$_0$ structure is characterised by superlattice reflections, i.e. (001),(110),(201) and (112), and a clear separation of the diffraction of the {200} and {220} families. The α_2 phase is a solid solution of Ag in an fcc Au matrix and is visible as low-angle shoulders of the fundamental L1$_0$ peaks. Figure 4-1b displays the corresponding TEM BF image. It shows the characteristic polytwinned configuration of an ordered structure [51,68,136,137]. The calculated long-range order parameter S is equal to 0.92, following the definition of S in section 2.4.5 and considering the {220} and (110) diffraction peaks.
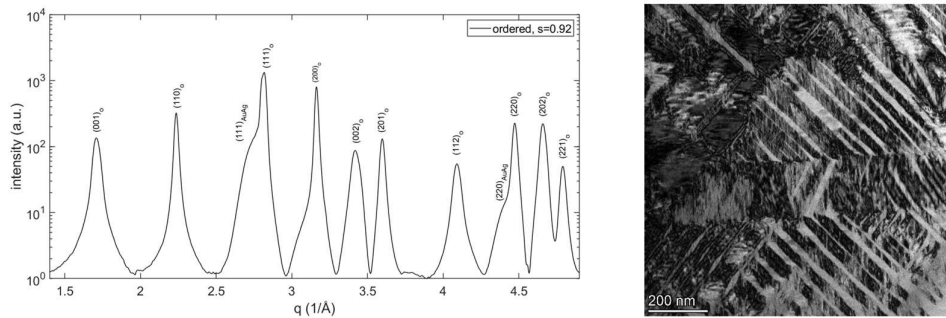
Figure 4-1 a) powder diffraction pattern of a sample isothermally treated at 330C during 12h. b) BF TEM image showing the characteristic polytwinned microstructure of the sample isothermally treated at 330°C for 12h.

4.1.2. Microstructure after continuous cooling

The microstructure obtained in continuous cooling furnaces is of paramount importance because it is the initial condition for the isothermal ageing studies as well as one of the intial conditions for the *in situ* thermal experiments.

Figure 4-2 compares the powder diffraction pattern of a sample cooled down from 660°C at -100°C/min with the sample treated at 330°C for 12h. The powder diffraction pattern of the fast cooled sample shows the fundamental (111)$_d$, (200)$_d$ and (220)$_d$ reflections that belong to the metastable disordered cubic phase with a lattice parameter a=3.89Å, as well as broad and low intensity super-lattice reflections, showing that chemical order is present in the sample. The peak positions of the super-lattice reflections are shifted from the equilibrium L1$_0$ positions. Indeed, the peak positions correspond to a nearly cubic matrix, indicating that the ordered domains are coherent with the disordered cubic matrix. Moreover, the fundamental ordered reflections are not observed because, due to coherency, they overlap with the fundamental reflections of the disordered matrix.
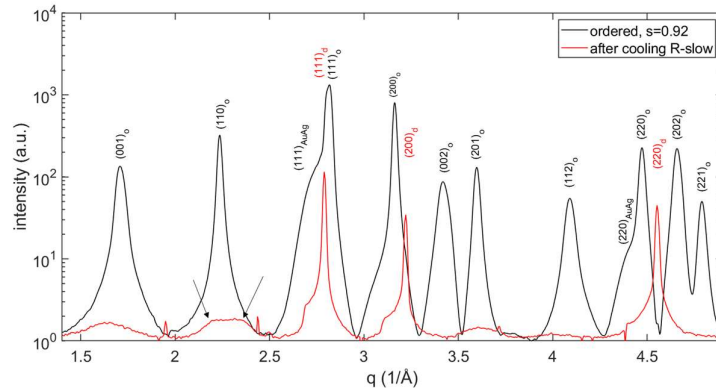
Figure 4-2 Powder diffraction pattern comparing the microstructure after cooling and close to fully ordered.

Furthermore, two broad maxima are observed around the $(110)_o$ peak instead of the expected single peak. This is a scattering phenomenon characteristic of disordered microstructures with embedded nano-sized ordered domains[85]. Constructive interference is observed when short-range order spatial correlations exist between ordered domains in an anti-phase configuration. In other words, this suggests that nano-sized ordered domains are densely and homogeneously distributed within the disordered grain.

High-resolution TEM investigations reveal the presence of a fine and homogeneous distribution of nano-sized ordered domains within the disordered cubic grains. Inverse fast Fourier transform (IFFT) images showed that the ordered regions extend up to 2nm in size ($\approx$ 6 atomic planes) and that they densely populate the disordered grains. The diffuse interface between the disordered matrix and the ordered domains does not allow to accurately estimate the inter-domain distance, but it is well below 10nm.

The former observations reveal that cooling at -100C/min from 660°C retains the metastable disordered cubic phase at room temperature that coexists with chemically ordered and nano-sized domains (and minor α_2 phase).

4.2. Microstructural evolution under isothermal ageing conditions

Isothermal ageing treatments at 150°C, 200°C, 280°C, 310°C and 330°C were applied on recrystallized wires of red gold . The duration of the thermal treatment varied between 5, 10 and 20 minutes for each ageing temperature. Chemical ordering can be followed by the evolution of the superlattice reflections $(001)_o$, $(110)_o$, $(201)_o$ and $(112)_o$ and the peak split on the fundamental (200) and (220) planes, related to the tetragonal distortion of the $L1_0$ phase (c/a). Therefore, special attention is put in the evolution of the superlattice peaks and the fundamental (200) and (220) peaks shapes

Figure 4-3 shows the X-ray powder diffraction patterns that correspond to a sample treated at low temperature (150°C, 5min) and a sample treated at high temperature (280°C, 20 min). Each peak is indexed. The subindex d denotes the disordered cubic matrix, while the subindex o corresponds to the ordered $L1_0$ phase. Ageing at 150°C shows very broad superlattice reflections, as well as overlapping (111), (200) and (220) fundamental reflections of the ordered and disordered phase. The latter indicates coherency between the disordered matrix and the ordered precipitates. The log-scale in the intensity axis allows highlighting the tails of the fundamental peaks. Increased intensity is observed on the tails of the fundamental $(200)_d$ and $(220)_d$ peaks on the sample treated at 150°C during 5 min. The sample heat treated at 250°C during 20 minutes exhibits greater intensity of the superlattice reflections, indicating that more chemical ordering is achieved after such treatment. Interestingly, the fundamental $(200)_d$ peak is no longer observed, a peak split is observed instead. The same happens with the fundamental $(220)_d$ peak.
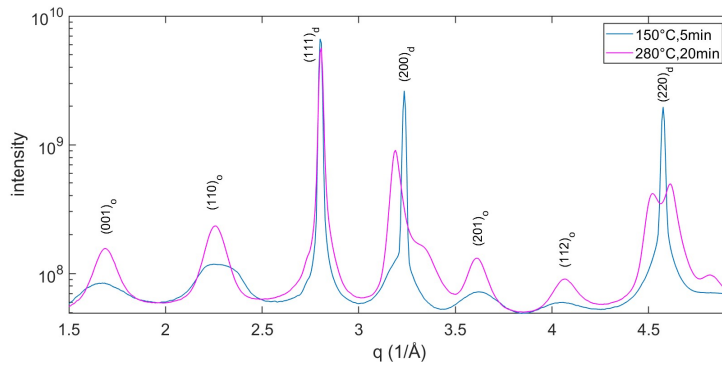
Figure 4-3 Powder x-ray diffraction pattern of samples isothermally treated during 20minutes at 150°C and 280°C, respectively.

Figure 4-4ab show the evolution of the X-ray powder diffraction patterns for samples isothermally treated during 5, 10 and 20 minutes at 150°C and 200°C, respectively. With increasing ageing time the superlattice reflections increase in intensity, as well as the tails of the fundamental $(200)_d$ and $(220)_d$ peaks. This indicates that ordering, i.e. increase of intensity of the superlattice reflections, is related to the increasing intensity of the tails.

Figure 4-4c shows the evolution of the X-ray powder diffraction patterns for samples isothermally treated during 5, 10, 20 minutes at 250°C. With increasing ageing time, the greater intensity of the $(200)_d$ and $(220)_d$ tails evolve into the previously mentioned peak splitting. At the same time, the superlattice reflections continue to grow in intensity, indicating that chemical order progresses within the sample. The faster development of the superlattice peaks and the peak splitting is indicative of a faster ordering rate at 280°C. It is unlikely that the formation of α_2 phase (FCC AuAg solid solution)

could explain the observed changes in the tails of the $(200)_d$ and $(220)_d$ and the subsequent peak splitting.
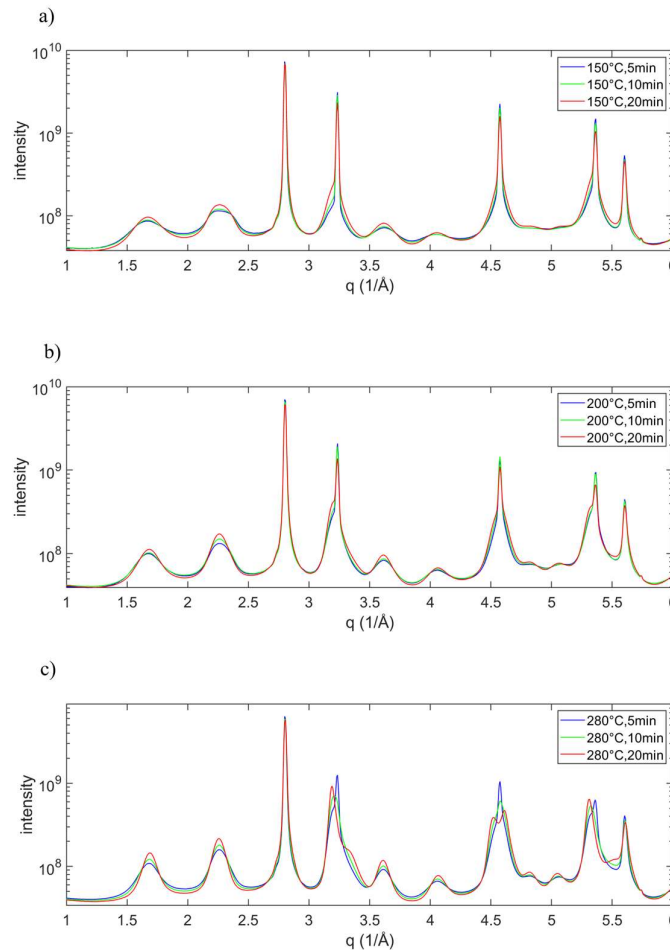
Figure 4-4 Powder diffraction patterns after isothermal treatments at a) 150°C, b) 200°C and c) 280°C.

Figure 4-5a shows the evolution of the $(200)_d$ and $(220)_d$ fundamental peaks upon isothermal ageing at 100°C, 200°C and 280°C during 20 minutes. Note that the y-axis scale is linear. The $(200)_d$ shows a clear split after ageing at 150°C, while the $(220)_d$ exhibits increased intensity of the tails. After 20 minutes at 280°C ageing, the $(220)_d$ peaks shows a clear split. Figure 4-5b displays better the evolution of the $(220)_d$ peak. After 10 minutes ageing, the peak shows a complex shape, which contains the $(220)_d$ peak and the split peaks. This suggests that the intensity increase of the tails corresponds the growth of the split peaks. Furthermore, the $(220)_d$ peak seems to coexist with the split peaks. The split peaks grow in intensity at the same time that the intensity in the $(220)_d$ decreases.
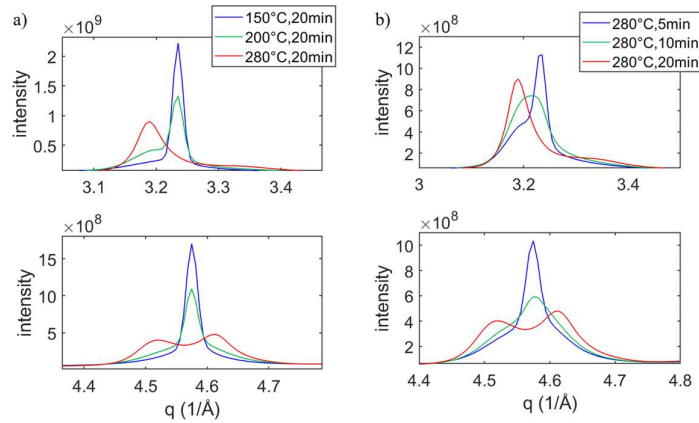
Figure 4-5 a) Comparison of the (200)d and (220)d fundamental diffraction peaks after ageing at 150°C, 200°C and 280°C during 20 minutes; b)Comparison of the (200)$_d$ and (220)$_d$ fundamental diffraction peaks after ageing at 280°C during 5, 10 and 20 minutes, respectively

4.2.1. Distortion of the disordered FCC phase

The peak splitting evolves with the progress of the ordering transformation. In order to understand the evolution of such split during ordering, additional samples were heat treated at higher ageing temperatures. Figure 4-6 displays the powder x-ray diffraction patterns around the (220)$_d$ fundamental peak position of samples isothermally treated at 280°C, 310°C and 330°C. The x-ray pattern of a sample treated at 250°C is put as reference of the microstructural state that does not show splitting.

It is observed that the splitted peaks shift outwards with increasing ageing temperature, as indicated by the black arrows in Figure 4-6. However, the sample isothermally aged at 310°C for 20 minutes shows the more striking feature: the right-side splitted peak contains an *additional* peak. Then, careful examination of the splitted peaks of the sample aged at 330°C during 1h also reveals also an *additional* peak on the right-side splitted peak; in this case, the *additional* peak exhibits greater intensity as the splitted peak. Finally, the sample treated at 330°C during 12h, which is known to be close to fully ordered, shows the (202)$_o$ peak at roughly the same position as the *additional* peak. The same behaviour is observed on the evolution of the (200)$_d$ peak with increasing ageing temperature, see Figure 4-7, most notably on the right split peak. It is therefore assumed that the additional peak corresponds to the L1$_0$ phase with c/a=0.92, i.e. strain-free.
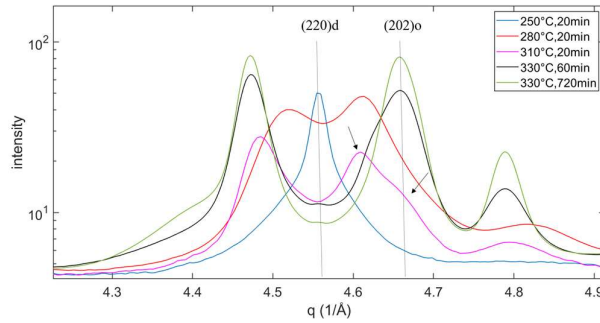
Figure 4-6 Powder diffraction patterns of red gold isothermally aged at various temperatures and times.
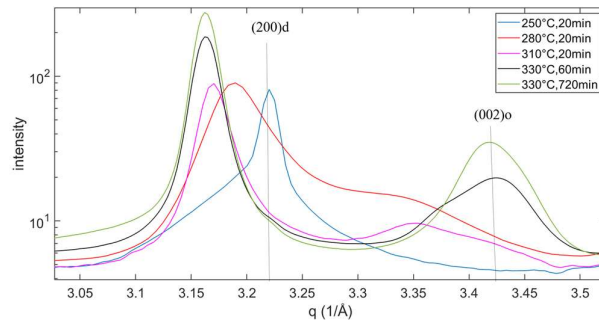
Figure 4-7 Powder diffraction patterns of red gold isothermally aged at various temperatures and times.

A possible explanation for the observed peak split on the $(200)_d$ and $(220)_d$ could be that, indeed, they corresponded to the $L1_0$ phase, i.e. the $(200)_o$, $(002)_o$, $(220)_o$ and $(202)_o$ peaks. The increasing split distance between the peaks would be explained by the increasing tetragonality (c/a) with increasing ordering. The same happens with the superlattice reflections, which exhibit a continuous shift from a c/a≈1 (note that the ordered domains are coherent with the cubic matrix) towards the equilibrium c/a=0.92 of the $L1_0$ phase (this will be discussed in the next section).

To proof that, the X-ray diffraction patterns of the isothermally aged samples were fitted to a $L1_0$ phase, in particular the $(001)_o$, $(110)_o$, $(201)_o$, $(112)_o$, $(221)_o$ and $(310)_o$ superlattice peaks and the $(111)_o$, $(200)_o$, $(002)_o$, $(220)_o$ and $(202)_o$ fundamental peaks. Interestingly, no solution fitted both the superlattice and fundamental peaks in any sample. While the superlattice peaks could be fitted to a $L1_0$ phase with c/a between 1 and 0.92, depending on the sample. The fundamental peaks could not be fitted to a $L1_0$ phase and, of course, not to a cubic phase. Figure 4-8 displays the x-ray diffraction pattern of sample 280°C, 20 minutes with an overlay of the expected peak positions calculated from the $L1_0$ lattice parameters that fit the superlattice reflections of the X-ray pattern. Red lines indicate the peaks where a big mismatch is observed.
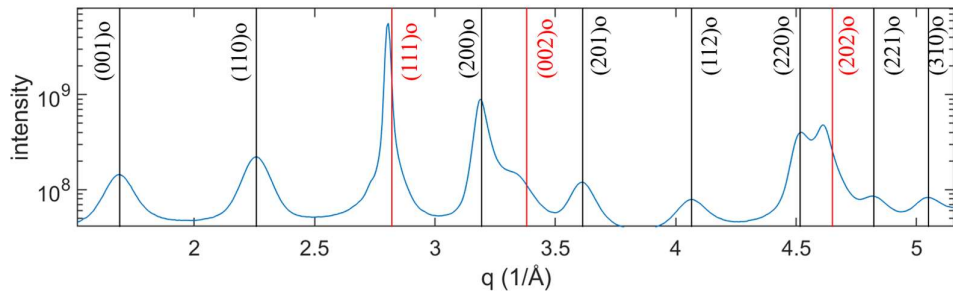
Figure 4-8 Powder diffraction pattern after isothermal ageing at 280C during 20 minutes overlayed with vertical lines that define the peak positions of the L1$_0$ phase according to the fitted superlattice reflections.

From Figure 4-8, it is clear that the (111), (002) and (202) fundamental reflections do not fit the L1$_0$ phase. This indicates that the coherency between the ordered domains and the disordered matrix induces strong elastic distortions that affect both phases and most notably the (200) and (220) fundamental peaks.

Microstructural TEM investigations were carried out after isothermal ageing at 250°C-20min, 280°C-20 min and 310°C-20 min. TEM BF and DF images of the respective samples are shown in Figure 4-9, together with the electron diffraction pattern of the DF image . TEM BF images in Figure 4-9a-c reveal a cross-hatched contrast which becomes coarser with increasing ageing temperature. The DF images in Figure 4-9d-f are taken along the [110] zone axis on the (001) superlattice reflection, where the white contrast of the image corresponds to the ordered domains. There is a clear evolution in the arrangement of the ordered domains with increasing ageing temperature. A fine tweed structure is observed after ageing at 250°C, which evolves into a coarser a tweed at 280°C and seem to develop some twins [51] at 310°C. The electron diffraction patterns, see Figure 4-9g-I, show increasing intensity in the superlattice spots, in accordance with the increasing ordering degree achieved after isothermal ageing at higher temperatures.

250⁰C, 20 min **280⁰C, 20 min** **310⁰C, 20 min**
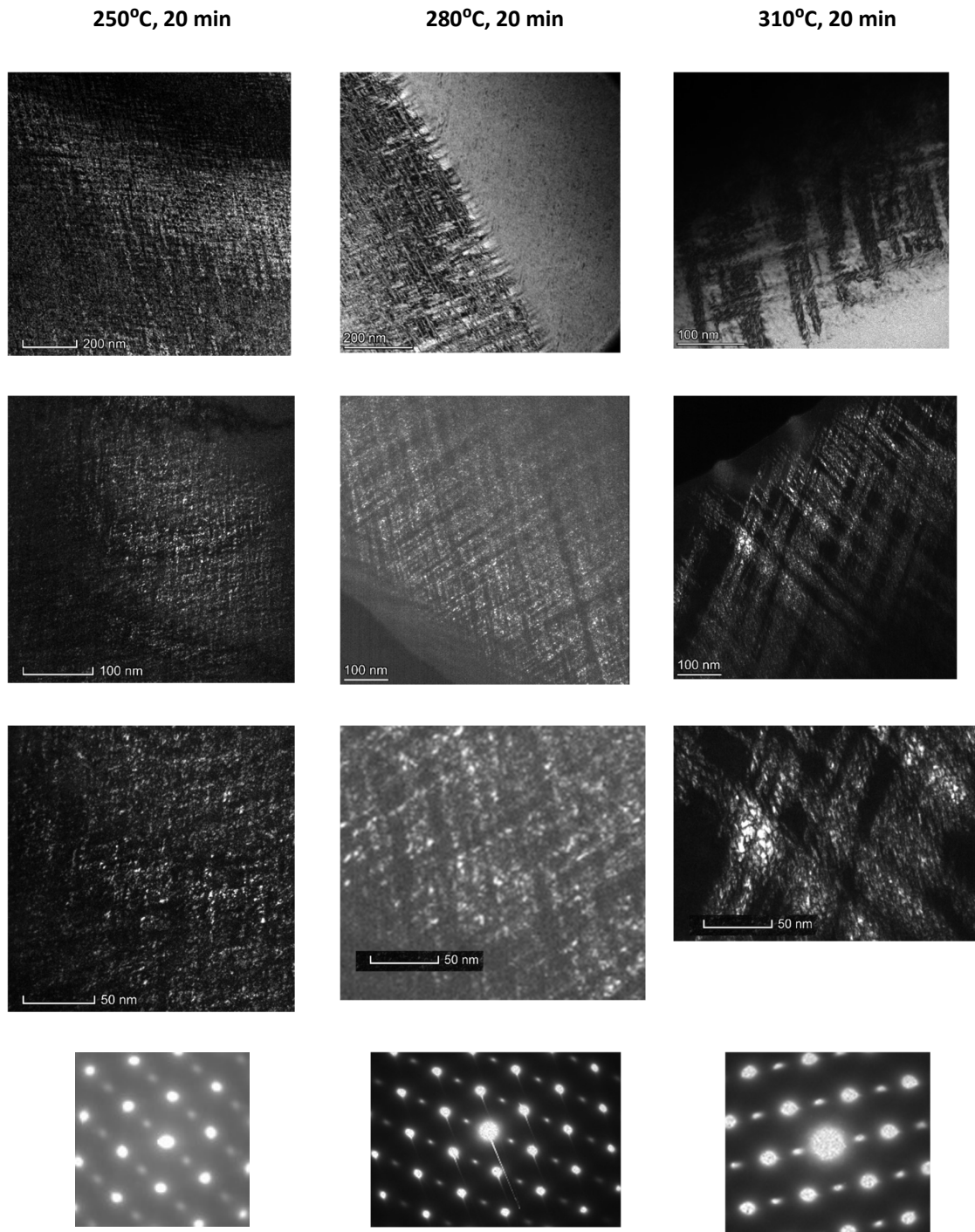
Figure 4-9 TEM DF images along the (001) superlattice spot along the [110] zone axis. a,d) sample treated at 250⁰C, 20min, b,e) sample treated at 280⁰C, 20min, c,f) sample treated at 310⁰C, 20min, g,h,i) electron diffraction patterns along the [110] zone axis

The correlation of the X-ray features with the microstructures observed in TEM result in three stages of ordering that are identified are summarized in Table 4-1. Note that the microstructural features of Stage I were already introduced in section 4.1.2.

Table 4-1 Correlation of the observed X-ray features with the microstructures revealed by TEM

Condition	Stage of ordering	TEM microstructure	X-ray feature
After cooling	Stage I	Dense, homogeneous and fine dispersion of coherent ordered and nano-sized domains within the disordered grains Eventually, <110> streaking fundamental spots.	(110) diffuse maxima Broad and low intensity super-lattice reflections
$250^{\circ}C$, 20min	Stage II	Tweed	Broadening of $(200)_d$ and $(220)_d$ fundamental peaks
$280^{\circ}C$, 20min		Coarse Tweed	Splitting of the $(200)_d$ and $(220)_d$ fundamental peaks
$310^{\circ}C$, 20min	Stage III	Twin (Microtwinning according to [51])	Presence of $(200)_o$, $(002)_o$, $(220)_o$ and $(202)_o$ fundamental peaks at $c/a \square 0.92$
$330^{\circ}C$, 12h	Stage IV	Twin (Macro-twinning according to [51])	Presence of $(200)_o$, $(002)_o$, $(220)_o$ and $(202)_o$ fundamental peaks at $c/a=0.92$

4.2.2. Distortion of the $L1_0$ phase

Figure 4-10 compares the evolution of the $(001)_o$ and $(110)_o$ after 20 minutes ageing at $150^{\circ}C$, $200^{\circ}C$ and $280^{\circ}C$. The continuous shift of the $(001)_o$ super-lattice towards greater q-values translates into smaller inter-planar spacings. Opposite behaviour is observed for the $(110)_o$ peak. This indicates that the interplanar distance between chemically ordered planes becomes smaller along the c-axis and larger along the a-axis of the ordered unit cell. Note that the $(110)_o$ peak for the sample heat treated at $150^{\circ}C$ during 20minutes displays a peak shape in-between the two broad maxima and a single peak, this peak shape probably corresponds to the transition between stage I and II.
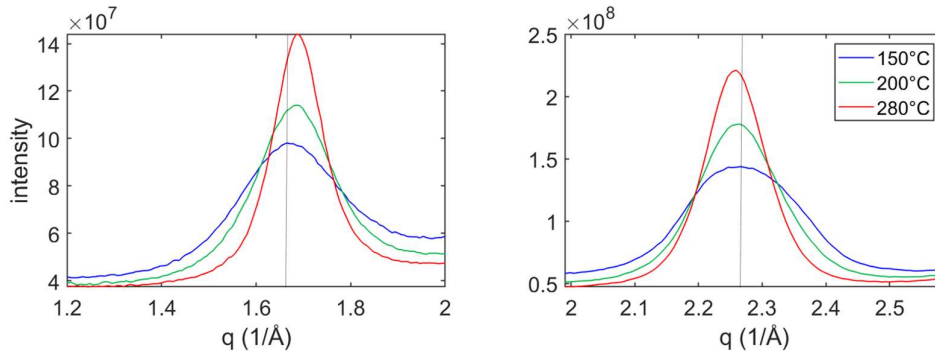
Figure 4-10 Diffraction peaks after isothermal ageing during 20 minutes at 150°C, 200°C and 280°C. a) (001) super-lattice peak and b) (110) super-lattice peak

Single-peak fitting of the super-lattice reflections (001), (110), (201) and (112) determines the peak position thus the inter-planar spacing of super-lattice planes. From this, the L1$_0$ lattice *a*- and *c*- parameters can be calculated by solving Eq 2 and Eq 3 for the pair of planes (001) / (110) and (201) / (112).

Equation 4-1 Relationship scattering vector and interplanar spacing

$$d_{hkl} = \frac{2\pi}{q_{hkl}}$$

Equation 4-2 Calculation of the interplanar spacing of the lattice cell

$$\frac{1}{d_{hkl}^2} = \frac{h^2 + k^2}{a^2} + \frac{l^2}{c^2}$$

Figure 4-11 shows, for each ageing treatment, the *a*- and *c*- lattice parameters obtained for each set of planes. Starred markers correspond to the set (001)/(110) while open circles correspond to the (201)/(112) set.
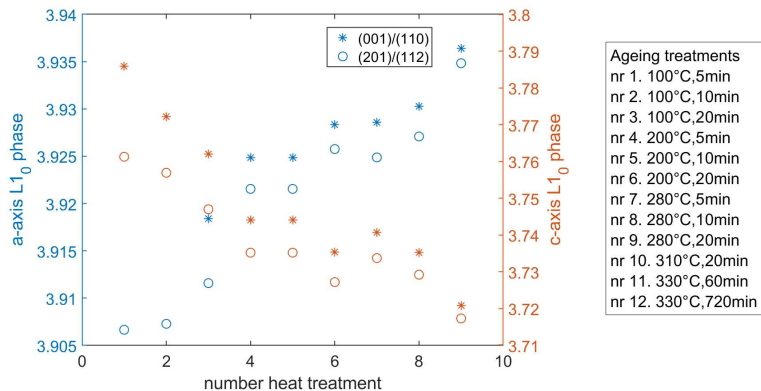
Figure 4-11 a- and c- lattice parameters of the L10 phase as a function of isothermal ageing treatments. Starred markers correspond to the values obtaiend from (001)/(110) plane pair. Open circles correspond to the values obained from the (201)/(112) pair of planes

There is a clear disparity on a- and c- values obtained from each set of planes. The (001)/(110) set of planes results in greater a- and c- parameters, as compared to the ones from the (201)/(112) set of

planes. With increasing time and treatment, the disparity is reduced. This suggets that at the early stages of ordering, the ordered unit cell is distorted and does not fully correspond to a $L1_0$ structure. With prolonged ageing time and increasing temperature, ordering advances and the ordered lattice relaxes towards the $L1_0$ structure (e.g. 280C, 20min).

The c/a ratio characterizes the tetragonality of the $L1_0$ phase. Figure 12 shows, for each ageing treatment, the c/a ratio obtained from the (001)/(110) pair (blue open circles) and (201)/(1120) pair (black open circles). For treatments nr. 1 and 2 the c/a ratio of the (001)/(110) pair is not calculated because the (110) peak shows the two broad maxima instead of a single peak.
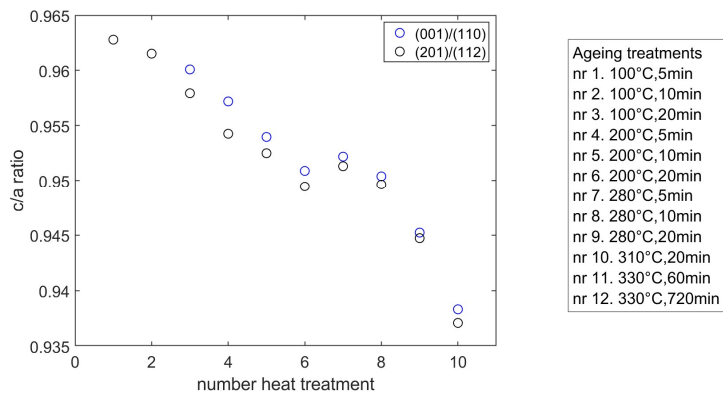
Figure 4-12 Evolution of the c/a ratio as a function of isothermal ageing treatments.Ageing treatments at 200°C (thermal treatments nr. 4, 5 and 6 indicated by vertical lines

Figure 4-12 show that increasing ageing time reduce both the c/a value and the dispersion between the (001)/(110) and (201)/(112), suggesting that the growth of the ordered domains is accompanied by a reduction in the distortion of the ordered lattice. This agrees with DF TEM observations on the (001) superlattice along the [110] zone axis, see Figure 4-9g-i, that show the increasing domain size with increasing ageing temperature, i.e. treatments at 250°C-20 min, 280°C-20min and 310°C-20min. Domain size measurements on the TEM DF images reveal average domain sizes of 5nm in the sample aged at 280°C during 20minutes.

Ageing at high temperature for less time (e.g. 280°C, 5 minutes) shows a greater c/a ratio but less dispersion as compared to lower ageing temperature for longer times (e.g. 200°C, 20minute). This is thought to be related to the ordering rate. Ageing at higher temperature will result in a faster ordering rate. A faster ordering rate results in a fast increase of the internal strain, and therefore triggering microstructural strain relief mechanisms, which relax both the disordered matrix and the ordered domains.

Figure 4-13 Williamson-Hall plot of the (001),(110),(201) and (112) super-lattice reflections for all the ageing treatments.shows the Williamson-Hall plot analysis on the super-lattice reflections for all the

ageing treatments. Ageing treatments at moderate temperatures and/or short durations (e.g. 150°C 5-20min, 200°C 5-20min and 280°C 5-10min) show a Williamson-Hall plot with a negative slope. For the treatments at higher temperatures, such as 280°C - 20min, 310°C-20min, 330°C-1h and 330°C-12h, the Williamson hall plot shows a shallow U-shape.
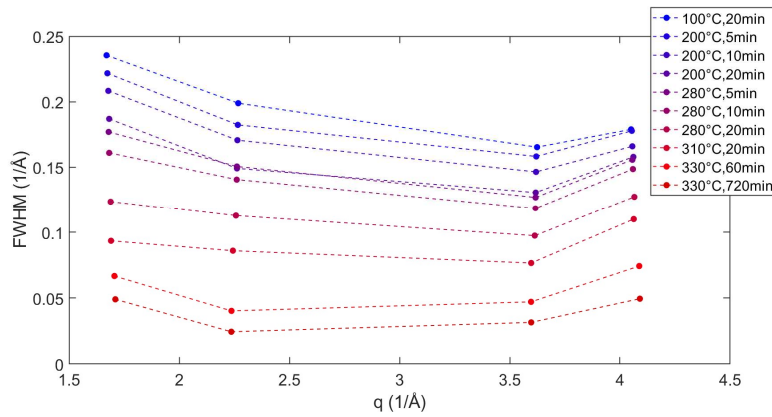
Figure 4-13 Williamson-Hall plot of the (001),(110),(201) and (112) super-lattice reflections for all the ageing treatments.

The observed tendencies of the FWHM with q do not follow the expected evolution of the peak breadth as a function of the reciprocal vector for an isotropic lattice with nano-sized crystallites and micro-strain. An isotropic system with nano-sized crystallites and no micro-strain shows a constant peak broadening as a function of the recriprocal vector (q). Additional strain gradients within the crystallites results in additional peak broadening, which increases with the reciprocal vector (q).

Elastic anisotropy (Au and Cu are highly anisotropic elements [138]) and/or the morphology of the ordered domains (e.g. a platelet vs. sphere) can be responsible for deviations from the ideal Williamson-Hall plot. In this case, micro-strain anisotropy and morphological effects cannot be excluded. The absence of micro-strain models on the precipitate during ordering makes it impossible to separate the crystallite size contribution from the micro-strain contribution.

The fact that the FWHM is reduced with increasing treatment time and temperature indicates that the ordered domains grow and/or relax. In particular, the nearly fully ordered sample (330°C-12h), which showed a nanotwinned structure and a L1$_0$ structure with c/a=0.92, can be assumed to be fully relaxed. Thus the difference in the peak breadths of this sample will be mainly dominated by shape anisotropy.Indeed, the crystallographic directions sensitive to the c-axis, i.e. (001) and (112), show broader peaks that suggest a platelet morphology with the shorter direction along the c-axis.

In a first approximation, it can be assumed that the peak breadth variations are solely due to the anisotropic morphology of the ordered domains and not to micro-strain. Then, the application of the Scherrer equation to each peak can estimate the crystallite size evolution along the crystalographic

directions [001], [110], [201] and [112], as shown in Figure 4-14. The obtained crystallite values can be considered as a lower limit for the size of the domains, in case microstrain is present. Moreover, as previously mentioned, domain size measurements in TEM DF images reveal average domain sizes around 2nm and 5nm for sample 550R-s and isothermally treated at 280^oC-20min, respectively, indicating that peak width is mainly related to grain size.
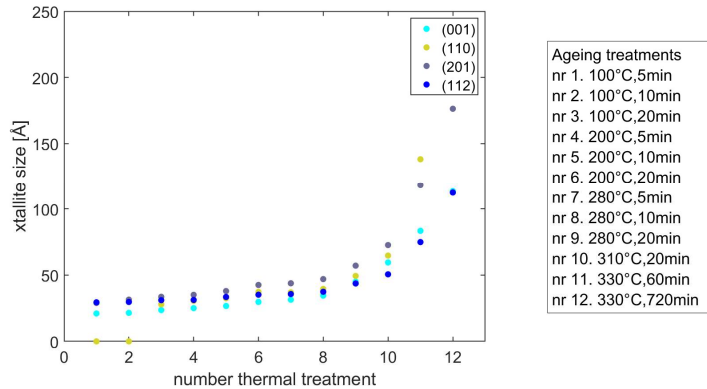
Figure 4-14 Crystallite size for the (001),(110),(201) and (112) superlattice reflections, obtained from the Scherrer equation.

Following the previous argument, from Figure 4-14 it observed that ageing treatments at 330^oC for 1h and 12h show a clear crystallite size anisotropy along the [110] and [001] directions. This suggests a plate-like morphology of 11 x 16 nm. The smallest dimension equal to 11nm corresponds to the [001] direction. The largest direction equal to 16nm corresponds to the crystallite size along the [100] direction, which is equal to the proyection of the [110] crystallite size along the [100] direction, which makes 23 nm divided by $\sqrt{2}$.

4.3. Natural ageing on samples processed in industry

4.3.1. Influence of cooling rate

Recrystallization heat treatments in industrial continuous furnaces are done with milder cooling rates as compared to water quenches, see Figure 3-1 in chapter 1. Figure 4-15 compares the powder diffraction patterns of samples recrystallized in quench furnaces and continuous cooling furnaces and naturally aged during 7 days.

Firstly, every cooled sample shows overlapping fundamental reflections indicating coherency between the ordered phase and the disordered matrix. Secondly, two diffuse maxima are observed around the $(110)_o$ peak position, indicating a stage I microstructure.
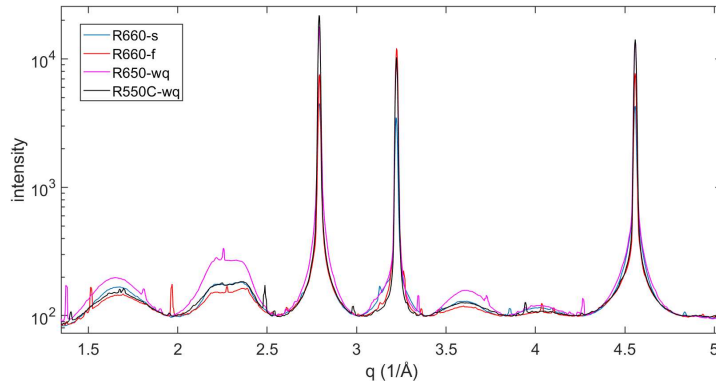
Figure 4-15 Powder diffraction pattern of various red gold samples after cooling

The quenched-in excess vacancy density is expected to be greater in the water-quenched samples compared to the continuoulsy cooled samples. Particularly, the sample quenched from 660°C will exhibit a higher density of excess vacancies compared to the one quenched from 550°C. Indeed, after natural ageing, the samples displaying a greater integrated intensity in the superlattice reflections are the water quenched ones. It is noted that the diffraction patterns of the sample *red 660slow cc* and the sample *red 550C wq* show a very similar diffraction pattern.

Furthermore, the sample red *660fast cc* shows lower superlattice intensity as compared to the sample *red 660slow cc*. This suggests that the quenched-in excess vacancies upon the fast cooling rate on the continuous cooling furnace are not large enough to promote ordering at room temperature.

4.3.2. Influence of cooling rate and plastic deformation

The influence of cooling rate and plastic deformation on natural ageing was examined on the industrially processed samples displayed in Table 4-2. Samples 660R-s and 550R-s are recrystallized on a continuous furnace with a characteristic slow cooling rate. While 550R-f and 660R-f were recrystallized in a continuous furnace with a faster cooling rate. After recrystallization, every sample is subsequently restraightened (660RS-s, 550RS-s, 660RS-f and 660RS-s) and naturally aged during 7 days. Line scans across the 2mm thickness of the samples were performed. *Ex situ* high-energy X-ray powder diffraction line scans were performed accross the 2mm thickness each sample.

Table 4-2 Overview of processing parameters for ex situ samples (C_r = cooling rate). The nomenclature is defined as follows: xxxR = recrystallization temperature, S = straightened, f, s = fast or slow cooling.

Nomenclature	T_r (°C)	C_r (°C/min)	Straightened	Grain size (µm)
660R-f	660	-800	-	13
60R-s	660	-100	-	30
660RS-f	660	-800	✓	13

660RS-s	660	-100	✓		30
550R-f	660	-800	✓	-	8
550R-s	660	-100	✓	-	8
550RS-f	660	-800	✓		8
550RS-s	660	-100	✓		8

Firstly, the samples 660R-s, 660R-f, 660RS-s and 660RS-f are examined, then a comment on samples 550R-s, 550R-f, 550RS-s and 550RS-f will follow.

Plastic deformation induced by the wire straightening operation increases the peak broadening of all fundamental diffraction peaks, as illustrated for the (311) fundamental peak in Figure 4-16a-b for the line scans performed on the samples 660R-s, 660RS-s, 660R-f and 660RS-f. The alloy grain size is too large to contribute to the peak broadening. It should be noted that the (311) peak might comprise contributions of both phases. However, the intensity of the ordered phase is very small and can therefore be ignored. As a result, we can assume that the peak broadening is directly related to inhomogeneous elastic strains in the disordered matrix.
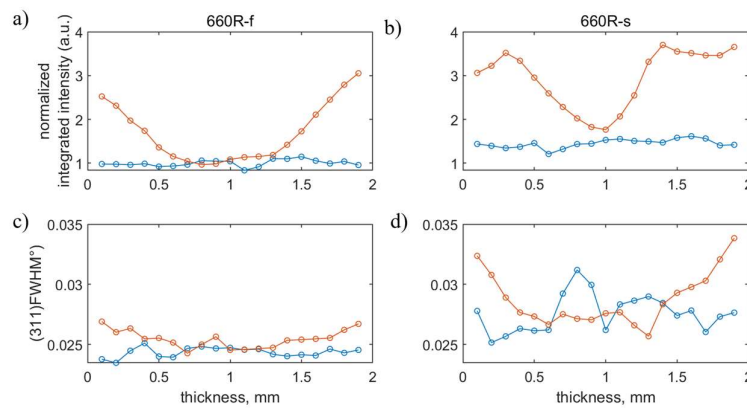
Figure 4-16 Evolution of the FWHM of the 311 peak along the thickness of samples a) 660R-f and 660RS-f and b) 660R-s and 660RS-s. Evolution of the normalized (110) integrated intensity alogn the thickness of the sample c) 660R-f and 660RS-f and d) 660R-s and 660RS-s.

For the non-straightened samples the FWHM of (311) is expected to be independent on the position within the samples. This is the case of 660R-f. The FWHM for 660R-s exhibits a lot of scatter, which can be ascribed to a lack in grain statistics. This sample had been exposed longer to high temperature than 660R-f, leading to larger grain sizes. This is also confirmed by the 2D patterns of 660R-s (see Figure 4-17a) , which do not exhibit full diffraction rings from the disordered phase; in contrast, they are rather spotty and the intensities vary strongly when scanning across the thickness. The rings of the superlattice peaks however are continuous in all samples, see Figure 4-17a-b Furthermore, the line scan of sample 660R-s was repeated by slightly wiggling the sample up and down in the direction

perpendicular to the thickness with the aim of probing more grains. The resulting FHWHM of (311) was independent of the position within the sample, as expected.
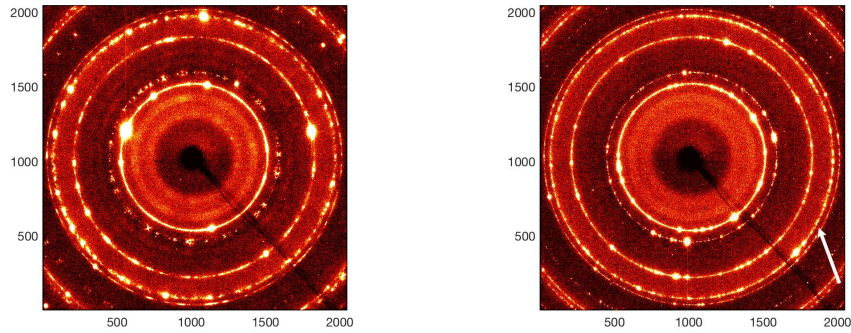
Figure 4-17 2D diffraction pattern of sample upper) 660R-s and lower) 660R-f

The straightening is reflected by a small increase in the FWHM near the surface in all samples. Figure 4-16c-d compare the integrated intensities of the (110) superlattice reflection of the $L1_0$ phase. Similar profiles are obtained for other superlattice reflections. The intensities are normalized to the average value for sample 660R-f. The recrystallized samples without straightening (660R-s,f) show as expected the presence of homogeneously distributed ordered precipitates. The averaged intensity is slightly higher in 660R-s then in 660R-f. After straightening, the integrated intensity is clearly higher near the surface of the samples, suggesting differences in distribution and/or sizes of ordered precipitates. The profiles are quite different for fast and slow cooling rates. Where there is a clear correlation between the integrated intensity and the FWHM for the fast cooled samples, this is not the case for the slowly cooled samples. Here, the maximum integrated intensity is reached below the surface. Since the industrial wire straightening process is carried out on a wavy wire, varying levels of plastic deformation along the length of the wire are to be expected and therefore, the exact shape of the profiles shown in Figure 4-16c and 4-16d may not be directly comparable.

Finally, the same tendencies are observed in samples previously recrystallized at 550°C, i.e. 550R-s, 550R-s, 550RS-s and 550RS-f, as shown in Figure 4-18.
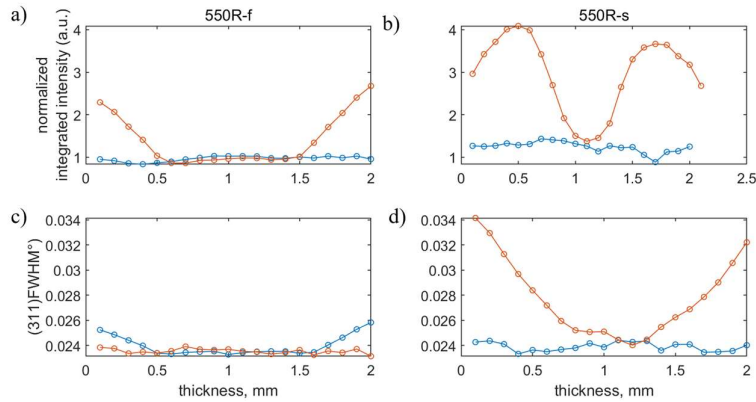
Figure 4-18 Evolution of the FWHM of the 311 peak along the thickness of samples a) 550R-f and 550RS-f and b) 550R-s and 550RS-s. Evolution of the normalized (110) integrated intensity alogn the thickness of the sample c) 550R-f and 550RS-f and d) 550R-s and 550RS-s.

4.4. Isothermal ageing: influence of thermo-mechanical history

Artificial isothermal ageing treatments were applied on two types of samples. Firstly, on samples that were previously thermo-mechanically processed in industry. Secondly, the ordering transformation will be followed *in situ* during the ordering transformation on samples were the initial microstructure (cooling rate and plastic deformation) is controlled under laboratory conditions.

4.4.1. Industrial thermo-mechanical processing

Figure 4-19 shows the powder X-ray diffraction patterns of straighened wires isothermally aged at different temperatures for a fixed duration of 20 minutes. Isothermal ageing at 150°C and 250°C confirm that previous plastic deformation enhances ordering.

At low temperatures, the more advanced ordering is observed at the surface region, as indicated by the more intense super-lattice reflections and slight intensity increase on the $(200)_d$ and $(220)_d$ fundamental peaks. After ageing at 250°C, the surface region clearly shows peak splitting around the fundamental $(200)_d$ and $(220)_d$ peaks as opposed to the center of the sample. Finally, heat treating at 330°C for 1h reveals a very similar ordered state between the surface region and the center. The ordering transformation is however not complete, as shown by the shape of the (111) peak, which results from the overlap of the $(111)_{\alpha2}$, $(111)_d$ and $(111)_o$.

These observations suggest that the ordering rate in the plastically deformed regions is faster at low temperatures. When the ageing temperature is close to the critical temperature for ordering, e.g. 330°C, the deformed and undeformed regions show a very similar final microstructure.

96
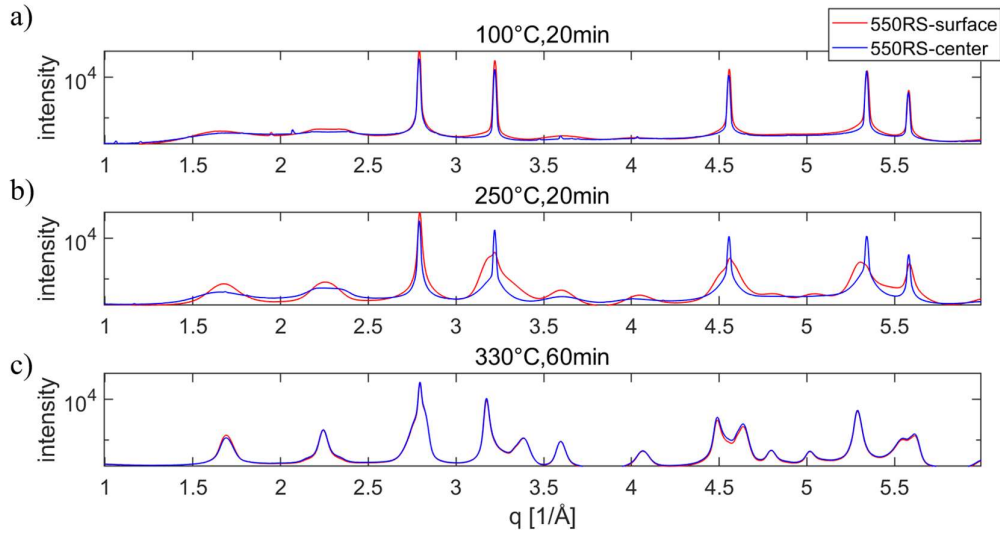
Figure 4-19 Powder x-ray diffraction patterns at the center and at the surface of straightened wires. a) isothermal ageing at 100C during 20 min, b) isothermal ageing at 250C during 20min and c) isothermal ageing at 330C during 1h.

4.4.2. Laboratory-scale controlled thermo-mechanical processing

In situ isothermal ageing experiments

To verify whether dislocations also play a role in enhancing ordering during artificial ageing, four *in situ* diffraction experiments were performed. First, all 4 samples are heated to 660°C with a fixed heating rate of 100°C/min and kept there for 2min to ensure a complete dissolution of the $L1_0$ precipitates, followed by controlled cooling to room temperature with cooling rates of -100°C/min and -800°C/min. Two of the samples were then cold rolled to a thickness reduction of 25% using a Cooks rolling mill 999 AXWA. Finally, all 4 samples are subjected to a 20min ageing treatment at 250°C. It should be noted that the cold rolling process induces a much higher degree of plastic deformation as compared to the wire straightening process. This is evidenced in Figure 4-20, which compares the changes of the FWHM of the (311) diffraction peak between the cold rolling and wire straightening process.
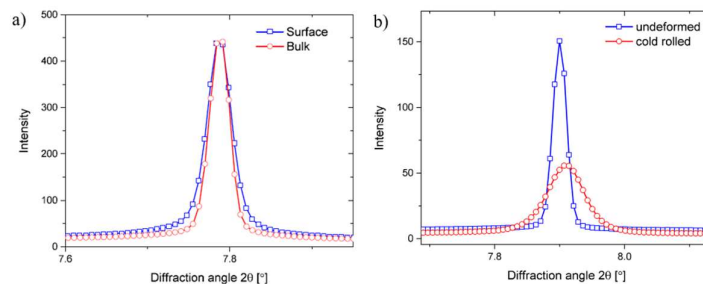
Figure 4-20 Comparison of the FWHM change of the (311) diffraction peak between the cold rolled sample and the straightened sample.

97

Figure 4-21a shows the evolution of the integrated intensity of the (110) superlattice reflection together with the temperature profiles (dashed black lines) starting from the recrystallization temperature (660°C). The intensities are normalized to the intensity obtained at room temperature after fast cooling. During cooling, precipitates start forming below 360°C. Below 200°C the ordering kinetics slows down and a plateau is reached. At room temperature, the integrated intensity after slow cooling is more than twice that after fast cooling. After room temperature is reached, the temperature is raised again to the ageing temperature at 250°C. During this period, the integrated intensity raises much faster in the deformed samples than in the undeformed samples. In the deformed samples ordering becomes visible around 100°C whereas in the non-deformed samples a raise is only observed close to 250°C. This is evidenced in Figure 4-21b, showing the evolution of the integrated intensities during heating from room temperature to the ageing temperature (250°C). After the ageing temperature of 250°C is reached (corresponding to time zero in Fig 18a), the difference between the integrated intensity of the deformed and the undeformed sample further increases. However towards the end of the ageing, the difference seems to remain constant. In other words, cold rolling prior to ageing increases the rate of ordering at the early stages

The integrated intensity is proportional to the volume fraction of the precipitates and therefore cannot discriminate between growth or nucleation. Further information can be obtained by considering the evolution of elastic strain in the precipitates. Figure 4-21c and Figure 4-21d show the evolution of the change of the interplanar spacing of the (201) and (112) superlattice reflection relative to their value prior to heating for the slowly cooled undeformed and deformed sample, respectively. During initial heating to the ageing temperature the lattice expands, thereby increasing the interplanar spacing. From this we can derive a thermal expansion coefficient of 16×10^{-6} C^{-1}, in agreement with the value reported in [139]. The same value is obtained during cooling down after 20min ageing. After reaching the ageing temperature of 250°C the interplanar spacings of the (201) and (112) peak of the undeformed sample change significantly and in opposite direction. For the deformed sample deviation from thermal expansion starts already at 150°C. It has been shown that during early stages of ordering the precipitates are fully coherent with the matrix and are under tension along the c-axis and compressed along the a-axes, in agreement with [51,77]. During precipitate growth the unit cell parameters approach those of the constraint-free AuCu-I phase [51]. This results in an expansion and contraction of the (201) and (122) interplanar spacings, respectively. With other words, the evolution of lattice expansion in Figure 4-21b and Figure 4-21c demonstrate that in the deformed sample the precipitates start to grow at a lower temperature as compared to the undeformed sample.
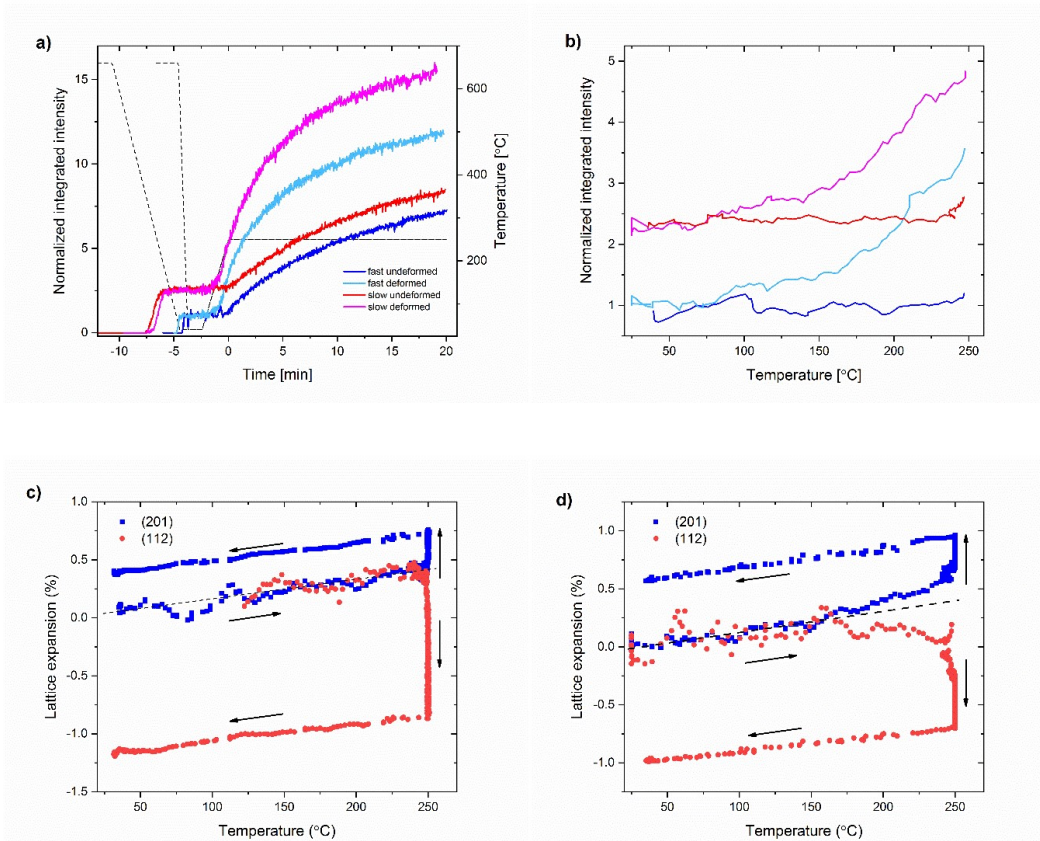
Figure 4-21 a-b) Evolution of the integrated intensity of the (110) diffraction peak during a thermal cycle, which is comprised of slow or fast cooling from 660°C followed by aging at 250°C with and without mechanical deformation in between. a) shows the temperature profile (dashed lines) and integrated intensities (full lines) as a function of time, b) displays the integrated intensity during heating up to the ageing temperature (250°C). c) Evolution of the peak position of the (201) and (112) diffraction peaks during the thermal cycle in the undeformed sample (slowly cooled). d) Evolution of the peak position of the (201) and (112) diffraction peaks during thermal cycle in the deformed sample (slowly cooled). The black arrows indicate the heating and cooling sections.

Post-mortem TEM studies reveal different ordered microstructures in the undeformed and deformed samples. Figure 4-23 compare TEM dark field images based on the (001) superlattice reflection along the [110] zone axis of respectively the undeformed and deformed sample after ageing, at various magnifications. The undeformed sample exhibits a fine tweed structure, whereas in the deformed sample shows a more heterogeneous and coarser tweed structure., indicative of a more advance ordered state. Examination of the x-ray powder diffraction patterns confirm that the deformed sample, which showed a faster ordering rate, shows a more advanced split around the $(200)_d$ and $(220)_d$ peaks, see Figure 4-22 a-b. These results agree with the observations of section 1.1. In ordert to gain insights on the role of dislocations during chemical ordering, it was interesting to investigate whether the ordered domains preferentially nucleate/grow in the core or ends of the dislocation. Unfortunately, it was not possible to observe the ordered domains at the film thickness where

dislocations were observed (around 100nm thick) due to the low intensity signal of the ordered domains.

In summary, these experiments reveal that plastic deformation enhances the ordering rate at low temperatures and suggesting an earlier growth of the ordered domains. The enhanced ordering rate of the deformed samples results in an ordered microstructure at an advaced stage II (coarse tweed), as compared to the undeformed sample, which is at the beginning of stage II (fine tweed).
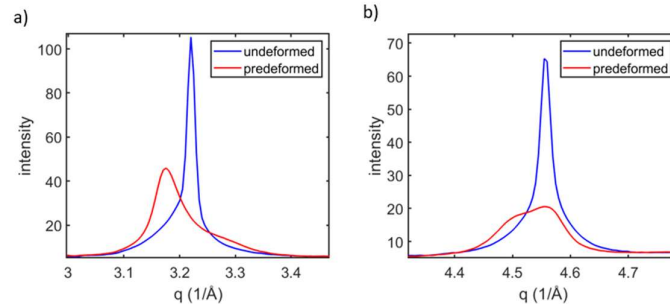
Figure 4-22 Deformed and undeformed isothermally aged samples at 250°C during 20 minutues. a) $(200)_d$ peaks and b) $(220)_d$ peaks

250ºC, 20 min undeformed   **250ºC, 20 min deformed**
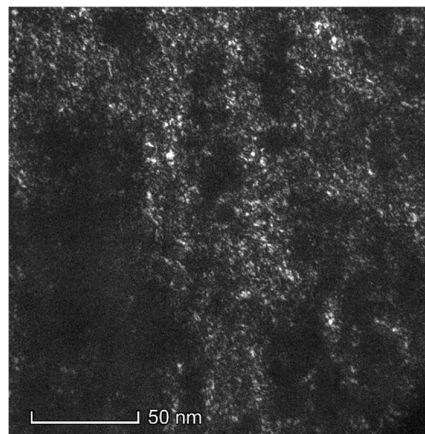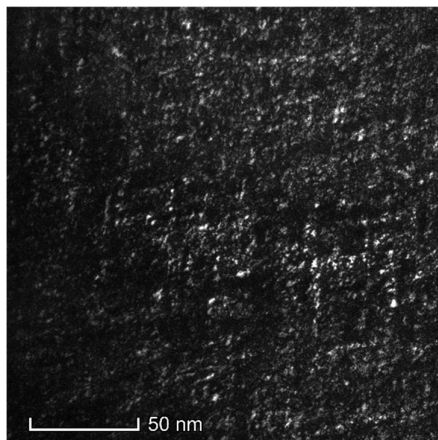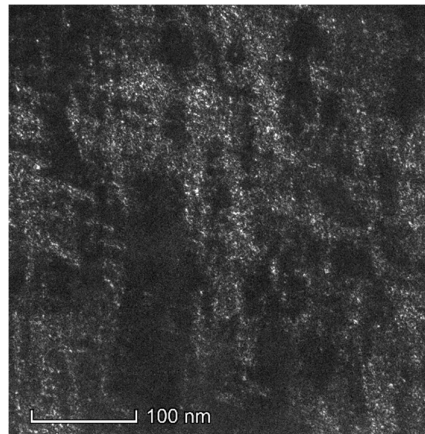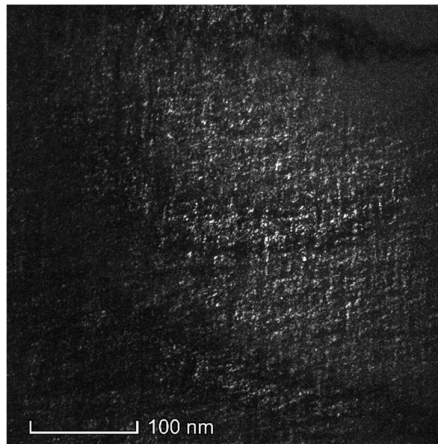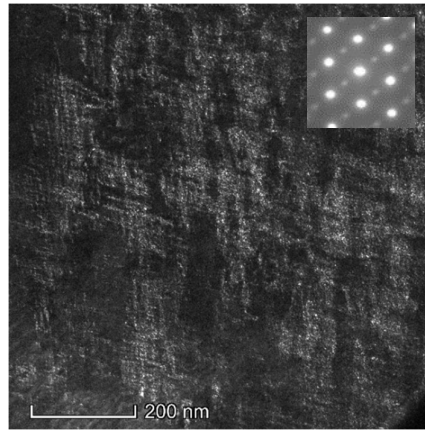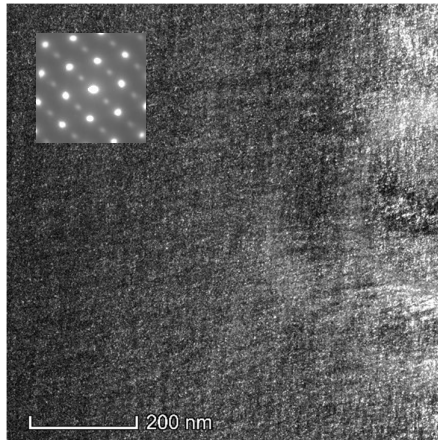
Figure 4-23 a-b) Dark field TEM images based on the (1-11) super-lattice reflection along the <110> zone axis after 20min ageing, a) without and b) with prior deformatio

Chapter 5   In situ heating experiments

Two series of 18 karat red gold alloys were investigated with nominal composition Au75-Cu20.5-Ag5.6 and $Au_{75}(Cu\text{-}Ag)_{(1\text{-}x\text{-}y)}Pd_xSn_y$, with 0.1<x<1.1 and 0.1<y<2.1 in weight percent. In what follows they are denominated red gold (R) and modified red gold (MR), respectively.

Section 1 compares experimental the microstructures obtained after cooling and after isothermal ageing.

Section 2 presents the *in situ* heating experiments on red gold (R) as a function of thermo-mechanical history under controlled laboratory conditions, i.e. treatment temperature, cooling rate and predeformation.

Section 3 presents the in situ heating experiments on modified red gold (MR) as a function of thermos-mechanical history under controlled laboratory conditions, i.e. cooling rate and predeformation.

Table 5-1 provides an overview of all samples that were used for the in situ experiments.

Table 5-1 Overview of the samples with processing parameters

Alloy	Cooling rate (^oC/min)	Pre-deformed	Nomenclature
Red gold	-100	-	R-slow
Red gold	-800	-	R-fast
Red gold	-100	✓	R-slow-def
Red gold	-100	✓	R-fast-def
Modified red gold	-800	-	MR-slow
Modified red gold	-100	✓	MR-slow-def
Modified red gold	-800	✓	MR-fast-def

5.1. Microstructure after cooling and after ageing

Figure 5-1a displays an inverse pole figure of the cross-section of an as-received wire, which is representative for all samples. The colour code corresponds to the stereographic projection of the crystal directions parallel to the normal direction (ND). The sample exhibits equiaxed grains with a number averaged grain size diameter of 8µm and very mild texture. TEM examinations reveal a very fine dispersion of ordered domains within the disordered grains as shown by the white dots on the dark field image along the <110> axis of Figure 5-1b. Figure 5-1c displays a diffraction pattern along the [001] zone axis. The white arrows indicate the presence of diffuse superlattice reflections belonging to the three different $L1_0$ orientational variants.

High-resolution TEM investigations confirm the presence of extremely fine ordered domains, composed of a few atomic planes. Figure 5-1d shows the inverse fast Fourier transform (IFFT) from the superlattice reflections, indicated by black arrows on the diffraction pattern shown in the inset. The regions of the IFFT image with stronger contrast correspond to the ordered domains. In this case, the X- and Y- orientational variants are observed within one grain, with sizes below 2nm. There is no clear interface between the disordered matrix and the ordered domains.

Figure. 5-2a compares the X-ray diffraction patterns of R-slow and R-fast immediately after cooling (blue curve) with a sample that was aged at 330°C for 12h (red curve). The latter corresponds to a nearly fully ordered sample with a long-range order parameter S=0.92. The selected fundamental and superlattice reflections for the calculation of the s parameter correspond to the {220} and (110), respectively.
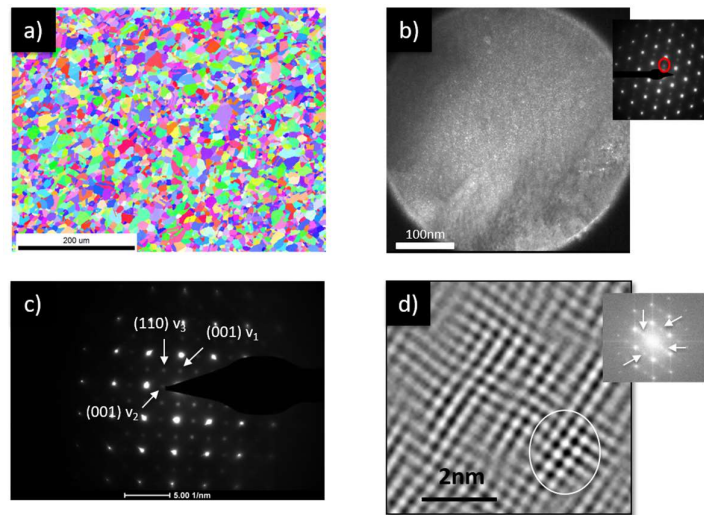
Figure 5-1 As-received microstructure. a) Inverse pole figure, b) TEM DF on the (001) along the [110] zone axis, the (001) super-lattice reflection is highlighted by a red circle on the diffraction pattern, c) TEM electron diffraction pattern along the [100] zone axis, d) IFFT of an HRTEM image taken along the [110] zone axis. The IFFT corresponds to the superlattice reflections indicated by white arrows in the FFT shown as an inset.

After cooling the microstructure exhibits a chemically disordered FCC phase that coexists with a minor $L1_0$ phase, as evidenced by the low intensity, broad superlattice reflections. This is in agreement with the TEM observations shown in Figure 5-1b. Note that the fundamental x-ray diffraction peaks of the ordered phase are not visible because they completely overlap with the fundamental peaks of the disordered matrix. After ageing, the sample is fully ordered and exhibits the typical $L1_0$ diffraction pattern, with splitting of the fundamental peaks such as, for instance, the $(220)_o$ and $(022)_o$. The experimental lattice parameters correspond to a=3.97Å and c=3.67Å. The corresponding microstructure (Figure. 5-2b) exhibits a large number of nano-twins. This is different from the typical microstructure of pure AuCu, where a much coarser laminar structure is observed after long ageing at elevated temperature [51].

The integrated intensity of the superlattice reflections of the slowly cooled sample is higher compared to the fast cooled sample, which indicates that it is more ordered. From the position of the superlattice peaks the unit cell parameters a and c of the tetragonal $L1_0$ phase can be calculated. The initial c/a ratios are 0.97 and 0.98, for R-slow and R-fast, respectively. This is considerably higher compared to the equilibrium value of c/a=0.92 obtained for the fully ordered sample. This can be understood, considering that the precipitates upon nucleation are fully coherent with the parent matrix [44,52]. This results in compressive and tensile strains along, respectively, the a- and c-axis of the $L1_0$ phase. The initial values of the peak widths are also slightly different. The origin of this difference can be found in slightly different average precipitate size, inhomogeneous elastic strain gradients, or a combination of both.
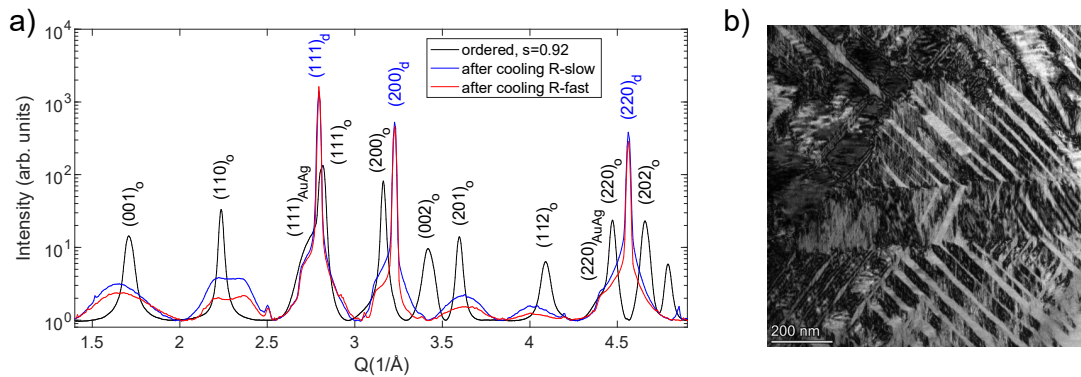
Figure. 5-2 a) X-ray diffraction pattern of a sample immediately after a recrystallization treatment (blue curve) compared to a sample after a 12h ordering treatment at 330°C (red curve). The patterns are indexed for the ordered $L1_0$, disordered A1, and disordered α_2 phase, b) TEM image of a fully ordered sample.

The experimental lattice parameter of the FCC phase is a_0=3.89Å. These shoulders increase in intensity and shift towards lower q with increasing temperature. Furthermore, they remain visible past the critical temperature of the $L1_0$ phase (not shown here). The ordered sample (black curve in Figure.

5-2a shows the same and even more pronounced shoulders on the fundamental $L1_0$ peaks. These shoulders most likely correspond to the α_2 phase, which is an FCC phase with Au and Ag in solid solution [31,140].

After cooling, the (110) diffraction peak has a particular shape that is different compared to the other superlattice reflections, as indicated with black arrows in Figure. 5-2a. It exhibits two diffuse intensity maxima around the expected (110) superlattice peak position. The intensity of these maxima was observed to be higher after cooling with a lower cooling rate (not shown here). This phenomenon has been observed before for pure AuCu systems [80,81] and theoretically explained by Hasimoto [37,85,86] as the result of short-range correlations between ordered domains. Ordered precipitates of a given variant separated in space within a single grain have either an in-phase or anti-phase relation with each other. The anti-phase correlation results in the observed diffuse maxima most notably for the (110) diffraction peak.

5.2. Microstructure evolution during heating of red gold

5.2.1. Influence of the cooling rate in red gold

Figure 5-3 displays the evolution of several superlattice and fundamental reflections during heating of sample R-fast. With increasing temperature the intensity of the superlattice reflections increases. On the other hand, the fundamental peaks broaden significantly and then split into two contributions. This is most visible for the (220) peak. Both observations are indicative for a gradual change from the disordered A1 to the ordered $L1_0$ phase. The diffuse maxima of the (110) peak first increase with increasing temperature. Above 250°C, the peak shape evolves towards a single peak with its maximum in between the two diffuse maxima. Because of this complex peak shape evolution, the (110) peak was not considered in the fitting procedure.
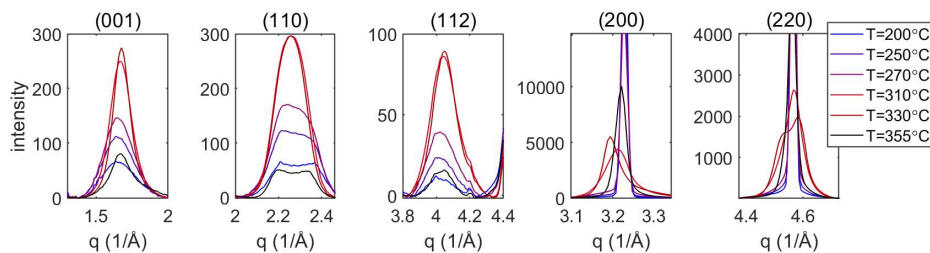
Figure 5-3 Evolution of the superlattice reflections (001), (110) and (112) and fundamental reflections (200) and (220) during heating.

Figure 5-4a displays the evolution of integrated intensity, lattice strain and full-width at half-maximum (FWHM) of the (001) and (112) superlattice reflections during heating for R-slow and R-fast. Figure 5-4b shows the corresponding evolution of the (200) and (220) fundamental peaks for R-slow, the evolution of R-fast is very similar. Based on the strain evolution of the (001) peak, we define two

characteristic temperatures T1 and T2, indicated in Figure 5-4a. Let us first consider R-fast. For temperatures below T1, the microstructure remains stable. At T1=120°C the strain in the (001) direction increases whereas it decreases for the (112). Simultaneously, the integrated intensity starts increasing. At temperature T2=250°C the (001) lattice strain starts decreasing while its integrated intensity further increases. Simultaneously, the decrease of the (112) strain accelerates. Furthermore, the (001) peak becomes narrower. On the other hand, the peak width of the (112) peak keeps on increasing up to 270°C before it starts decreasing. The transition T2 is also visible in the fundamental peaks shown in Figure 5-4b, most notably in the (220) peak. Before T2 the fundamental peaks slightly increase their width and the intensity at the tails increases. However, beyond T2 the peaks split into two contributions. Finally, at 340°C, the precipitates start to quickly dissolve, resulting in a decrease of the integrated intensity of all superlattice reflections.

Similar regimes can be distinguished for R-slow and are compared to R-fast in Table 5-2

Table 5-2. There are a few remarkable observations to be made. The temperature T1 where both the integrated intensity and lattice strain change is significantly higher for R-slow. Interestingly, the transition T2 is the same for both samples. Between T1 and T2 the (001) lattice strain of R-slow hardly increases. Beyond T2 the behaviour of both samples is very similar.

Figure 5-4 a) integrated intensity, lattice strain and FWHM evolution as a function of temperature for the (001) and (112) superlattice peaks, b) evolution of the (200) and (220) fundamental peaks for R-slow

Table 5-2 Comparison of temperatures T1 and T2 defined in Fig. 4 for R-slow and R-fast.

Sample	T1 (°C)	T2 (°C)
R-slow	200	250
R-fast	120	250

5.2.2. Influence of cooling rate and predeformation red gold

First, it should be noted that the cold rolling procedure induced a rolling texture in the material. The intensity of the (001) and (112) reflections are enhanced, whereas the (110) and (201) reflections exhibit a decrease in intensity. The ratio of the integrated intensity $\frac{I20}{I00}$ remains the same before and after deformation. Furthermore, the reduction of sample thickness by 25% induced a decrease of the total diffracted intensity by less than 5%. For that reason, the intensity differences between the predeformed and undeformed samples are mainly texture induced. It is, therefore, reasonable to assume that most precipitates are preserved during the deformation procedure. As expected, the widths of the fundamental peaks have increased significantly after the cold rolling process (see also [141]). On the other hand, the widths of the superlattice reflections are hardly influenced.

Figure 5-5a displays the evolution of integrated intensity, lattice strain and peak width of the (001) and (112) superlattice reflections during heating for the two predeformed samples, after slow cooling (R-slow-def) and fast cooling (R-fast-def), respectively. The corresponding evolution for the (200) and (220) fundamental peaks for R-slow-def is shown in Figure 5-5b. Similar to Figure 5-4 various regimes can be marked by temperatures T1 and T2, which are listed in Table 5-4.

Both the integrated intensity and the lattice strains start increasing from the start of the heating experiment (T1=50°C), which is much lower compared to the non-deformed samples. At T2=180°C, the lattice strain starts decreasing, first slow up to 250°C and then faster. The integrated intensities further increase up to 300°C before the precipitates start dissolving. Interestingly, the difference between the slow and fast cooled samples is less pronounced compared to the undeformed samples (Figure 5-4a). The evolution of the fundamental peaks shown in Figure 5-5b for R-slow-def is qualitatively similar compared to what was observed for the undeformed samples (Figure 5-4b). Up to 250°C, the peaks mainly broaden, followed by a pronounced splitting into two contributions.
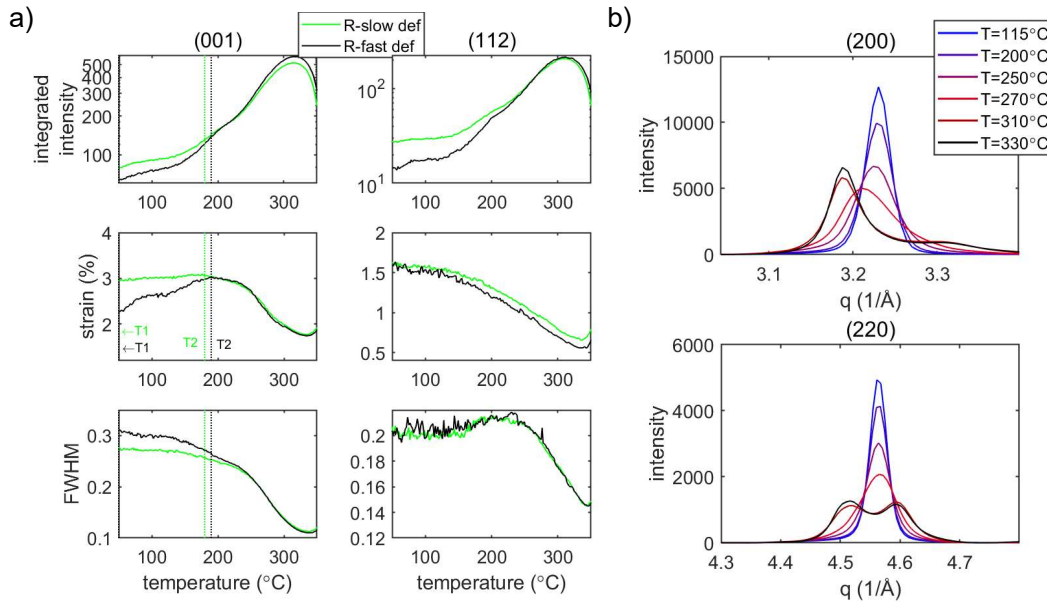
Figure 5-5 a) integrated intensity, lattice strain and FWHM evolution as a function of temperature for the (001) and (112) super-lattice peaks, b) evolution of the (200) and (220) fundamental peaks for R-slow-def.

Table 5-3 Comparison of the characteristic temperatures defined in Figure 5-4 for R-slow-def and R-fast-def.

Sample	T1 (°C)	T2 (°C)
R-slow def	50	180
R-fast def	50	190

Figure 5-6 compares the splitting of the (200) and (220) fundamental peaks for R-slow, R-fast, R-slow-def and R-fast-def after heating to 330°C. The (200) peak of the deformed samples exhibits two contributions whereas only one can be discerned for the undeformed samples. This is even more marked for the (220) peak. Here, the deformed samples exhibit a more pronounced splitting compared to the undeformed samples. This suggests that predeformation enhances ordering kinetics, which is in agreement with the observations made for the superlattice reflections. It is interesting to note that for both the undeformed and deformed samples the cooling rates seems to have very little influence on the microstructure at 330°C. Indeed, above T2 the evolution of both the superlattice and fundamental reflections is very similar.
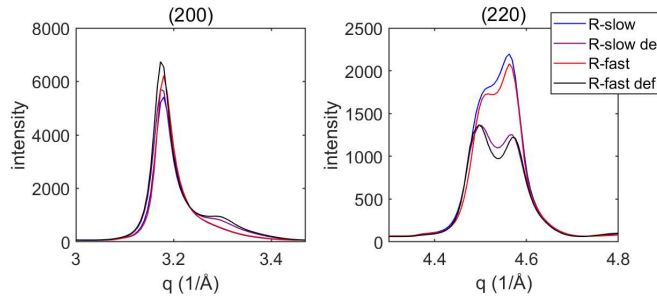
Figure 5-6 Comparison of the (200) and (220) fundamental peaks for R-slow, R-fast, R-slow-def and R-fast-def at 330°C.

5.2.3. Influence of the annealing temperature

The term annealing temperature denotes the temperature from which a cooling rate is applied in order to create the initial microstructure before heating. Figure 5-7a compares the evolution of the (112) superlattice peak for samples annealed at 550°C and 660°C for a duration of two minutes and subsequently fast cooled with the same cooling rate (-800°C/min). Fast cooling from 660°C results in a slightly earlier offset of the lattice strain and integrated intensity, presumably linked to the higher quenched-in excess vacancy density.

On the other hand, the application of a slow cooling rate (-100°C/min) on samples annealed at 550°C and 660°C results in very similar ordering kinetics upon further heating, as shown by the similar evolution of the integrated intensity, lattice strain and FWHM of the (112) peak in Figure 5-7b.
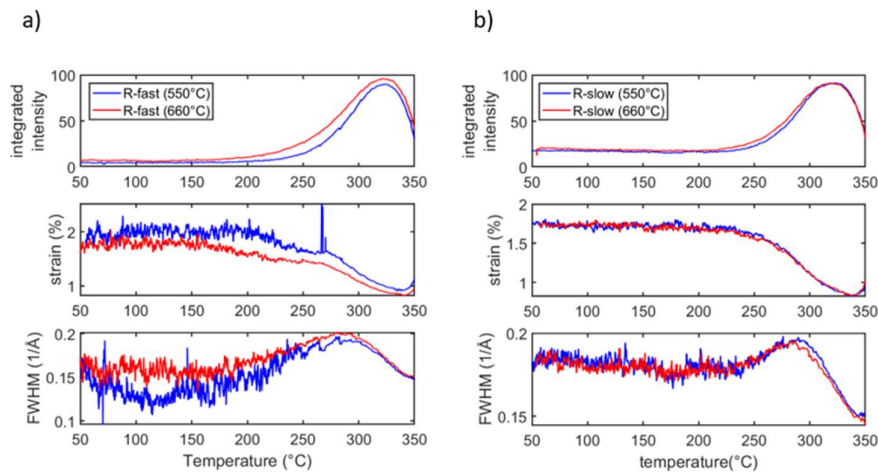
Figure 5-7 Integrated intensity, lattice strain and FWHM evolution of the (112) reflection during heating as a function of cooling rate and heat treatment temperature.

5.3. Microstructure evolution during heating of modified red gold

5.3.1. Influence of the cooling rate on the modified red gold

Figure 5-8a displays the evolution of integrated intensity, lattice strain and peak width of the (001) and (112) superlattice reflections during heating, for the slowly cooled red gold (R-slow) and modified

red gold (MR-slow). Table 5-4 shows the corresponding characteristic temperatures T1 and T2. MR-slow initially exhibits a greater integrated intensity as compared to R-slow, as well as lower lattice strain values for both the (001) and (112) superlattice reflections. On the other hand, the peak widths for both samples are very similar.

The behaviour during heating is qualitatively the same for both samples. However, the values of T1 and T2 are shifted to lower temperatures for MR-slow. MR-slow exhibits a higher integrated intensity and lower lattice strain compared to R-slow. This points to a more advanced ordered state at a given temperature. Figure 5-8b compares the fundamental (200) and (220) diffraction peaks at 320°C. The more pronounced peak splitting in MR-slow indicates a more advanced ordered state.
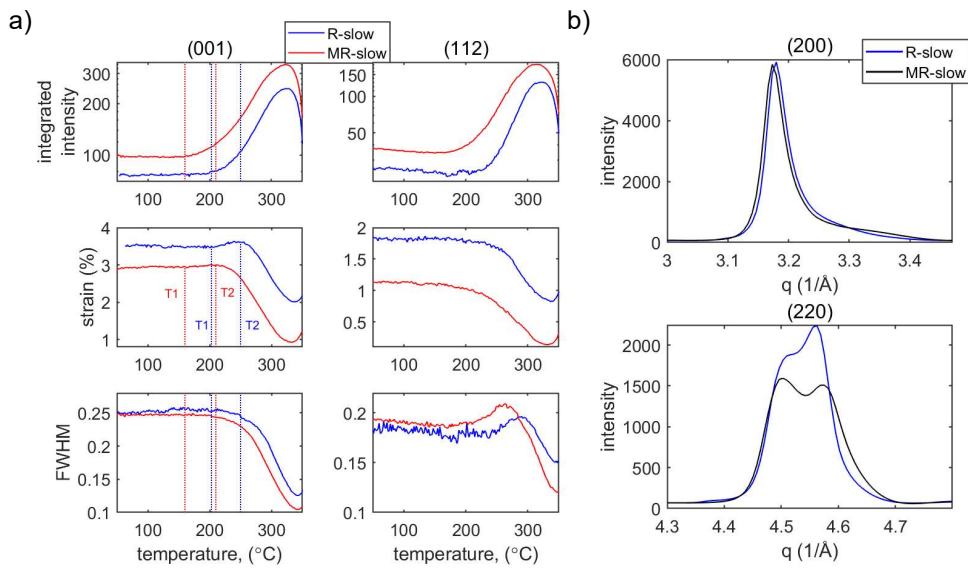
Figure 5-8 a) Evolution of integrated intensity, lattice strain and FWHM as a function of temperature for (001) and (112) super-lattice peaks, b) comparison of the (200) and (220) diffraction peaks for R-slow and MR-slow at 320°C

Table 5-4 Comparison of the characteristic temperatures for R-slow and MR-slow

Sample	T1 (°C)	T2 (°C)
R-slow	200	250
MR-slow	170	220

5.3.2. Influence of the cooling rate and predeformation on the modified red gold

Figure 5-9a displays the evolution of integrated intensity, lattice strain and peak width of the (001) and (112) superlattice reflections during heating, for predeformed modified red gold after slow (MR-slow-def) and fast cooling (MR-fast-def), compared to predeformed red gold after fast cooling (R-fast-def). The (001) lattice strain in both MR-fast-def and MR-fast-def starts increasing at T1=80°C, with a

simultaneous increase of the intensity. In contrast, for R-fast-def the lattice strain and intensity increase from the beginning of the heating experiment at T1=50°C. On the other hand, the lattice strain starts relaxing much earlier in the modified red gold (T2=150°C). After T2 the evolution of superlattice reflections for the modified red gold is very similar, independent on the initial cooling rate. Figure 5-9b compares the (200) and (220) fundamental peaks for the deformed red and modified red gold samples at 320°C. Both peaks exhibit clear splitting into two contributions. This effect is slightly more pronounced for the modified red gold, independent of the initial cooling rate.

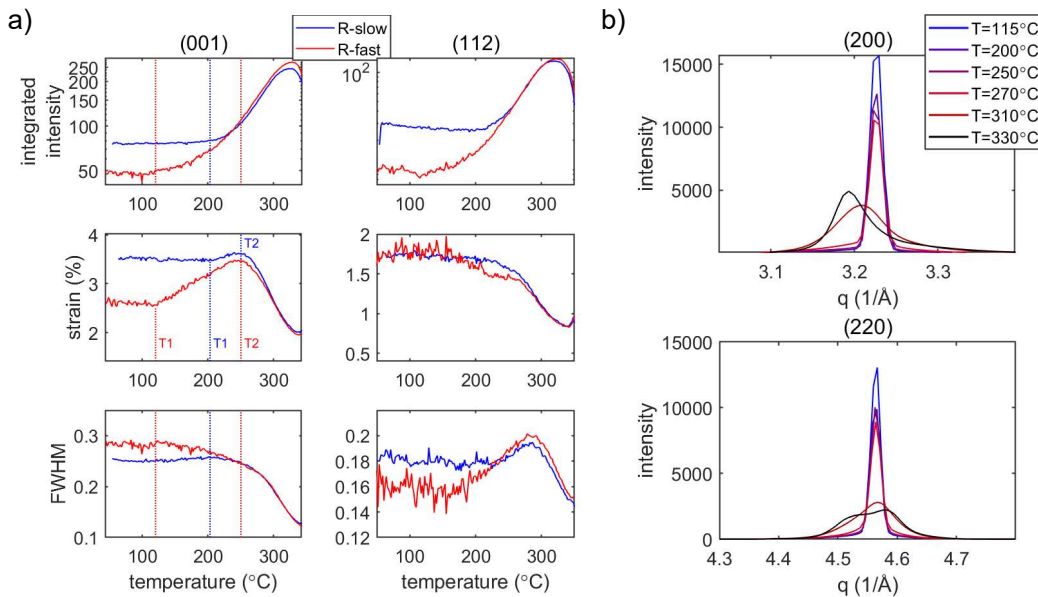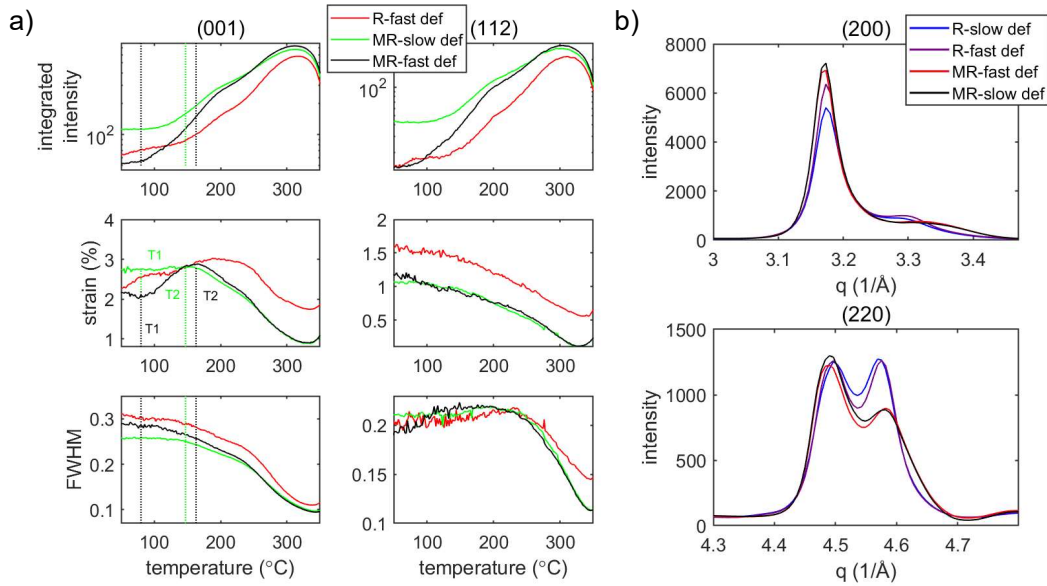Figure 5-9 a) integrated intensity, lattice strain and FWHM evolution as a function of temperature for the (001) and (112) super-lattice peaks, b) comparison of the (200) and (220) fundamental peaks for R-fast-def and MR-fast-def at 320°C.

Table 5-5. Comparison of the characteristic temperatures for MR-slow-def and MR-fast-def

Sample	T1 (°C)	T2 (°C)
MR-slow-def	80	150
MR-fast-def	80	160

Chapter 6 Discussion and conclusions

The influence of thermal and mechanical processing on the $A1 \rightarrow L1_0$ ordering phase transformation in red gold has been studied by combining *in situ* temperature X-ray diffraction experiments with transmission electron microscopy investigations. The link between the microstructural evolution and thermo-mechanical history has been established. The following section discusses and summarizes the achieved results.

6.1. Initial microstructures in red gold

6.1.1. Microstructure after continuous cooling

Industrial continuous furnaces show characteristic cooling rates between -100°C/min and -800°C/min for the red gold parts considered in this study. Some degree of ordering takes place when cooling down at these rates. However, only advanced characterization techniques such as synchrotron X-ray diffraction (Figures 5-1 b-d) and TEM are able to reveal it.

After cooling, X-ray diffraction patterns show the diffraction peaks of a FCC structure, *i.e.* the disordered matrix, together with low intensity and broad superlattice peaks that correspond to the ordered $L1_0$ nanodomains.

The diffracted intensity of the superlattice reflections depends on the cooling rate. Slow cooling rates result in stronger superlattice reflections, indicating that the volume density of $L1_0$ phase is greater as compared to fast cooled samples. This is expected, as during slow cooling, samples are subject longer to temperatures just below T_c where ordering kinetics are fast.

On the other hand, it is expected that the fast cooled samples retain a certain concentration of quenched-in excess-vacancies[45]. For instance, assuming the diffusion coefficient of Cu in AuCu (E_{act}=27kcal/mol, A=0.21 from [142]) and a vacancy formation energy in AuCu of 1eV [143]. The apparent diffusion coefficient at 25C after a quench from 660C is 5.33e-10cm^2/s. Using the approximation equation for diffusion time, we get that after 5 min, a Cu atom has travelled 250 µm.

In general, the large breadth of the superlattice reflections is indicative of a very small crystallite size, in the order of a few nm. Complementary TEM observations support this hypothesis, showing extremely small ordered domains homogeneously dispersed within the disordered grains (see Figure 2-10). IFFT processing of HRTEM images show a $L1_0$ domain structure similar to the ones reported in literature on water-quenched AuCu [77,80]. The extension of the ordered domains is about 2nm

(Figure 1-14). However, this value must be taken as an upper limit, since the thickness of the observed lamella was estimated to be around 10-20nm.

Following with the analysis of the X-ray diffraction patterns of the continuously cooled samples, two broad maxima are observed around the $(110)_o$ superlattice peak position instead of the expected $(110)_o$ single peak. X-ray diffraction studies on the ordering kinetics of equiatomic AuCu [81,144] suggest that the presence of the broad maxima at the early stages of ordering correspond to in-plane periodic antiphase boundaries, similar to the ones observed in the PAP structure AuCu II. However, it is unlikely that *periodic anti-phase boundaries* develop in the microstructure when the ordered domains are still nano-sized and unconnected to each other, as suggested by TEM observations (Figure 1-11).

Interestingly, Guinier and Griffoul [83] observed two broad maxima around the $(110)_o$ peak position during ordering of a system that does not form a PAP structure, the $AuCu_3$ system (A1$\rightarrow$ L1$_2$). They suggested that the origin of the broad maxima is assigned to short-range interactions of the chemically ordered *nano*domains in antiphase relationship, and supported this idea by calculations on the diffracted intensity. Later on, Hashimoto [37,85,86] developed a diffraction model considering the interference effects between *nano*-sized ordered domains embedded in a disordered matrix. This model predicts two broad maxima around the $(110)_o$ peak as a result of the constructive interference of short-range spatial correlations between the ordered *nano*domains in anti-phase relation which extend over large areas, as Guinier and Griffoul suggested .

Hashimoto advanced that this phenomenon occurred at the early stages of ordering, when the ordered *nano*domains form within the disordered matrix, but also when the fully ordered L1$_0$ structure progressively dissolves into A1. When the temperature increases and exceeds Tc, the degree of order progressively decreases until ordering is mostly destroyed and only ordered *nano*domains in antiphase relation prevail before full dissolution. This effect has been observed experimentally, when the single $(110)_o$ peak transforms into two $(110)_o$ maxima before full dissolution at around 340°C (Figure 5-3).

It is therefore proposed that the presence of the two broad maxima is a microstructure-related diffraction phenomenon, characteristic of a homogeneous and fine dispersion of ordered *nano*domains embedded in the disordered matrix. Indeed, the experimental observation of AuCu II as an intermediate phase between L1$_0$ and A1 during heating at 10°C/min is improbable due to the sluggish character of AuCu II formation [26].

The diffraction peaks corresponding to the fundamental reflections of the $L1_0$ phase are not observed because they overlap with the fundamental reflections of the FCC phase. This is indicative of the coherency between the ordered domains and the disordered matrix, implying that $L1_0$ phase is close to cubic in symmetry c/a ≈ 1.

In summary, the microstructure after cooling is characterized by a metastable FCC disordered cubic matrix and a very fine dispersion of coherent, chemically ordered and nano-sized domains within the disordered grainsof the matrix. Fast cooling results in lower volume density of $L1_0$ domains and presumably a higher density of excess-vacancies compared to slow cooled samples.

6.1.2. Microstructure after plastic deformation

After cooling, some of the samples are subject to 25% cold rolling, which changes the microstructure by inducing a rolling texture and can influence the relative intensities of the diffraction peaks. However, the intensity ratio of the $(001)_o$ and $(002)_d$ peaks remains constant before and after cold rolling. This implies that the cold rolling process does not destroy order. The fundamental peaks exhibit significant broadening after deformation, indicative for the built-up of a dislocation network (Figure 4-20). Figure 6-1 shows the $(110)_o$ superlattice peak for R-slow, R-slow-def, R-fast and R-fast-def. The diffuse maxima after deformation are less pronounced. This is most likely related to the presence of strain fields in the matrix caused by deformation-induced dislocations, which might cause the loss of the anti-phase relation between the ordered domains.
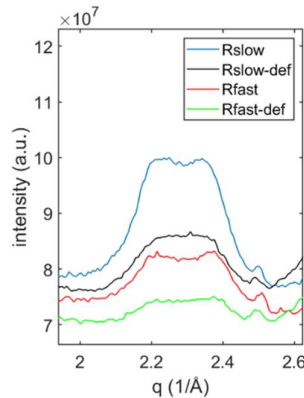
Figure 6-1 (110) diffuse maxima after cooling in the deformed and undeformed condition for R-slow and R-fast

6.2. Tracking chemical order with X-ray diffraction

In general, phase transitions are quantified as the evolution of the volume density of the phase of interest against time (isothermal experiments) or temperature (heating experiments). The phase volume density can be calculated from a X-ray diffraction pattern with full-pattern fitting methods.

However, the diffraction patterns resulting from coexisting and coherent A1 and $L1_0$ phases are difficult to quantify with state-of-the art methods.

The reasons why the diffraction patterns are difficult to fit by full-pattern fitting methods required for quantifying the $L1_0$ phase fraction are the following. On the one hand, the coherency between the $L1_0$ phase and the cubic matrix results in complex strain states between both phases. Initially, this induces a distortion in the $L1_0$ lattice and next, influences the shape of the fundamental peaks. On the other hand, the presence of two broad maxima around the $(110)_o$ peak position is a microstructure-related feature that is not treated in available fitting methods.

A major observation of this study is the distortion of the $L1_0$ lattice at the early stages of ordering, followed by the distortion of the matrix. The appearance of superlattice peaks is indeed related to chemical ordering in the matrix, however, they cannot be fitted to a perfect $L1_0$ structure. In other words, the c/a ratio calculated from two independent sets of peaks, *i.e.* the (001)/(110) and (201)/(112), does not coincide (Figure 4-11). This is understood as a distortion of the ordered domains induced by the coherency with the matrix. In a more advanced stage of ordering, the coherency strains between bigger $L1_0$ domains with the matrix induce the distortion of the A1 phase by tweed (further discussed later). This is revealed by changes in the intensity of the tails in the fundamental peaks, followed by a transition from a single peak to a peak split.

Rietveld refinement [145] cannot be performed on systems where 1) the unit cells of the phases under study are distorted in an unknown manner and 2) the peak shape of the superlattice and fundamental peaks is strongly influenced by the microstructure.

Whole Powder Pattern Modelling (WPPM) methods, e.g. PM2K [146], are the proper alternative to fit these systems because they incorporate physical models that account for microstructural effects on the diffraction peaks, such as crystallite size, crystallite size distributions and elastic strain. However, the physical models reproducing the A1→$L1_0$ coherency strain evolution and the related microstructural effects (distortion of the $L1_0$ lattice and tweed) are still missing; as well as the implementation of Hashimoto's diffraction model. Moreover, no models for the strong diffuse background present during the early stages of ordering have been found, which would improve the fitting results.

Consequently, calculation of the evolution of the $L1_0$ phase fraction is not achievable, therefore the evolution of chemical order is followed by single-peak fitting of the superlattice reflections, in particular the $(001)_o$ and $(112)_o$ during the heating experiments.

6.3. Early stages of ordering during heating

It is known that the formation and growth of coherent $L1_0$ domains within the cubic matrix generate non-local and long-range strain fields due to the lattice mismatch between the disordered FCC matrix (a_0=3.89Å) and the $L1_0$ domains ($a_{equilibrium}$=3.97Å, $c_{equilibrium}$=3.67Å) as well as between different orientational $L1_0$ variants [51,69]. These strain fields are most notable along the c-axis, which is the crystallographic direction that undergoes the greatest lattice changes. For this reason, the evolution of the $(001)_o$ lattice strain, calculated from the $(001)_o$ peak position, is selected as the reference parameter to study the stages of ordering during heating.

6.3.1. Stage I: increase in the (001) lattice strain

During heating with a moderate heating rate of 10°C/min, the onset of ordering is confirmed by the increase in the $(001)_o$ integrated intensity, which is proportional to the volume density of the $L1_0$ phase. The evolution of the integrated intensity is monotonic until T=340°C, where the $L1_0$ phase starts to transform back into A1. With the onset of ordering, the FWHM monotonically decreases. This pinpoints to the growth of the ordered domains and maybe micro-strain relaxation within the ordered crystallites.

Interestingly, the $(001)_o$ lattice strain exhibits a non-monotonic behaviour. Based on the evolution of the lattice strain two characteristic temperatures are defined. At temperature T1 the lattice strain starts increasing, which coincides with the onset of ordering. At temperature T2 the lattice strain decreases towards equilibrium (*i.e.* zero lattice strain), which indicates the presence of a relaxation process. Prior to T1, the microstructure remains stable within the sensitivity of our measurements.

The behaviour of the $(001)_o$ lattice strain can be explained as follows. Initially, the nano-sized ordered domains are homogeneously dispersed within the matrix. At this point, the coherency between the matrix and the $L1_0$ domains result in considerable *pulling* of the matrix along the c-axis of the ordered domains, which results in an overall tensile $(001)_o$ strain on the $L1_0$ lattice. When temperature T1 is reached, the volume fraction of $L1_0$ phase starts increasing but it is still low enough for the matrix to confine the ordered lattice to a close-to-cubic symmetry. The growth of the ordered domains, as suggested by the continuous decrease in FWHM, drives the $L1_0$ lattice towards its respective tetragonal distortion (c/a → 0.92). This means that when the ordered lattice starts *shrinking* along the c-axis, the matrix *pulls* harder and results in an increasing $(001)_o$ tensile strain in the $L1_0$ domains. At temperature T2, the increasing volume density of the *coherent* $L1_0$ domains can no longer be withhold by the matrix. It is then when the matrix reaches a strain limit and sets in a microstructural relaxation mechanism. Both T1 and T2 depend on the thermo-mechanical history and chemical composition.

Moreover, the different lattice strain evolution of the $(001)_o$ and $(112)_o$ peaks is to be noted. The $(112)_o$ lattice strain shows a monotonic relaxation in contrast to the non-monotonic behaviour of the $(001)_o$ lattice strain (Figure 5-4). It is anticipated that the origin of this behaviour lies on the anisotropy of the $L1_0$ lattice (AuCu I) [147] due to the remarkable anisotropy of Au and Cu [138].

6.3.2. Stage II: relaxation of the (001) lattice strain and lattice relaxation mechanism

In order to understand the strain relaxation mechanism, the $(200)_d$ and $(220)_d$ fundamental peaks have been inspected in the 1D and 2D diffraction patterns and complemented with TEM observations.

Inspection of the 1D diffraction patterns at temperature T2, when the lattice strain relaxation occurs, shows that the $(200)_d$ and $(220)_d$ fundamental peaks display increasing intensity at the tails (Figure 5-4b). Later on, this evolves into a peak split on both the $(200)_d$ and $(220)_d$ peaks (Figure 5-4b)

It is known that the transition from a partially ordered $A1 + L1_0$ microstructure towards a single-phase $L1_0$ microstructure involves the progress of the aspect ratio $c/a \approx 1$ (coherent domains) towards an aspect ratio $c/a \approx 0.92$ (relaxed domains) in the $L1_0$ phase. This means that a fully relaxed $L1_0$ lattice will exhibit peak splitting of the diffraction peaks affected by the a- and c-parameters, notably the $(200)_d \rightarrow (200)_o + (002)_o$ and the $(220)_d \rightarrow (220)_o + (202)_o$ (Figure 5-2).

However, the expected peak positions of the $(200)_o$, $(200)_o$, $(220)_o$ and $(202)_o$ peaks do not correspond to the observed peak split on the $(200)_d$ and $(220)_d$ peaks (Figure 4-8).

Inspection of the $(200)_d$ and $(220)_d$ diffraction rings in the 2D diffraction patterns at T < T2 and T ≈ T2 is crucial in understanding the microstructural relaxation mechanism. Figure 6-2 displays the 2D diffraction patterns for R-fast at T < T2 (150°C) and T ≈ T2 (270°C), respectively. Note that the same colour-scale has been applied on both images for visualization purposes, which explains why spotty rings are observed instead of continuous rings.

At T < T2, the $(200)_d$ and $(220)_d$ diffraction rings show the typical continuous powder diffraction rings. At T ≈ T2, intense cross-like features appear, most markedly on the $(200)_d$ rings. These features are responsible for the increase of intensity on the tails of the $(200)_d$ and $(220)_d$ diffraction peaks on the 1D diffraction patterns. At T >> T2, not shown in Figure 6-2, these crosses evolve into a peak split with very similar intensities.

Early works on equiatomic AuCu ordered at low temperatures reported the appearance of cross-like features on the fundamental spots in electron diffraction patterns [51,69] and the arrangement of very small and fine ordered domains along <101> direction. This configuration is known as the 'tweed configuration' [80]. Tanner's electron microscopy investigations on Cu-2Be [57] attributed the

diffraction cross-like features to $\{110\}[1\bar{1}0]$ elastic shear strains produced by the *coherent* tetragonal precipitates in an anisotropic FCC matrix. He suggested that this model was applicable to the initial stages of ordering in equiatomic AuCu [51], CoPt [148,149], NiPt and Ni_3V. Computer simulations by Silberstein and Clapp [150] supported Tanner's model. Furthermore, these simulations predicted that the tetragonal distortions lead to the tweed formation in the FCC matrix. It was predicted that the onset of tweed in the FCC matrix resulted in a peak splitting of the $(200)_d$ and $(220)_d$ diffraction peaks, similar to what is observed in this work (Figs. 5-4b, 5-5b, 5-6, 5-8b and 5-9b). Moreover, experimental investigations on ageing alloys (Cu-Be) and ordering alloys (Co-Pt) by Tyapkin [58,60] suggested that $\{110\}[1\bar{1}0]$ shear induces a monoclinic-like distortion in the cubic matrix, which fits with the tweed distortion.
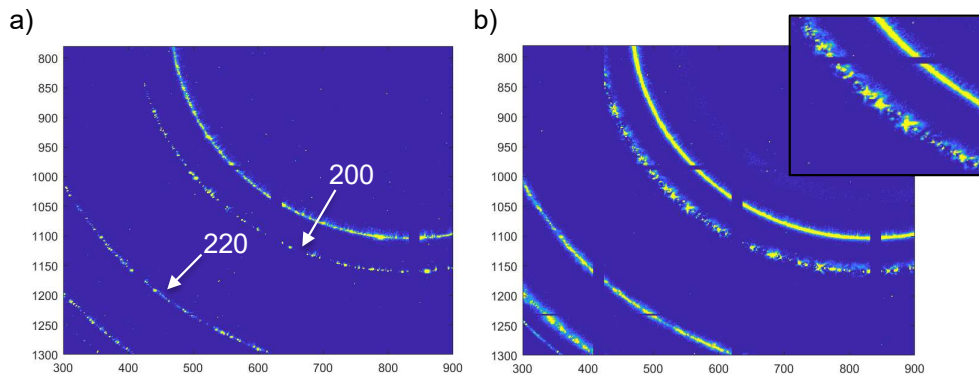
Figure 6-2 2D XRD patterns for sample R-fast a) before the onset of tweed at T=150°C, b) after the onset of tweed at T=270°C.

In view of the previous facts, the following scenario is proposed. During stage I, the $(001)_o$ lattice strain increases in the ordered domains due to the coherency with the FCC matrix, while the shear strains grow stronger in the matrix. At T ≈ T2 the shear strains are intense enough to interfere with the diffracted beam, as evidenced by the sharp cross-like features, and reach the elastic limit of the matrix. Then, tweed sets in as the microstructural relaxation mechanism, evidenced by the $(200)_d$ and $(220)_d$ peak splitting. The relaxation of the matrix by tweed inevitably causes a relaxation in the $(001)_o$ lattice strain of the ordered domains.

Complementary transmission electron microscope observations confirmed the presence of tweed in the microstructure. For that, two samples displaying the X-ray features associated to stage II were prepared, as shown in Figure 6-3. *Sample A* showed a microstructure equivalent to that of T ≈ T2, *i.e.* increasing intensity on the tails of the $(200)_d$ and $(220)_d$ peaks. *Sample B* showed a microstructure equivalent to that of T > T2, i.e. peak split of the $(200)_d$ and $(220)_d$ peaks. These samples were obtained after isothermal ageing at 250°C during 20 minutes. *Sample A* and *B* belong to the reported isothermal *in situ* measurements (chapter 4) in the undeformed and deformed condition, respectively.
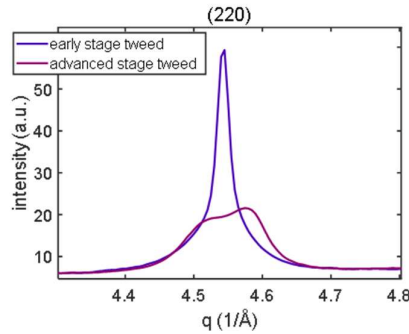
Figure 6-3 (220) peak shape of samples A and B

Figure 6-4 a and b shows the TEM DF images using the (001) superlattice reflection along the [110] zone axis for *samples A* and *B*, respectively. Both TEM DF images show a tweed configuration of the ordered domains, evidenced by their alignment along the [111] crystallographic directions. Since the ordered domains are coherent with the matrix, the tweed of the matrix results in a tweed configuration of the ordered domains too.

Sample A, Figure 1-2a, shows a very early stage of tweed, where the homogeneously and finely dispersed ordered domains start rearranging into the tweed configuration. While *sample B*, Figure 6-4b, shows a more developed and coarser tweed structure. These observations suggest that a greater peak split correlates to a more developed tweed structure.
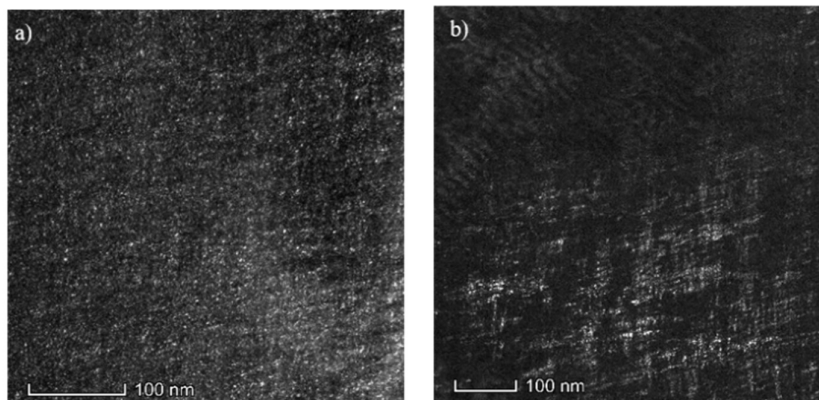
Figure 6-4 a,b) DF TEM images on the (001) superlattice reflection along the [110] zone axis, on undeformed and deformed samples after isothermal ageing at 250°C, 20 min, respectively.

In summary, it is proposed that intense shear strains in the matrix initiate stage II and outsets the tweed microstructure, which relaxes the (001)$_o$ lattice strain of the ordered domains. The XRD footprints of these events have been correlated to microstructural observations by electron microscopy.

6.4. Influence of thermo-mechanical history and chemical composition on the early stages of ordering in red gold

The influence of thermo-mechanical history has been evaluated at a laboratory scale by applying a artificial ordering treatments (a heating ramp) on samples with different initial microstructures. The undeformed state has been evaluated after slow (-100°C/min) and fast (800°C/min) cooling rates, which mimics industrially relevant conditions. The deformed state consists on applying a 25% reduction cold rolling on previously cooled samples (fast and slow). Additionally, the influence of chemical composition was evaluated by addition of Pd (0.1-1.1 %wt.) and Sn (0.1-2 %wt.).

The magnitude of the lattice strain in the ordered domains immediately after cooling depends on the cooling rate. The slow cooled samples exhibit a larger $(001)_o$ lattice strain compared to the fast cooled samples (Fig. 5-4a). This suggests that a greater volume density of $L1_0$ phase in the disordered matrix increases the lattice strain in the ordered domains. This might be due to the larger domain size in the slow cooled sample, as suggested by the narrower peak breadths of the superlattice reflections in the slow cooled sample (Figure 5-4a).

Figure 6-5a and Figure 6-5b compares the evolution of integrated intensity and lattice strain of the $(001)_o$ reflection for all red gold samples. Note that the integrated intensities have shifted to an arbitrary initial value in order to compare the ordering rate. For the undeformed samples, ordering starts earlier in the fast cooled samples, which display a shift of T1 to lower values. Complementary heating experiments performed on samples fast cooled from 660°C and 550°C show more enhanced low temperature ordering in the sample cooled from 660°C, which contained a greater density of vacancies before the cool down (Figure 5-7a). With other words, it is suggested that fast cooling samples exhibit an enhanced ordering rate attributed to enhanced diffusion of Cu in the fast cooled sample because of a higher density of quenched-in excess-vacancies[45].
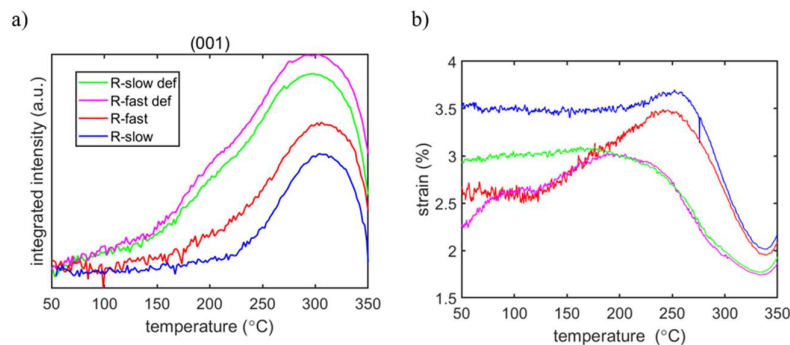
Figure 6-5 Comparison of the evolution of a) the integrated intensity and b) (001) lattice strain during heating for R-fast, R-slow, R-fast def and R-slow def.

Cooling rates have a remarkable influence on the lattice strain increase between T1 and T2. For instance, in the undeformed samples, fast cooling induces +1% strain increase, whereas slowly cooled samples exhibit a strain increase as little as +0.3%. At temperature T2 the lattice strains for the fast cooled samples reach nearly the same strain level as the slowly cooled samples. This supports the idea that the matrix can only withstand a maximum amount of lattice strain before a relaxation mechanism sets in, and implies that both samples reach similar microstructure at T2. Indeed, the integrated intensity and FWHM curves overlap for both samples from temperature T2 and the $(200)_d$ and $(220)_d$ fundamental peaks are very similar.

Slow cooling rates lead to a volume density of $L1_0$ phase such that the matrix is strained close to its elastic limit. As a result, further ordering will quickly result in the relaxation of the microstructure. However, fast cooling rates result in a lower initial volume density of $L1_0$ phase and the associated lower lattice strain in the domains. Upon further ordering and growth of the domains, the accumulation of lattice strain is therefore larger before relaxation, which might result in more pronounced changes in the physical properties of the alloy.

The deformed samples exhibit a very distinct behaviour. Firstly, ordering starts already at the beginning of the experiment (T ≈ 50°C) with a significantly enhanced ordering rate compared to the undeformed samples (Figure 6-5a). There is little difference in the evolution of the integrated intensity between fast and slow cooled deformed samples. This indicates that the excess-vacancies present after fast cooling plays only a minor role in the ordering kinetics as compared to the dislocations introduced by the plastic deformation. It is expected that an enhanced ordering rate will result in faster build up strain in the matrix, and therefore trigger earlier the strain relaxation mechanism. Indeed, the relaxation temperature T2 shifts to lower temperatures. Complementary isothermal treatments of cold rolled samples confirm that the ordering rate in the plastically deformed samples is enhanced compared to the undeformed regions (see Figure 4-21).

Secondly, the lattice strain increase in the deformed samples is less than that of the undeformed samples (Figure 6-5b), suggesting that the presence of dislocations partially relieves the build-up of lattice strain in the $L1_0$ lattice. In addition, *in situ* isothermal experiments on deformed and undeformed samples suggest enhanced domain growth in the deformed samples (see Figure 4-21).

It is likely that the $L1_0$ lattice is better accommodated within the strained regions around the dislocations by means of $L1_0$ variant selection. In other words, the $L1_0$ domain aligns its c-axis perpendicular to the elastic tensile component around the dislocations. In this way, the tetragonal distortion of the $L1_0$ lattice is partially compensated by the compressive strain field.

Experiments [96,151,152] and simulations [95] confirmed that an externally applied stress field during ordering promotes the formation of a given $L1_0$ variant, inducing internal stress fields that further

enhances the formation of a similar variant. This autocatalytic process enhances the ordering rate and the built-up of strain in the system. We anticipate that a similar mechanism is present in the predeformed samples as a consequence of local internal stress fields induced by the dislocation network created by the cold rolling process.

Similar observations can be made for the chemically modified red gold samples (MR alloy). Figure 6-6 compares the evolution of integrated intensity for red gold alloys (R-slow, R-slow-def and R-fast-def) and the modified red gold alloys (MR-slow, MR-slow-def and MR-fast-def). Note that the integrated intensity of each samples has been shifted to a common origin for comparison of the ordering rate.

The integrated intensity of MR-slow increases at a lower temperature (T1) compared to R-slow, suggesting that additional alloying with Sn and Pd lowers the critical temperature for ordering. The addition of Sn and Pd to the alloy increases the off-stoichiometry, which generally reduces the stability temperature range of the ordered phase [15].
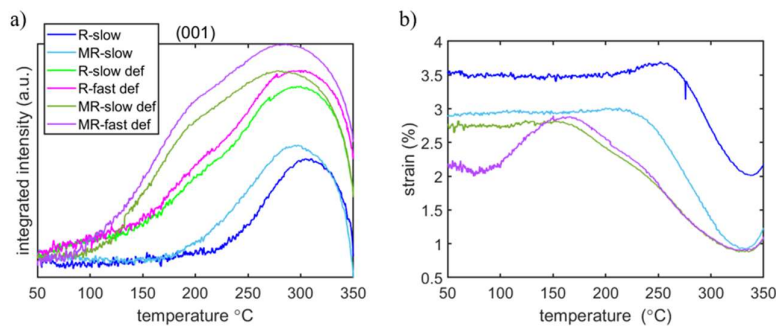
Figure 6-6 Comparison of the evolution of the integrated intensity during heating for red gold alloys (R-slow, R-slow-def and R-fast-def) and modified red gold alloys (MR-slow, MR-slow-def and MR-fast-def).

The lattice strain of the MR-slow samples hardly increases before reaching T2 (Fig. 6-6b). This suggests that slow cooling develops a degree of order close enough to the elastic limit of the disordered matrix, similar to what is observed in the R alloy. In contrast, the lattice strain of the fast cooled samples clearly increases between T1 and T2, and reaches a similar lattice strain level as the slowly cooled samples before relaxation sets in (Fig. 5-9a). It seems that the MR allow exhibits a lower increase in the lattice strain compared to the R alloy as well as lower T2 temperatures both in the undeformed and predeformed samples. Note that the sample MR-fast could not be measured due to lack of synchrotron time.

Predeformation substantially enhances the ordering rate at low temperature in the MR alloy compared to the R alloy, although it has qualitatively the same influence on the ordering kinetics. It is interesting to point out that the predeformed MR alloy shows a slightly higher T1 compared to predeformed R alloy (see Table 5-3 and Table 5-5). This means that the MR alloy is more stable at room temperature in the deformed state, however, when subject to a temperature raise the ordering

kinetics will be faster. It is anticipated that this is related to a reduced diffusion at low temperatures due to the addition of Pd [112].

As mentioned before, there is a clear correlation between the ordering rate (Figure 6-5a and Figure 6-6a) and the temperature T2 (Figure 6-5b and Figure 6-6b). Faster ordering rates build-up faster the elastic strain in the matrix and result in lower values of T2. This implies that tweed develops faster with the addition of Pd and Sn and predeformation (see Figures 5-6, 5-8b and 5-9c).

Figure 6-7 summarizes the temperatures T1 and T2 as a function of the initial condition. The lower connected dots correspond to temperature T1, while the upper connected dots correspond to temperature T2. Predeformation has the greatest influence in reducing temperatures T1 and T2. Faster cooling rates mainly shift T1 to lower temperatures. Chemical composition modification by addition of Sn and Pd slightly reduces T1 and T2. Finally, fast cooling rates result in a greater increase of lattice strain upon ordering, while predeformation shows less lattice strain increase upon ordering.
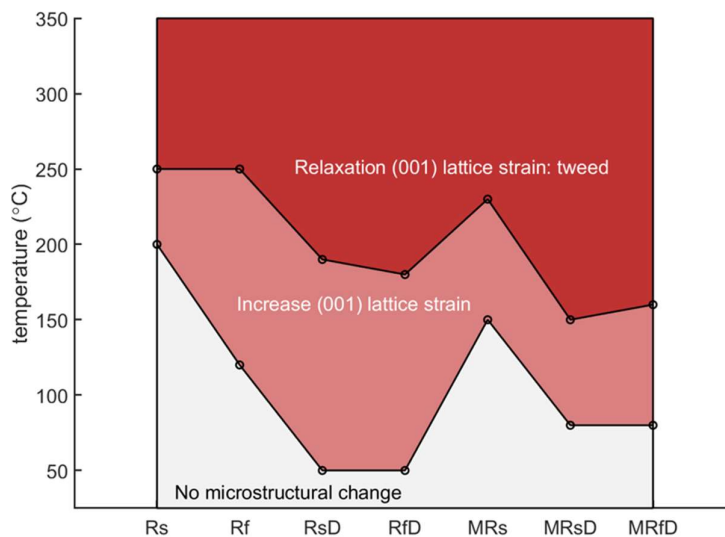
Figure 6-7 Summary chart of temperatures T1(lower temperature line) and T2 (upper temperature line) for all the investigated samples. Red gold alloys: Rs (slow cooling), Rf (fast cooling), RsD (slow cooling and predeformed), RfD (fast cooling and predeformation). The same nomenclature is followed for the modified red gold alloys, MR.

6.5. XRD footprints of the microstructural evolution during ordering

A global and systematic study to correlate the evolution of the ordered microstructure with the XRD footprints in a diffraction pattern was undertaken. Three distinct microstructural stages have been identified by electron microscopy in red gold. Figure 6-8 summarizes the X-ray diffraction features characteristic of each stage: (I) build-up of lattice strain, (II) formation of tweed and (III) twinning.

Stage I: nano-sized $L1_0$ domains of the three orientational variants are *coherent* with the disordered matrix and homogeneously dispersed within the cubic grains. The coherency induces increasing shear strains in the matrix, which grow in magnitude with the further growth of the ordered domains. The microstructure-related footprints in XRD correspond to the presence of two broad maxima around the $(110)_o$ superlattice peak position, see Figure 6-8a.

Stage II: the strong shear strains induced in the disordered matrix by the *coherent* ordered domains sets in a local strain relief mechanism by the formation of tweed in the disordered matrix, as a result of its high elastic anisotropy [57,153,154]. Tweed results in the alignment of the coherent domains along the <1-10> directions of the cubic matrix. Eventually, the tweed structure coarsens, probably by reorientation of the ordered domains or preferential growth of well-aligned domains. This is correlated to 1) the advent of the single $(110)_o$ peak (Figure 6-8a) and 2) the increase in intensity of the tails on the $(200)_d$ and $(220)_d$ fundamental peaks, which evolves into a peak split upon development the tweed structure (Figure 6-8b). The development of a single $(110)_o$ peak and disappearance of the two broad maxima are ascribed to the extinction of the short-range spatial correlations between the ordered domains due to the onset of tweed.

Stage III: further growth of the ordered domains results in coalescence and may form anti-phase boundaries. Eventually, twinning takes place in order to release strains arising from ordered regions with different c-axis orientations. The onset of twinning in the ordered phase is correlated to the display of the $(200)_o$ and $(220)_o$ $L1_0$ peaks in the diffraction pattern, which corresponds to a *fully relaxed* $L1_0$ phase as a result of the twin.
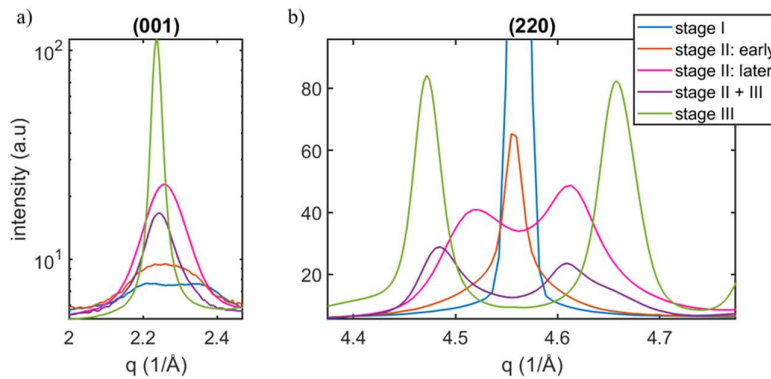
Figure 6-8 a) (110) peak shape at stage I (two diffuse maxima) and at stage II (single peak). b) X-ray diffraction peak of the $(220)_d$ at different ordering stages.

6.6. Evolution of the $L1_0$ microstructure during manufacturing

Chemically ordered domains are present during the manufacturing process of 18k red gold alloys. More precisely, nano-sized and *coherent* ordered domains that are homogeneously distributed within the metastable disordered matrix. Continuous furnaces prevent from fast cooling rates (such as water quenches), which result in natural ageing due to a high quenched-in excess-vacancy density (Figure 1-1). However, their characteristic cooling rates (-100°C/min to -800°C/min) induce chemical ordering in the microstructure at the early stages and build up shear strains in the matrix. This microstructure seems to remain stable up to 120°C or 200°C for the fast and slow cooled samples, respectively. However, it is anticipated that plastic deformation enhance the ordering kinetics at low temperatures. Under the manufacturing conditions considered in this study, the microstructure has not been observed to evolve beyond stage I (coherent domains that constrain the matrix with shear strains).

The plastic deformation induced during a straightening operation induces low temperature ordering (*i.e.* natural ageing) in the deformed regions while the microstructure of the undeformed regions of the sample remains stable (see Figures 4-16 and 4-17). This suggests that heterogeneous deformation within the samples will induce microstructural gradients with respect to the degree of order, which will inevitably have an influence on the internal stress state of the alloy. Furthermore, any temperature raise (i.e. heat produced during mechanical operation) will accelerate the ordering rate thus magnify the microstructural gradients.

Furthermore, *in situ* experiments show that the applied cooling rate before the deformation operation does not influence greatly the ordering rate. However, the increase of the lattice strain in the ordered domains during ordering is greater after fast cooling compared to slow cooling. This implies that the disordered matrix undergoes larger strain gradients on fast cooled and predeformed samples.

Finally, it has been shown that chemical composition modifications can tune the ordering kinetics. In the case of the addition of Sn and Pd, the critical temperature for ordering is slightly reduced. In the deformed condition, the microstructure remains stable up to around 90°, regardless the previous cooling rate, although the ordering rate turns out to be much faster as compared to a predeformed red gold.

6.7. Conclusions

In situ temperature high-energy X-ray diffraction experiments were performed on 18k red gold alloys with different thermo-mechanical histories and chemical composition, with the aim to study the early stages of the ordering transformation. The results are supported by electron microscopy observations. The most important findings are:

- Observation of the early stages of ordering from nucleation and growth to the onset of tweed
- During heating, the lattice strain along the c-axis of the ordered domains increases. The magnitude of this increase depends on the thermo-mechanical history and chemical composition.
- Above a certain temperature, the lattice strain in the ordered domains starts relaxing. This relaxation temperature is strongly influenced by predeformation and chemical composition.
- It is proposed that the observed lattice strain relaxation is caused by the formation of tweed in the matrix
- Predeformation enhances the ordering rate and the growth of the ordered domains.

Ex situ high-energy X-ray diffraction studies were performed on isothermally aged 18kt red gold alloys and complemented with transmission electron microscopy studies, with the aim to identify the microstructural evolution during ordering. The most important findings are:

- Observation of the significant distortion of $L1_0$ and FCC phases at the early stages of ordering
- Identification of microstructure-related X-ray diffraction features and correlation to the stages of ordering.

Ex situ high-energy X-ray and electron microscopy studies were performed on industrially processed samples of 18k red gold, with the aim to characterize the microstructures that develop under real-life processing conditions. The most important findings are:

- Characterization of the microstructure after recrystallization heat treatments: metastable FCC matrix with a fine dispersion of coherent and chemically ordered domains and minor α_2 phase.
- The observed ordered microstructures correspond to stages I, when coherency strains are strong.
- Plastic deformation induced during the straightening operation enhances natural ageing.

6.8. Perspectives

The research presented in this thesis has raised a number of questions that remain unexplored.

In situ SANS kinetics studies at different heating rates

The volume fraction of coherent $L1_0$ domains cannot be easily obtained from powder X-ray diffraction data. Neutron small angle scattering (SANS) experiments are sensitive to domains embedded in the matrix and provide with information about the volume and number density and size distribution of the domains. This technique might provide with sufficient scattering contrast to follow the evolution of the ordered domains during ordering. *In situ* SANS experiments are suggested to perform kinetics studies and obtain quantitative insights on the thermodynamics of the system. This will also allow studying the influence of thermal treatments on the number density and size distribution evolution of the ordered domains. Linear heating rate experiments are suggested in order to apply model-free iso-conversion methods for the ordering kinetics [155].

Kinetics studies as a function of the level of predeformation

This study has shown that straightening operations and 25% reduction cold rolling facilitate $L1_0$ ordering. However, it remains unclear whether increasing degrees of plastic deformation enhances the ordering rate. This open question could have major implications on the manufacturing process of red gold, by avoiding problematic degrees of deformation. Kinetic studies on the influence of the degree of plastic deformation would provide with a quantitative insight on the evolution of the reaction rate as a function of the degree of cold rolling reduction.

Exploring strategies to suppress chemical ordering

This work reveals the importance of chemical composition on controlling the ordering kinetics. The addition of Pd and Sn result in a lower critical temperature as well as in the stabilization of the microstructure at room temperature. A systematic study that targets suppressing ordering is an encouraging research line. Suggested strategies to suppress ordering would be reducing the stability range of the $L1_0$ phase (off-stoichiometry) while maintaining the A1$\rightarrow$ $L1_0$ phase transition, addition of heavy atoms that hinder low temperature diffusion or find a $L1_0$ phase with a greater c/a ratio closer to cubic symmetry.

REFERENCES

[1]   G. Prandini, Infoscience EPFL (2019).

[2]   W.B. Pearson, G.V. Raynor, A Handbook of Lattice Spacings and Structures of Metals and Alloys [Elektronische Ressource] : International Series of Monographs on Metal Physics and Physical Metallurgy, Vol. 4, Burlington Elsevier Science 2013, 2013.

[3]   L. Nowack, Z. Metallkunde 22 (1930) 24.

[4]   V. S. Arunachalam, R. W. Cahn, Journal of Materials Science 2 (1967) 160–170.

[5]   K. Yasuda, M. Ohta, Journal of the Less Common Metals 70 (1980) P75–P87.

[6]   K. Hisatsune, M. Ohta, T. Shiraishi, M. Yamane, Journal of the Less Common Metals 83 (1982) 243–253.

[7]   K. Udoh, K. Hisatsune, K. Yasuda, M. Ohta, Dental Materials Journal 3 (1984) 253-261,333.

[8]   K.-I. Udoh, K. Yasuda, M. Ohta, Journal of the Less Common Metals 118 (1986) 249–259.

[9]   K. Yasuda, G. Van Tendeloo, J. Van Landuyt, S. Amelinckx, J Dent Res 65 (1986) 1179–1185.

[10]   K. Yasuda, H. Metahi, Y. Kanzawa, Journal of the Less Common Metals 60 (1978) P65–P78.

[11]   R. Hultgren, L. Tarnopol, Nature 141 (1938) 473–474.

[12]   H.A. Bethe, W.L. Bragg, Proceedings of the Royal Society of London. Series A - Mathematical and Physical Sciences 150 (1935) 552–575.

[13]   Bragg William Lawrence, Williams Evan James, Proceedings of the Royal Society of London. Series A, Containing Papers of a Mathematical and Physical Character 145 (1934) 699–730.

[14]   A. Cebollada, R.F.C. Farrow, M.F. Toney, in: Magnetic Nanostructures, H.S. Nalwa (Ed.), American Scientific Publishers, Stevenson Ranch, Calif., 2002, pp. 93–122.

[15]   J. jimenez Flores, Easterling, Kenneth E.; Porter, Phase Transformations in Metals and Alloys (n.d.).

[16]   R.E. Smallman, A.H.W. Ngan, in: R.E. Smallman, A.H.W. Ngan (Eds.), Modern Physical Metallurgy (Eighth Edition), Butterworth-Heinemann, Oxford, 2014, pp. 43–91.

[17]   W. Martienssen, H. Warlimont, eds., Springer Handbook of Condensed Matter and Materials Data, Springer-Verlag, Berlin Heidelberg, 2005.

[18]   Henning, PhD Thesis EPFL (2009).

[19]   M. Arango, A. María, PhD Thesis Northeastern University Boston Massachusets (n.d.) 251.

[20]   P.M. Guymont, Acta Cryst. A36 (1980) 792–795.

[21]   C.H. Johansson, J.O. Linde, Annalen der Physik 417 (1936) 1–48.

[22]   G. Jehanno, P. Perio, Journal de Physique et le Radium 23 (1962) 854–860.

[23]   K. Okamura, H. Iwasaki, S. Ogawa, Journal of the Physical Society of Japan 24 (1968) 569–579.

[24]   M. Takeda, H. Hashimoto, Physica Status Solidi (a) 87 (1985) 141–149.

[25]   M. Guymont, D. Gratias, Journal de Physique Lettres 39 (1978) 437–439.

[26]   J. Bonneaux, M. Guymont, Intermetallics 7 (1999) 797–805.

[27]   G. Effenberg, S. Ilyenko, eds., Noble Metal Systems. Selected Systems from Ag-Al-Zn to Rh-Ru-Sc, Springer Berlin Heidelberg, 2006.

[28]   K. Udoh, M. Ohta, K. Oki, and K. Hisatsune, (2000).

[29]   Raub, E., Z. Metallkunde (1947).

[30]   H-I. Kim, D-H. Lee, J-A. Sim, Y-H. Kwon, H-J. Seol, Materials Characterization 60 (2009) 357–362.

[31]   H.-I. Kim, T.-W. Kim, Y.-O. Kim, S.-Y. Cho, G.-Y. Lee, Y.H. Kwon, H.-J. Seol, Materials Research 16 (2012) 71–87.

[32]   A.M. El Araby, K.-I. Udoh, Y. Tanaka, K. Hisatsune, K. Yasuda, Materials Science and Engineering: A 206 (1996) 290–301.

[33]   K. Hisatsune, K.-I. Udoh, B.I. Sosrosoedirdjo, T. Tani, K. Yasuda, Journal of Alloys and Compounds 176 (1991) 269–283.

[34]   M. Nakagawa, K. Yasuda, J Mater Sci 23 (1988) 2975–2982.

[35]   H.I. Kim, M.I. Jang, B.J. Jeon, (n.d.) 7.

[36]   D.E. Laughlin, K. Srinivasan, M. Tanase, L. Wang, Scripta Materialia 53 (2005) 383–388.

[37]   S. Hashimoto, Acta Crystallogr. A 39 (1983) 524–530.

[38]   J.M. Howe, in: Physical Metallurgy, Elsevier, 2014, pp. 1317–1451.

[39]   J. Nyström, Ark. Phys. 2 (1950) 151.

[40]   M. Hyrabayashi, Nippon Kinzoku Gakkaishi B15 (1951) 1020.

[41]   G. Borelius, J. Inst. Metals 74 (1947) 17.

[42]   G.J. Dienes, Journal of Applied Physics 22 (1951) 1020–1026.

[43]   M. Hirabayashi, The Journal of the Japan Institute of Metals.B 15 (1951) 565–571.

[44]   G.C. Kuczynski, R.F. Hochman, M. Doyama, Journal of Applied Physics 26 (1955) 871–878.

[45]   K. Hisatsune, Y. Tanaka, K. Udoh, K. Yasuda, Intermetallics 3 (1994) 335–339.

[46]   K. Mitsui, Y. Mishima, T. Suzuki, Philosophical Magazine A 59 (1989) 123–140.

[47]   M. de Jong, J.S. Koehler, Phys. Rev. 129 (1963) 40–49.

[48]   L. Tarnopol, R. Hultgren, Trans. Amer. Inst. Min Metallurg. Engrs. Inst. Metal. Div. 188 (1939) 228.

[49]   H.K. K. Yasuda, Bull. Tokyo Med. Dent. Univ. 22 (1975) 101–111.

[50]   H. Buum, Z. Metallkunde 31 (1939) 31.

[51]   M. Hirabayashi, S. Weissmann, Acta Metallurgica 10 (1962) 25–36.

[52]   J.L. O'Brien, G.C. Kuczynski, Acta Metallurgica 7 (1959) 803–806.

[53]   T. Imura, S. Weissmann, J.J. Slade, Acta Crystallographica 15 (1962) 786–793.

[54] A.G. Khachaturyan, Theory of Structural Transformations in Solids., Dover Publications, Newburyport, 2013.

[55] S. Semenovskaya, A.G. Khachaturyan, Acta Materialia 45 (1997) 4367–4384.

[56] Y. Yamazaki, J. Phys. Soc. Jpn. 66 (1997) 2628–2637.

[57] L.E. Tanner, The Philosophical Magazine: A Journal of Theoretical Experimental and Applied Physics 14 (1966) 111–130.

[58] Yu.D. Tyapkin, K.M. Yamaleev, Soviet Physics Doklady 9 (1964) 322.

[59] K.M. Yamaleev, Soviet Physics Journal 8 (1965) 96–98.

[60] Yu.D. Tyapkin, Soviet Physics Doklady 9 (1964) 95.

[61] K. Yasuda, M. Nakagawa, G. Van Tendeloo, S. Amelinckx, Journal of the Less Common Metals 135 (1987) 169–183.

[62] Y. Kanzawa, K. Yasuda, H. Metahi, Journal of the Less Common Metals 43 (1975) 121–128.

[63] K. Yasuda, K. Hisatsune, Gold Bull 26 (1993) 50–66.

[64] M. Ohta, T. Shiraishi, M. Yamane, K. Yasuda, Dent Mater J 2 (1983) 10–17.

[65] K. Yasuda, M. Ohta, J Dent Res 61 (1982) 473–479.

[66] T. Shiraishi, M. Ohta, M. Nakagawa, R. Ouchida, Journal of Alloys and Compounds 257 (1997) 306–312.

[67] J.J. Slade, S. Weissmann, K. Nakajima, M. Hirabayashi, Journal of Applied Physics 35 (1964) 3373–3385.

[68] B. Hansson, R.S. Barnes, Acta Metallurgica 12 (1964) 315–319.

[69] M. Hirabayashi, S. Ogawa, Journal of the Physical Society of Japan 11 (1956) 907–914.

[70] S. Kohara, G.C. Kuczynski, Acta Metallurgica 4 (1956) 221–222.

[71] M. Ohta, T. Shiraishi, R. Ouchida, M. Nakagawa, S. Matsuya, Journal of Alloys and Compounds 265 (1998) 240–248.

[72] Spanl, M, Puschl W., Sprusil, B., Sachl J., Sima, V., Pfeiler, W., Materials Transactions 43 (2002) 560–565.

[73] I. Watanabe, M. Atsuta, K. Yasuda, K. Hisatsune, Dental Materials Journal 10 (1994) 369–374.

[74] G.B. Brook, Gold Bull 6 (1973) 8–11.

[75] K. Sato, D. Watanabe, S. Ogawa, J. Phys. Soc. Jpn. 17 (1962) 1647–1651.

[76] E. Metcalfe, J.A. Leake, Acta Metallurgica 23 (1975) 1135–1143.

[77] G.V. Tendeloo, S. Amelinckx, S.J. Jeng, C.M. Wayman, J Mater Sci 21 (1986) 4395–4402.

[78] B.W. Roberts, Acta Metallurgica 2 (1954) 597–603.

[79] H.-I. Kim, T.-W. Kim, Y.-O. Kim, S.-Y. Cho, G.-Y. Lee, Y.H. Kwon, H.-J. Seol, Mat. Res. 16 (2012) 71–87.

[80]   Tanaka, Materials Transactions 39 (n.d.) 87–94.

[81]   O. Malis, K.F. Ludwig, Physical Review B 60 (1999) 14675–14682.

[82]   O. Malis, K.F. Ludwig, W. Schweika, G.E. Ice, C.J. Sparks, Phys. Rev. B 59 (1999) 11105–11108.

[83]   A. Guinier, R. Griffoul, Rev. Met. Paris 45 (1948) 387–396.

[84]   A. Guinier, Acta Metallurgica 3 (1955) 510–512.

[85]   S. Hashimoto, Acta Cryst A 30 (1974) 792–798.

[86]   S. Hashimoto, Acta Cryst A 37 (1981) 511–516.

[87]   M. Hirabayashi, Journal Physics Society Japan 2 (1959).

[88]   A.Yu. Volkov, B.D. Antonov, A.M. Patselov, The Physics of Metals and Metallography 110 (2010) 250–259.

[89]   K. Tanaka, T. Ichitsubo, M. Koiwa, Materials Science and Engineering: A 312 (2001) 118–127.

[90]   N. Ueshima, M. Yoshiya, H. Yasuda, T. Fukuda, T. Kakeshita, Journal of Applied Physics 115 (2014) 073501.

[91]   A. Kulovits, W.A. Soffa, W. Püschl, W. Pfeiler, MRS Online Proceedings Library Archive 753 (2002).

[92]   M.N.D. Larcher, C. Cayron, A. Blatter, R. Soulignac, R.E. Logé, J Appl Crystallogr 52 (2019) 1202–1213.

[93]   A.R. Deshpande, PhD University Pittsburg (n.d.) 97.

[94]   T. Ichitsubo, K. Tanaka, H. Numakura, M. Koiwa, Phys. Rev. B 60 (1999) 9198–9201.

[95]   T. Ichitsubo, K. Tanaka, M. Koiwa, Y. Yamazaki, Phys. Rev. B 62 (2000) 5435–5441.

[96]   S.N. Hsiao, F.T. Yuan, H.W. Chang, H.W. Huang, S.K. Chen, H.Y. Lee, Applied Physics Letters 94 (2009) 232505.

[97]   S. Lee, K. Edalati, H. Iwaoka, Z. Horita, T. Ohtsuki, T. Ohkochi, M. Kotsugi, T. Kojima, M. Mizuguchi, K. Takanashi, Philosophical Magazine Letters 94 (2014) 639–646.

[98]   K. Hisatsune, T. Shiraishi, Y. Takuma, Y. Tanaka, E. Miura, Journal of Alloys and Compounds 391 (2005) 38–41.

[99]   A. Kulovits, J.M.K. Wiezorek, W.A. Soffa, W. Püschl, W. Pfeiler, Journal of Alloys and Compounds 378 (2004) 285–289.

[100]   J.W. Cahn, Acta Metallurgica 5 (1957) 169–172.

[101]   A.M. Hunt, D.W. Pashley, Journal de Physique et Le Radium 23 (1962) 846–853.

[102]   L. Zou, C. Yang, Y. Lei, D. Zakharov, J.M.K. Wiezorek, D. Su, Q. Yin, J. Li, Z. Liu, E.A. Stach, J.C. Yang, L. Qi, G. Wang, G. Zhou, Nature Materials 17 (2018) 56–63.

[103]   R.W. Vidoz, Lazarevi, Cahn, ACTA METALLURGICA 11 (1963) 17.

[104]   M. Ohta, S. Matsuya, M. Yamane, J Mater Sci 21 (1986) 3981–3985.

[105] T. Shiraishi, M. Ohta, J Mater Sci 24 (1989) 1049–1052.

[106] E. Raub, G. Worwag, Z. Metallkunde 46 (1955) 119.

[107] R.I. Hernandez, K. Udoh, Y. Tanaka, Y. Takuma, H. Winn, K. Hisatsune, Dent. Mater. J. 18 (1999) 235–247.

[108] E. Klay, F. Diologent, J. Arnéodo, P. Dubos, A. Mortensen, Intermetallics 19 (2011) 726–737.

[109] R. Lacroix, C. Niney, Gold Bull 6 (1973) 94–98.

[110] C.J. Raub, D. Ott, Gold Bull 16 (1983) 46–51.

[111] H.-J. Seol, T. Shiraishi, Y. Tanaka, E. Miura, K. Hisatsune, H.-I. Kim, Biomaterials 23 (2002) 4873–4879.

[112] M. Ohta, T. Shiraishi, M. Nakagawa, S. Matsuya, J Mater Sci 29 (1994) 2083–2086.

[113] A.Yu. Volkov, E.F. Talantsev, O.S. Novikova, A.V. Glukhov, K.N. Generalova, B.D. Antonov, Phys. Metals Metallogr. 119 (2018) 1222–1228.

[114] A.J. Schwartz, M. Kumar, B.L. Adams, D.P. Field, eds., Electron Backscatter Diffraction in Materials Science, 2nd ed., Springer US, 2009.

[115] Www.Myscope.Com (n.d.).

[116] J.W. Edington, Interpretation of Transmission Electron Micrographs, London : Macmillan, 1975.

[117] G.H. Michler, ed., in: Electron Microscopy of Polymers, Springer, Berlin, Heidelberg, 2008, pp. 199–217.

[118] D. Kiener, C. Motz, M. Rester, M. Jenko, G. Dehm, Materials Science and Engineering: A 459 (2007) 262–272.

[119] M. Schaffer, B. Schaffer, Q. Ramasse, Ultramicroscopy 114 (2012) 62–71.

[120] George F. Vander Voort, Metallography: Principles and Practice, ASM International, 1999.

[121] P. Skjerpe, J. Gjønnes, E. Sørbrøden, H. Herø, J Mater Sci 21 (1986) 3986–3992.

[122] K. Yasuda, M. Nakagawa, G. Van Tendeloo, S. Amelinckx, Journal of the Less Common Metals 135 (1987) 169–183.

[123] H. Knosp, R.J. Holliday, C.W. Corti, Gold Bull 36 (2003) 93–102.

[124] W.F. Peck, S. Nakahara, Metallography 11 (1978) 347–354.

[125] O. Scherzer, Journal of Applied Physics 20 (1949) 20–29.

[126] D.J. Smith, in: T. Mulvey, C.J.R. Sheppard (Eds.), Advances in Optical and Electron Microscopy, Elsevier, 1989, pp. 1–55.

[127] Stadelmann, P., Http:/Www.Jems-Saas.Ch (n.d.).

[128] N. Iqbal, N.H. van Dijk, S.E. Offerman, M. Moret, L. Katgerman, G.J. Kearley, MRS Proc. 840 (2004) Q7.12.

[129] Dassault Systèmes, Providence, RI, USA, (2011).

[130] N. Schell, A. King, F. Beckmann, T. Fischer, M. Müller, A. Schreyer, Materials Science Forum (2014).

[131] J. Filik, A.W. Ashton, P.C.Y. Chang, P.A. Chater, S.J. Day, M. Drakopoulos, M.W. Gerring, M.L. Hart, O.V. Magdysyuk, S. Michalik, A. Smith, C.C. Tang, N.J. Terrill, M.T. Wharmby, H. Wilhelm, J Appl Cryst, J Appl Crystallogr 50 (2017) 959–966.

[132] R.B. Neder, T. Proffen, Diffuse Scattering and Defect Structure Simulations: A Cook Book Using the Program DISCUS, Oxford Univ. Press, Oxford, 2008.

[133] P. Scherrer, Göttinger Nachrichten Gesell. 2 (1918) 98.

[134] MIT MRSEC X-Ray Diffraction Facility (n.d.).

[135] Fautelais, Acta Materialia 47 (1999) 2539–2551.

[136] E.K. A. Mortensen F. Diologent, Acta Materialia 59 (2011) 3184–3195.

[137] L.E. Tanner, M.F. Ashby, Physica Status Solidi (b) 33 (1969) 59–68.

[138] R.F.S. Hearmon, Rev. Mod. Phys. 18 (1946) 409–440.

[139] T. Anraku, I. Sakaihara, T. Hoshikawa, M. Taniwaki, Materials Transactions 50 (2009) 683–688.

[140] T. Shiraishi, M. Ohta, M. Nakagawa, R. Ouchida, Journal of Alloys and Compounds 257 (1997) 306–312.

[141] M. Garcia-Gonzalez, S. Van Petegem, N. Baluc, S. Hocine, M. Dupraz, F. Lalire, H. Van Swygenhoven, Scripta Materialia 170 (2019) 129–133.

[142] W. Jost, Z. Physik Chern 21B (1933) 158.

[143] H. Fukushima, J. Sugiura, M. Doyama, J. Phys. F: Met. Phys. 6 (1976) 1845–1850.

[144] K.R. Elder, O. Malis, K. Ludwig, B. Chakraborty, N. Goldenfeld, EPL 43 (1998) 629.

[145] H.M. Rietveld, J Appl Crystallogr 2 (1969) 65–71.

[146] P. Scardi, M. Leoni, Acta Cryst A 58 (2002) 190–200.

[147] G.-X. Kong, X.-J. Ma, Q.-J. Liu, Y. Li, Z.-T. Liu, Physica B: Condensed Matter 533 (2018) 58–62.

[148] J.B. Newkirk, A.H. Geisler, D.L. Martin, R. Smoluchowski, JOM 2 (1950) 1249–1260.

[149] J.B. Newkirk, R. Smoluchowski, A.H. Geisler, D.L. Martin, Acta Crystallographica 4 (1951) 507–512.

[150] A. Silberstein, P.C. Clapp, Phys. Rev. B 38 (1988) 9555–9566.

[151] K.T. M. Koiwa T. Ichitsubo, Materials Science and Engineering: A 312 (2001) 118–127.

[152] K. Tanaka, T. Ichitsubo, M. Koiwa, Materials Science and Engineering: A 312 (2001) 118–127.

[153] J. W. Christian, in: Oxford: Pergamon Press, n.d., pp. 117–606.

[154] V. Gerold, Z. Metallkunde 45 (n.d.) 593–599.

[155] M.J. Starink, Thermochimica Acta 404 (2003) 163–176.